Spectroscopic and Structural Characterization of Synthetic Models of Dioxygen-Activating Nonheme Diiron and Monoiron Systems

A Dissertation

SUBMITTED TO THE FACULTY OF

UNIVERSITY OF MINNESOTA

BY

Chase Silver Abelson

IN PARTIAL FULFILLMENT OF THE REQUIREMENTS

FOR THE DEGREE OF

DOCTOR OF PHILOSOPHY

Professor Lawrence Que, Jr., Adviser

November 2022

© Chase Silver Abelson 2022

Acknowledgements

There are too many people to thank for supporting me throughout my studies. Firstly, I'd like to thank Professor Lawrence Que, Jr. for welcoming me into his second family and providing me the freedom to pursue what interested me most. He always encouraged me to ask more questions and try to understand my work through and through. Thank you for helping me become an independent scientist.

Throughout my studies, I've had several close friends inside and outside of the research lab. I'd like to thank the Que research lab for their help. A big thank you to Dr. Subhasree Kal and Dr. Patrick Crossland for persuading me to work in the Que group during my first year and Subhasree, Pat, and Dr. Yuan Sheng for making the office interesting and making it fun to come to work each day. Additionally, I'd like to thank Subhasree, Dr. Waqas Rasheed, and Dr. Shuangning Xu for providing me with great mentorship and getting me started in the bioinorganic research space. Also, I'd like to thank Dr. Wei-Min (Seesaw) Ching for inspiring me to be a better chemist and a better person, for forcing me to think critically inside and outside of lab. The XAS team, while small, was mighty. A massive thank you to Pat for showing me everything spectroscopy has to offer and inspiring me to shoot lasers at things. I'd like to thank Dr. Andrew Jasniewski (even though we never overlapped) and Dr. Apparao Draksharapu for their hard work and contributions to the XAS and resonance Raman instrumentation that enabled a majority of my graduate studies. And a thank you to my new friends Dr. Bittu Chandra and Dr. Nabhendu Pal for helping me through my final year as a graduate student.

As a synthetic chemist turned spectroscopist, I have many collaborators I'd like to thank. I relied heavily on Shuangning Xu for his careful work towards understanding the proton-assisted work that led to my desulfonation work. Bittu worked hard on understanding the TQA-diiron work and was patient enough to prepare many samples. A special thank you to Professor Dong Wang and Yan Li for opening my eyes to dicobalt chemistry and allowing me to learn alongside them and to Professor Thomas Makris and Dr. Olivia Manley for teaching me biochemistry and helping me escape synthetic chemistry and play inside the world of enzymes. While efforts with these two groups were not discussed in my thesis, they were instrumental in expanding my skill set and allowing me to be successful in my PhD.

Lastly, I would like to thank my friends and family for the love and support throughout the years. Thank you to my "roommates" Dr. Rishad Dalal, Dr. Brendan Graziano, and Jack Elder for being patient with my bad taste in music and always welcoming me into their home. I have played soccer throughout my entire life, and without Dr. Guilhem De Hoe,

Dr. Spencer Reisbick, Dr. Ryan Gnabasik and Dr. Patrick Crossland, I would never have had the opportunity to continue playing soccer throughout my graduate studies. A thank you to my video games friend from across the world for giving me an escape every week for when work was too stressful. A special thank you to Matthew Bond and Patrick Hulbert for always been easy to talk to and for the challenging conversations. Another thank you to my Thai friends in Minnesota for expanding my horizons and for being so kind to a *farang* like me.

I would have been lost without my parents, John and Lynn. Thank you for the phone-calls, advice, and love and support you both have given me over my entire life. A big thank you to my brothers Ryan and Alex who have always been a phone-call away when my catalytic converter gets stolen or when I need advice on research or job hunting. I am shaped by my family and am forever grateful to them. Lastly, I want to thank my current and lifelong roommate, Siri (Kik). Thank you for teaching me to be a kind and giving person, for showing me the importance of caring about others, and for opening up my eyes to the world outside of my living room.

I was lucky enough to know all four of my grandparents: Arnold and Irene & Bob and Nanna. They shaped my parents and are the ones truly responsible for the love and support I have received over the years. I was fortunate enough to live down the street from Arnold and Irene and have been influenced by my grandfather's humor and my grandmother's patience. Bob and Nanna lived across the country, and I always excitedly anticipated their regular visits from 3,000 miles away. While Bob left us shortly after I entered adulthood, he (to my knowledge) is the only chemist throughout both sides of my family and I thank him for my love of chemistry. Nanna has strongly carried on, and I am thankful for our weekly phone-calls, for keeping me grounded, and for continuing to shower me with extra love on Bob's behalf.

Dedication

This thesis is dedicated to my grandparents, for the endless love and support they have given to me, my brothers, and my parents, and for their grit, determination, kindness, and inspiration to be an individual.

Abstract

Using monoiron and diiron active sites, Nature has found a way to activate O_2 to perform powerful oxidations. Upon the binding of O_2 into the active site, the iron centers are oxidized to high-valent intermediates, and these highly oxidized species are able to break strong C-H bonds, such as those found in methane (104.5 kcal/mol). There has been a great interest in understanding the mechanistic cycle of these reactive oxidants as well as how nature can craft active sites that can perform difficult transformations.

Understanding how enzymes activate O_2 requires the employment of a variety of techniques, including structural characterization through X-ray absorption spectroscopy (XAS), single crystal X-ray diffraction (XRD), and nuclear magnetic resonance (NMR). Other spectroscopic techniques, like electronic absorbance, resonance Raman, and electron paramagnetic resonance (EPR) help further our understanding of the wide variety of these oxygen-activating enzyme active sites. Due to the complexity of handling these enzymes, biomimetic synthetic complexes have been synthesized and investigated, with well over 100 characterized high-valent iron complexes. These small molecules allow for a greater understanding of why Nature employs iron centers to perform biologically vital transformations.

In Chapter 2, ultraviolet-visible spectrophotometry (UV-Vis) and resonance Raman spectroscopy have been employed to better understand the role of a proton in helping to regulate the O—O bond cleavage step to unleash a powerful high-valent oxoiron oxidant

in a synthetic complex. Chapter 3 is an investigation of synthetic diiron systems whereby the structures of complexes have been structurally characterized using XAS and other techniques. This work is an effort in helping to better understand the mechanism by which diiron enzymes can form high-valent iron centers through the activation of O_2. In Chapter 4, a combination of reactivity and spectroscopy has been employed to better understand how electronic parameters and the steric environments can perturb the oxidizing potential of $Fe^{IV}(O)$ species. Overall, this thesis demonstrates the power of combining a variety of spectroscopic techniques to help generate and support hypotheses for enzyme mechanisms.

Table of Contents

Acknowledgements i

Dedication iii

Abstract iv

List of Figures viii

List of Tables xi

Chapter 1: Functional Overview of the Formation of High-Valent Oxoiron Complexes 1

1.1 — Formation of High-Valent Oxoiron Complexes in Nature 2

1.2 — Monoiron Non-heme Enzymes 4

1.3 — The Diiron Enzyme Soluble Methane Monooxygenase 7

1.4 — Synthetic Models of Monoiron Non-heme Enzymes 15

1.4.1 — Usage of Polypodal Ligands to Enable the Synthesis of High-Spin Monoiron-Oxo Centers 15

1.4.2 — Overview of *S* = 1 Synthetic Oxoiron(IV) Complexes 21

1.4.3 — Formation of $Fe^{V}(O)$ Intermediates 25

1.5 — Synthetic High-Valent Diiron-Oxo Model Complexes 27

1.6 — Conclusion 32

Chapter 2: Oxidative Desulfonation of an Aromatic Ring by a High-Valent Iron-Oxo Complex 34

2.1 — Introduction 35

2.2 — Formation of 2 with HOAc and H_2O_2 at 25 °C 36

2.3 — Reaction of 2 with Strong Acids 37

2.4 — Fe^{III}-phenolate Generation and Spectroscopic Characterization 41

2.5 — Mechanistic Investigation 45

2.6 — Summary, Conclusions, and Broader Implications 55

2.6.1 — Additional Figures 60

Chapter 3: Structural Investigation of a Pathway to Form a High-Spin Bimetallic sMMOH-Q Mimic 62

3.1 — Introduction 63

3.2 — Pathway for Formation of Complexes 66

3.2.1 — XANES Analysis 67

3.2.2 — EXAFS Analysis 70

3.3 — Generation and Structural Characterization of Complex 3 83

3.4 — Conclusion **90**

Chapter 4: Modeling Transient Enzymatic Oxoiron(IV) Complexes **92**

4.1 — Introduction **93**

4.2 — Characterization of Fe^{II}(TMC)-like Complexes **95**

4.3 — Characterization of Corresponding High-Valent Oxoiron(IV) Intermediates **98**

4.3.1 — Structural Characterization of Oxoiron(IV) Species **103**

4.3.2 — HAT Reactivity of Oxoiron(IV) Species **106**

4.4 — Comparison of Oxoiron(IV) Complexes Modulated by Sterically-Imposed Tilt of the Iron-Oxo Bond **108**

4.5 — Conclusion **112**

4.6 — Additional X-ray Diffraction Data **114**

Appendix **153**

Experimental Section **153**

Bibliography **155**

List of Figures

Figure 1. Proposed mechanism for the catalytic cycle of a generic α-ketoglutarate-dependent iron monooxygenase enzyme performing a hydrogen atom abstraction on an organic substrate. 5
Figure 2. Proposed mechanistic cycle of the oxidation of methane as performed by soluble methane monooxygenase. Non-bridging amino acids and hydrogen bonds have been removed for clarity and simplicity. Additionally, several steps in the mechanistic cycle have also been removed for simplicity. 10
Figure 3. Single crystal X-ray diffraction structures of the two characterized S = 2 complexes. Adapted from Ref [9] with permission. 17
Figure 4. Crystal structure the nonheme iron enzyme L-arginine 3-hydroxylase (VioC) with a stable V^{IV}=O moiety in place of the reactive ferryl unit. Modified from Ref [9] with permission. 18
Figure 5. A collection of nine S = 1 $Fe^{IV}(O)$ structures characterized through X-ray crystallography. Adapted from Ref [9] with permission. 24
Figure 6. Overview of the many interconversions of diamond core and open core complexes. A: Ref [30, 82]; B: Ref [30, 83]; C: Ref [83, 84]; D: Ref [30]; E: Ref [85]; F: Ref [86]; G: Ref [87]; H: Ref [86, 87]; I: Ref [88-90]; J: Ref [91]. Adapted from Ref [9] with permission. 29
Figure 7. UV-Vis spectrum associated with the addition of 10 equiv of HOAc and 10 equiv of 90 % H_2O_2 to a solution of 1 mM $[Fe^{II}(MeTPEN)(CH_3CN)]^{2+}$ in CH_3CN at 25 °C. 37
Figure 8. UV-Vis spectrum associated with the addition of 1 equiv TsOH acid to the intermediate 2 in CH_3CN at 1 mM with respect to Fe^{II} starting complex. 38
Figure 9. Proposed possible products formed upon the hydroxylation of TsOH that give rise to the broad chromophore observed at 640 nm. 41
Figure 10. Generation of a generic LFe^{III}-phenolate species formed by the addition of a generic para substituted phenol to LFe^{II} starting material in the presence of air, where L = MeTPEN. 42
Figure 11. Resonance Raman spectra of the phenolate product when intermediate **2** was reacted with 4-$ClC_6H_4SO_3H$ (2, purple) or TsOH (4, blue) compared to the product generated when Fe^{II} starting material is reacted with 4-ClC_6H_4OH (1, green) or p-cresol (3, red) in the presence of atmospheric oxygen. All values labeling vibrations are in units of cm^{-1}. Values in gold (487, 703, 1092 cm^{-1}) are associated solely with spectra 1 and 2, while the value in red (562 cm^{-1}) is associated with spectra 3 and 4. Values above 1100 cm^{-1} are associated with all spectra. All spectra were obtained in CH_3CN at 77 K with 561 nm laser excitation. Reaction conditions for 2, 4: 3 mM **2**, 10 equiv HOAc, 2.5 equiv 4-$ClC_6H_4SO_3H$ (spectrum 2) or TsOH (spectrum 4) in CH_3CN at 233 K; reaction conditions for 1, 3: 3 mM **1**, 10 equiv 4-ClC_6H_4OH (spectrum 1) or p-cresol (spectrum 3) in CH_3CN at 298 K. 45
Figure 12. UV-Vis spectrum associated with the addition of 1 equiv $HClO_4$ acid concomitantly with 200 equiv benzene to the intermediate **2** in CH_3CN at 1 mM with respect to Fe^{II} starting complex at 20 °C 50
Figure 13. Proposed mechanisms for the hydroxylation of the benzenesulfonate species 50

Figure 14. Spectral comparison of a) **2** upon the addition of TsOH at -40 °C (blue) and b) Fe^{II} starting material upon the addition of p-cresol in the presence of air at 20 °C. Both spectra were obtained in CH_3CN. [Fe] = 3 mM 60
Figure 15. UV-Vis spectrum associated with the addition of 1 equiv 2-mesitylenesulfonic acid (2-Mes) to a solution of intermediate **2** in CH_3CN at 1 mM Fe^{II} complex concentration. 60
Figure 16. Eyring plots for **2** decay under different conditions. A: with only HOAc; B: with HOAc and 0.5 equiv HOTf; C: with HOAc and 1.0 TsOH; D: with HOAc and 0.5 equiv $HClO_4$; E: with HOAc and 1.0 equiv 2-Mes; F: with HOAc and 1.0 equiv 2-Mes. Reaction conditions A-E: 1 mM **1**/10 equiv HOAc/10 equiv 90% H_2O_2/with or without acid in CH_3CN; reaction condition F: 1 mM $[(Fe^{II}(CH_3CN)(BnTPEN)]^{2+}$ /10 equiv HOAc/10 equiv 90% H_2O_2/0.5 equiv 2-Mes in CH_3CN. Values are listed in Table 3. 61
Figure 17. Proposed catalytic cycle of the oxidation of methane to methanol performed by soluble methane monooxygenase. Adapted from Ref [21] with permission. 64
Figure 18. Cartoon depictions of the structures explored in this study. Ligand has been removed for simplicity. L = TQA 66
Figure 19. Fourier transformed EXAFS spectrum and the k-space data (inset) for $[Fe^{II}_2(\mu\text{-}OH)_2(TQA)_2]^{2+}$ (Fit 4). 73
Figure 20. Fourier transformed EXAFS spectrum and the k-space data (inset) for $[Fe^{III}_2(\mu\text{-}O)_2(TQA)_2]^{2+}$ (Fit 4) 76
Figure 21. Single crystal X-ray diffraction for $[Fe^{III}_2(\mu\text{-}O)_2(TQA)_2]^{2+}$ (**2**) drawn at 50 % probability with H-atoms, solvent, and counteranionic $^-$OTf omitted for clarity. Color scheme: Fe, orange; O, red; N, blue; C, gray. Selected bond lengths (Å): Fe1—O1, 1.839(3); Fe1—O2, 1.917(3); Fe—N_{ave}, 2.255(13); Fe1·····Fe2, 2.6679(8). Data available from Ref [139]. 78
Figure 22. Collection of ligands discussed in this chapter. 81
Figure 23. Fourier Transform EXAFS spectrum and the k-space data (inset) for $[Fe^{III}_2(\mu\text{-}O)(\mu\text{-}1,2\text{-}O_2)(TQA)_2]^{2+}$ (Fit 4) 85
Figure 24. Pre-edge area fitting of all 3 complexes explored in this study 90
Figure 25. Generic catalytic cycle of the oxidation of alkyl products performed by α-ketoglutarate dioxygenase-dependent non-heme iron enzymes. Adapted from Ref [1] with permission 93
Figure 26. Crystal structures of three TMC-related iron(II) structures. Selected bond lengths available in Table 12. Additional structural information for both $[Fe^{II}(TMC\text{-}im)]^{2+}$ and $[Fe^{II}(TMC)(Cl)]^{+}$ are available at the end of this chapter. Additional information for $[Fe^{II}(Bn3MC)(OTf)]^{+}$ has been published in Ref [4] 96
Figure 27. Fourier transformed EXAFS spectrum and the k-space data (inset) for $[Fe^{IV}(O)(TMC\text{-}im)]^{2+}$ (Fit 4). 101
Figure 28. Pre-edge area fitting of $[Fe^{IV}(O)(TMC\text{-}im)]^{2+}$. 102
Figure 29. Comparison of structures of N4Py and N4Py derivative complexes. The second crystal structure is of the Fe^{II} starting material. Complexes **c** and **d** are DFT optimized structures. Ref: **a**[2]; **b**[3]; **c**[5], **d**[5] 109

Figure 30. k_2 plots for the anaerobic oxidation of different HAT substrates performed by $[Fe^{IV}(O)(6Me_2N4Py)]^{2+}$. The slopes of the fitted red lines represent the second-order rate constants (k_2 M^{-1} s^{-1}) at 298 K in acetonitrile. 112

List of Tables

Table 1. Properties of enzymatic and synthetic high-spin oxoiron(IV) complexes. 20
Table 2. Optical parameters associated with the UV-Vis spectroscopic features of the products formed upon the addition of 2.5 equiv benzenesulfonic acid reacted with **2** (Col. 2, -40 °C) or approximately 10 equiv phenol to starting Fe^{II} material in the presence of atmospheric oxygen (Col. 3, 20 °C). All experiments are normalized to 3 mM [Fe^{II}] and carried out in CH_3CN. 40
Table 3. Eyring parameters for the decay of (L)Fe^{III}–OOR complexes (solvent is CH_3CN unless otherwise specified) 49
Table 4. Comparison of XANES data for the complexes in this work. 68
Table 5. Comparison of XANES data for diiron diamond core complexes. 70
Table 6. EXAFS fits for $[Fe^{II}_2(\mu\text{-}OH)_2(TQA)_2]^{2+}$ (1). Best fit in bold. 73
Table 7. EXAFS fits for $[Fe^{III}_2(\mu\text{-}O)_2(TQA)_2]^{2+}$ (**2**). Best fit in bold 77
Table 8. Comparison of diiron diamond core structures of diiron complexes. All distances are in Å. Values that are italicized are obtained through X-ray diffraction, while values in print are obtained using X-ray Absorption Spectroscopy. Ligand structures can be found in Figure 22. 82
Table 9. EXAFS fits for $[Fe^{III}_2(\mu\text{-}O)(\mu\text{-}1,2\text{-}O_2)(TQA)_2]^{2+}$ (3). Best fit in bold. 86
Table 10. Comparison of structural and XANES data for different peroxo complexes with the general formula $[Fe^{III}_2(\mu\text{-}O)(\mu\text{-}1,2\text{-}O_2)(L)_2]^{2+}$ where L is the ligand listed in column 1. Ligand structures can be found in Figure 22. All distances in columns 2-4 are in units of Å. Values in italics are obtained through X-ray diffraction 88
Table 11. Comparison between best EXAFS fits for the complexes explored in this study. All complexes are ligated by two TQA molecules and have an overall charge of 2+. 89
Table 12. Comparison of single crystal X-ray diffraction of iron(II) complexes ligated by TMC-related complexes. The atom (L) in parentheses in column 3 indicate the metal-L bond. 98
Table 13. EXAFS fits for $[Fe^{IV}(O)(TMC\text{-}im)]^{2+}$ (1-Im). Best fit in bold. 101
Table 14. Comparison of XANES and Fe=O bond distance for TMC oxoiron(IV) structures with the generic structure $[Fe^{IV}(O)(L)]^{2+/+}$. In column one, 1 corresponds to an $Fe^{IV}(O)$ with a TMC ligand framework derivative where the 6^{th} ligand is bound through a nitrogen present in the cyclam. Complexes with 1' indicate that the 6th coordinating ligand is non-pendant. Weighted area is calculated as: pre-edge area/yield 103
Table 15. Comparison of data obtained for eleven of the crystallographically characterized complexes. 106
Table 16. Comparison of self-decay and reactivity for TMC and TMC-like oxoiron(IV) complexes. 107
Table 17. Comparison of the structure, reactivity and thermal stability of the four N4Py and N4Py-derivative complexes. 111
Table 18. Crystal data and structure refinement for $[Fe^{II}(TMC\text{-}Im)]^{2+}$. 116
Table 19. Atomic coordinates (x 10^4) and equivalent isotropic displacement parameters ($Å^2$ x 10^3) for $[Fe^{II}(TMC\text{-}Im)]^{2+}$. 118
Table 20. Bond lengths [Å] and angles [°] for $[Fe^{II}(TMC\text{-}Im)]^{2+}$. 121

Table 21. Anisotropic displacement parameters ($Å^2 x\ 10^3$) for $[Fe^{II}(TMC\text{-}Im)]^{2+}$. 128
Table 22. Hydrogen coordinates (x 10^4) and isotropic displacement parameters ($Å^2$ x 10^3) for $[Fe^{II}(TMC\text{-}Im)]^{2+}$. 131
Table 23. Torsion angles [°] for $[Fe^{II}(TMC\text{-}Im)]^{2+}$. 134
Table 24. Crystal data and structure refinement for $[Fe^{II}(TMC)(Cl)]^{+}$. 138
Table 25. Atomic coordinates (x 10^4) and equivalent isotropic displacement parameters ($Å^2 x\ 10^3$) for $[Fe^{II}(TMC)(Cl)]^{+}$ 139
Table 26. Bond lengths [Å] and angles [°] for $[Fe^{II}(TMC)(Cl)]^{+}$. 141
Table 27. Anisotropic displacement parameters ($Å^2 x\ 10^3$) for $[Fe^{II}(TMC)(Cl)]^{+}$. 147
Table 28. Hydrogen coordinates (x 10^4) and isotropic displacement parameters ($Å^2$ x 10^3) for $[Fe^{II}(TMC)(Cl)]^{+}$. 149
Table 29. Torsion angles [°] for $[Fe^{II}(TMC)(Cl)]^{+}$. 152

Chapter 1: Functional Overview of the Formation of High-Valent Oxoiron Complexes.

1.1 — Formation of High-Valent Oxoiron Complexes in Nature

Nature has discovered a way to activate oxygen using iron through a four-electron process by which dioxygen is reduced to form metal-oxidants that are competent towards performing difficult oxidations of organic substrates. These enzymes are able to perform oxidative transformations with high levels of chemo-, regio-, and stereoselectivity, even activating the strongest aliphatic C-H bond found in methane (BDE = 104.5 kcal/mol). These directed oxidations promote a great level of interest in understanding this work, and a significant effort is made towards trying to understand the process by which these proteins are able to utilize oxygen.

Iron proteins can be divided into two broad categories: heme and non-heme proteins. Efforts to understand heme proteins predates the non-heme counterparts.[6] A heme protein is one with an iron metal center ligated by a porphyrin ring in the active site, the best-known example being hemoglobin, the mammalian dioxygen carrier. While hemoglobin is a transport protein, responsible for carrying oxygen throughout the body, there is a subset of heme proteins that can break the O—O bond in oxygen to perform powerful oxidative transformations. This subset of heme proteins, referred to as heme enzymes, have long been of interest to the scientific community and lend themselves well to characterization due to characteristic strong absorbance in the UV-visible region.[6] In recent news, the heme enzymes were found to be so impressive in their oxidative (both native and non-native transformations) that in 2018, Frances Arnold received the Nobel

Prize in Chemistry for the directed evolution of heme enzymes like cytochrome P450 to perform non-native transformations like the primary amination of allylic and benzylic $C_{(sp3)}$-H bonds[7] and nitrene transfer[8] reactions.

Another subset of iron proteins that can perform powerful oxidative transformations are the non-heme enzymes, which are as the name suggests iron proteins that do not contain the porphyrin macrocycle cofactor. These non-heme iron enzymes can be broken into two groups that have monoiron and diiron active sites, with many similarities between these two groups. One of the most important similarities lies in the first coordination sphere of these active sites where the irons are typically ligated by a combination of histidine and aspartic or glutamic amino acids. Another useful similarity between the monoiron and diiron active sites is the electronic process by which they activate dioxygen or O_2. In a majority of the enzymatic cycles, one (or both) iron(s) is reduced to Fe(II). Upon the reaction with dioxygen, the iron(s) is oxidized to Fe(III). Through some other processes which will be discussed later, the iron(s) activates dioxygen to form a (di)ferryl intermediate that has been demonstrated to be responsible for the oxidation of organic substrates.[9] While there are many distinguishing features between monoiron and diiron systems, it is important to understand that the many similarities allow for comparisons between the two groups.

Because of the complications of working with proteins, model complexes have long been used to gain insight into how nature uses metals to perform powerful oxidations. A majority of this work has been recently discussed by us in a review published

in Comprehensive Coordination Chemistry III,[9] and the discussion herein is an overview of what can arguably be called the highlights of the past six decades of research in both the model complexes and enzyme intermediates.

1.2 — Monoiron Non-heme Enzymes

Monoiron enzymes span a broad range of oxidative reactivitiy.[9] Many of these enzymes feature active sites with a combination of histidine and aspartate or glutamate, a combination of amino acids commonly referred to as the "2-His-1-carboxylate facial triad".[10] This facial triad motif is commonly found in the active sites of the family of α-ketoglutarate (αKG)-dependent non-heme iron enzymes such as taurine: α-ketoglutarate dioxygenase (TauD) that employ αKG as a cosubstrate that coordinates to the iron center to help in the activation of dioxygen. The generic mechanism for these non-heme enzymes[11] first requires the initial binding of the cosubstrate αKG to the iron center (Figure 1). Once the substrate enters the active site, dioxygen then binds to the iron center, oxidizing the iron center while reacting with αKG, driving off CO_2. This resulting $Fe^{IV}(O)$ complex in TauD, namely TauD-***J***, is the powerful oxidant that is able to perform HAT on the substrate RCH_3. The $Fe^{IV}(O)$ center has been found to be high-spin $S = 2$, arguably an important electronic argument for why these monoiron enzymes have such high oxidizing potentials.[9] This intermediate, namely the $Fe^{IV}(O)$ or oxoiron(IV), is a powerful oxidant found in many enzymes, capable of breaking incredibly challenging C-H bonds as well as performing other impressive oxidative transformations.[11, 12] TauD-***J*** reacts with the organic substrate, homolytically cleaving a strong C-H bond, resulting in

an $Fe^{III}(OH)$ species and an alkyl-centered radical, which then undergo "radical rebound" to form a C–O bond that results in the formation of an iron(II) center and the hydroxylated product. This radical rebound step has been well studied and characterized in both heme[6] and non-heme[13] systems.

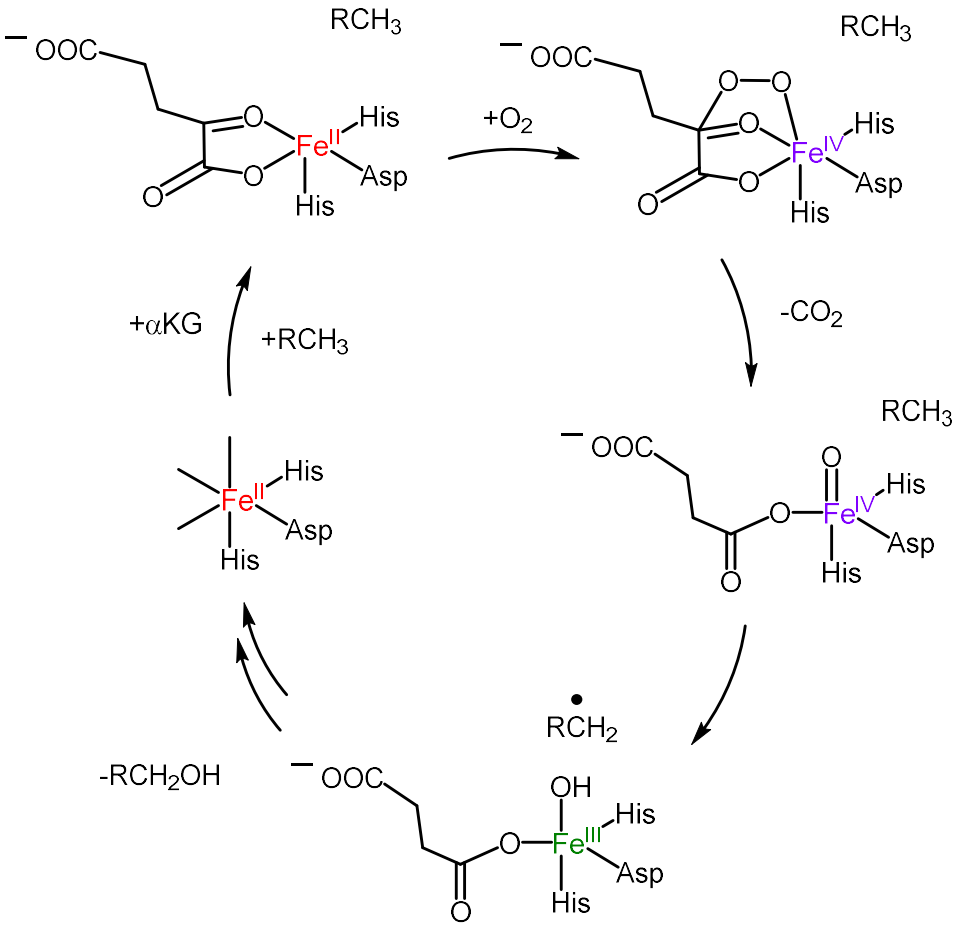

Figure 1. Proposed mechanism for the catalytic cycle of a generic α-ketoglutarate-dependent iron monooxygenase enzyme performing a hydrogen atom abstraction on an organic substrate.

A very similar mechanism is proposed for related halogenase enzymes, such as syringomycin biosynthesis enzyme 2 (SyrB2), which differ somewhat from the

hydroxylases. Most importantly, the aspartate amino acid is replaced with a halogen, either a chloride or bromide (SyrB2-Cl and SyrB2-Br, respectively) and a halogenated product is obtained. During the enzymatic cycle, the alkyl-centered radical rebounds with the halogen instead not the $Fe^{III}(OH)$ species. This change in reactivity is what leads to the halogenation-type reactivity as opposed to the hydroxylation.

Some of these enzymes have been well characterized by spectroscopic techniques such as XAS and UV-Visible-NIR, Mössbauer, and Raman spectroscopies, with the two best characterized oxoiron(IV) intermediates being those found in the TauD and SyrB2-Cl cycles.[13-17] EXAFS studies reveal Fe(IV)=O bond lengths of 1.62 Å and 1.66 Å, respectively.[18, 19] Mössbauer studies reveal respective parameters δ = 0.31 mm/s and ΔE_Q = –0.88 mm/s and δ = 0.30 mm/s and ΔE_Q = 1.09 mm/s for the TauD[17] and SyrB2-Cl[19] intermediates, respectively. These parameters are characteristic of *S* = 2 oxoiron(IV) complexes.[9] Resonance Raman studies have also been identified the iron-oxo vibration for TauD-***J***, which was found to be 821 cm^{-1}.[20] This vibration may correlate with reactivity, where the lower in energy the vibration, the more reactive the system. In fact, this vibration is lower than a great number of synthetic *S* = 1 systems,[9] maybe providing the field with a probe into the reactivity of these iron centers. There are only a dozen or so *S* = 2 synthetic complexes that have been characterized by vibrational spectroscopy.[9] Of these dozen, a majority enforce a different geometry around the iron center when compared to that of TauD. This geometry change enforces a different d-orbital splitting of the iron in order to access the high-spin *S* = 2 state (to be discussed more in depth later

in this work).[9] This makes comparisons between the TauD-***J*** value and the synthetic values difficult, necessitating the characterization of more $S = 2$ complexes with a geometry more closely related to that found in the TauD active site.

1.3 — The Diiron Enzyme Soluble Methane Monooxygenase

There are many similarities between the monoiron and diiron enzymes. Similar to the monoiron enzymes, the diiron active sites contain a combination of histidine and carboxylate amino acids ligating the metal centers. In the diiron systems, there is usually a carboxylate amino acid that bridges between the two metal centers in conjunction to the aforementioned histidine and carboxylate amino acids that ligate the individual metal centers. These amino acids serve as the scaffold that holds the iron centers in the appropriate geometry to allow for activation of dioxygen and subsequent substrate oxidation. When discussing the diiron enzymes, it is common to refer to the metal centers and bridging amino acids as the "core" and this shorthand will be used throughout this work. One of enzymes of great interest is soluble methane monooxygenase (sMMO) due to its capability of oxidizing the 104 kcal/mol C-H bond of methane to methanol. Data has been principally obtained from studies of the enzymes from *Methylosinus trichosporium* OB3b (*Mt* OB3b) and *Methylococcus capsulatus* Bath (*Mc* Bath). These two methanotrophic bacteria have been found to be incredibly similar in iron active site structure and nearly identical in all their characteristics. Therefore, data discussed in this work will not be distinguished as being from either bacteria. sMMO is a multicomplex

protein comprised of a hydroxylase protein MMOH, a regulatory protein MMOB and an electron-transfer reductase MMOR. References to sMMO will primarily be with respect to MMOH as this is the protein where the hydroxylation of methane occurs and is the most relevant to efforts herein.

sMMOH is a diiron enzyme that is ligated by two histidine amino acids and four glutamate residues, with two of these glutamate residues bridging the iron centers. One carboxylate bridges in a μ-1,3-O_2CR motif whereby each carboxylate oxygen atom is bound to a different iron. The other carboxylate is bound in a μ-1,1-O_2CR motif, where only one oxygen is responsible for binding to both metal centers and the second oxygen is bound to only one iron. The binding motif of the μ-1,1-O_2CR carboxylate is proposed to change configuration during the mechanistic cycle.

The catalytic cycle of sMMOH is reasonably well formulated, with few, but important, questions yet to be fully understood. The iron centers are initially reduced to iron(II) (MMO$\mathbf{H}^{red}$) either by NADH-reduced proteins in nature or using chemical reductants. This now-primed core is able to bind dioxygen, oxidizing both iron centers to form a Fe^{III}_2(μ-1,2-O_2)(μ-1,1-O_2CR) structure, namely MMOH-**P**. Also, a solvent water molecule that was bound to a ferrous atom is deprotonated to form a hydroxide. The peroxo O—O bond is then activated, and one equivalent of water is expelled to form the MMOH-**Q** intermediate. This species has been rife with controversy as to what is the exact assignment of the core structure. The core structure is proposed to be a diferryl intermediate with two bridging oxygens, referred to as a diferryl bis-μ-O, sometimes

colloquially described as a diferryl diamond core structure. Intermediate **Q** is proposed then to perform a hydrogen atom transfer reaction (HAT) where an H-atom is abstracted from methane by a bridging oxygen atom, forming an unsymmetric Fe^{IV}/Fe^{III} core structure and an alkyl radical. These two intermediates then react and the alkyl radical and hydroxide bound to the iron center form the desired product methanol. A diferric core remains, which is in turn reduced back to the diferrous starting species $\mathbf{H^{red}}$ in preparation for another turnover of the catalytic cycle.

There are several structural changes of note throughout the catalytic cycle of MMOH. One noteworthy change is the rearrangement of the diiron core structure upon the oxidation of the diiron(III) centers to diiron(IV). It has been proposed that the carboxylate of the amino acid that is bound to both iron centers through only one oxygen atom rearranges and adopts a μ-1,3-O_2CR binding mode, similar to the other bridging carboxylate. This rearrangement is proposed to occur concomitantly with the loss of a solvent water coordinated to the metal center. This structure is maintained until both iron centers are reduced to diferric state upon the oxidation of methane.

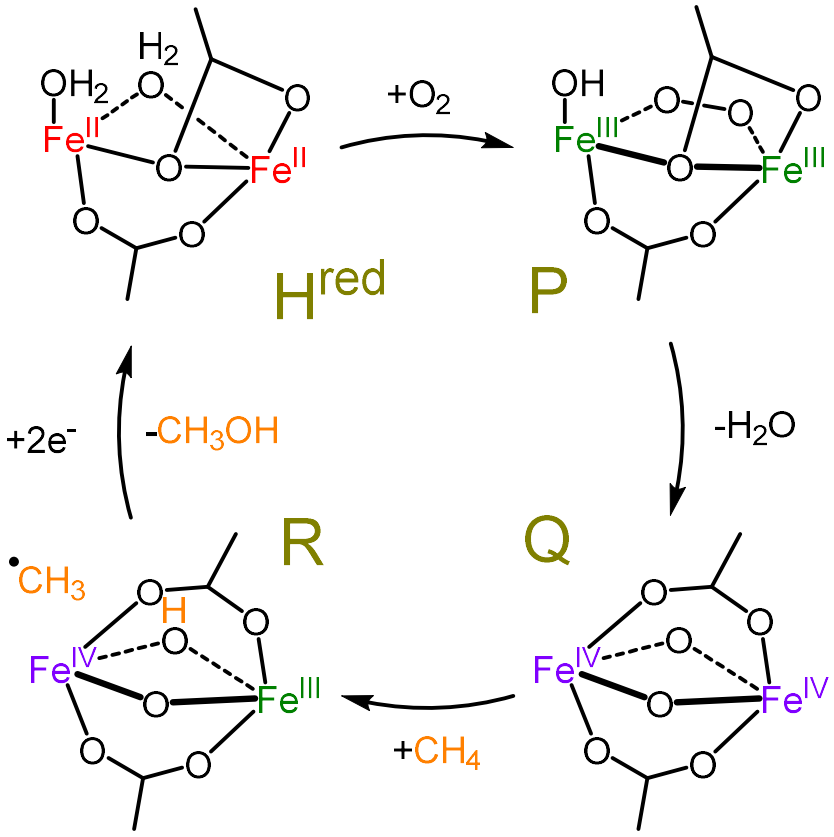

Figure 2. Proposed mechanistic cycle of the oxidation of methane as performed by soluble methane monooxygenase. Non-bridging amino acids and hydrogen bonds have been removed for clarity and simplicity. Additionally, several steps in the mechanistic cycle have also been removed for simplicity.

Arguably, the most interesting structure during the catalytic cycle is the diferryl diamond core proposed for MMOH-**Q**. Initial and ongoing studies from Lipscomb, Münck, Proshlyakov, Que, and many others have led to the assignment of MMOH-**Q** as depicted in Figure 2. This proposed intermediate has undergone thorough characterization using spectroscopic techniques such as UV-Visible, resonance Raman, Mössbauer, electron paramagnetic resonance (EPR), and X-ray absorption spectroscopies, as well as elaborate kinetic experiments to try to elucidate this fleeting intermediate.[21] The different

spectroscopic techniques help to elucidate the catalytic cycle and to try and better understand how nature uses iron and dioxygen to oxidize methane. As previously stated, the structure of **Q** has been the center point of debate in the recent biochemical and bioinorganic literature.[21, 22] The complications associated with the characterization of the intermediate arise from **Q**'s impressive oxidizing potential and thermal instability.

Early Mössbauer and X-ray absorption spectroscopic efforts led to the assignment of **Q** as a diferryl diamond core.[23] These two spectroscopic techniques can be performed on frozen solution samples, making them ideal tools to investigate unstable intermediates such as **Q**. In non-heme iron chemistry, Mössbauer spectra of these oxoiron complexes generally show quadrupole doublets that are characterized by two parameters: the isomer shift (δ), which is indicative of the iron oxidation state, and the quadrupole splitting (ΔE_Q) which reflects the geometry around the iron center. These values provide insight into the oxidation and spin-states of the iron center(s) as well as the centrosymmetry around the iron centers, respectively. Importantly, Mössbauer spectroscopy can give information into all the iron centers present in the sample, so unsymmetric core structures with two distinct iron centers should be distinguishable from one another. In the first reported Mössbauer analysis of **Q**, only one quadrupole doublet was observed, with an isomer shift of δ = 0.17 mm^{-1} s^{-1} and a quadrupole splitting of ΔE = 0.53 mm^{-1} s^{-1}, which led to the conclusion of a reasonably symmetric core consisting of a pair of antiferromagnetically coupled high-spin S = 2 iron(IV) centers.[24] The Fe(IV) centers

of MMOH-**Q** have Mössbauer parameters similar to those of the monoiron enzymes where the Fe(IV)=O centers are typically found to have an $S = 2$ spin state.

X-ray absorption spectroscopy is a synchrotron-based technique that can provide insight into oxidation state, centrosymmetry, and connectivity around the atom of interest. The technique can be broken into two regions: the X-ray absorption near-edge region (XANES) which provides insight into the oxidation state based on the energy of the Kα rising-edge, and the EXAFS region which sheds light on the connectivity of the iron center. Similar to Mössbauer spectroscopy, XANES provides insight into the centrosymmetry of the iron center, as reflected by the area of the pre-edge feature in the XAS spectrum. An increase in the pre-edge area would reflect a deviation from centrosymmetry around the iron center.

For the exploration of intermediate **Q**, the EXAFS data shed more light on the connectivity of the iron centers. EXAFS provides structural information around the iron center. The first EXAFS data for **Q** was reported in 1997 by Lipscomb, Münck, Que, and coworkers, revealing two Fe—O bond distances at 1.77 and 2.05 Å as well as an Fe•••Fe distance of 2.46 Å suggesting the presence of an Fe–O–Fe unit with quite an acute Fe–O–Fe angle.[23]

Since these results were reported, several more enzymatic[21, 25] and synthetic[9] diamond core complexes have been reported, allowing comparison between the enzymatic value and the model complexes. It should be noted that the entries listed in

this table do not have an Fe•••Fe distance as short as the 2.46-Å distance associated with intermediate **Q** but have values closer to 2.7 Å,[9, 25] resulting in greater scrutiny of the original 2.46 Å value reported for **Q**. More than 20 years later, DeBeer and others have developed improved XAS techniques that provide enhanced resolution. DeBeer, Lipscomb and coworkers obtained pre-edge area data indicating the **Q** structure to be more consistent with an open core structure with a terminal Fe^{IV}=O unit that is bridged via an O-atom to another Fe^{IV} center.[26] This assignment of an open core structure was later supported by an Fe Kα high-energy-resolution-fluorescence-detected XAS (HERFD-XAS) EXAFS data that revealed an Fe•••Fe distance of 3.4 Å, approximately 1 Å longer than the originally reported 2.47 Å.[22]

Currently, the structural data is supportive of the open core assignment of **Q**. However, not all the data is supportive of this assignment. Resonance Raman is a technique by which vibrational information can be obtained for vibrations associated with charge transfer bands in the UV-Visible range. These charge transfers can be resonantly enhanced to allow for the observation of low-intensity vibrations. This technique proved useful in the investigation of **Q**, where a vibrational mode at 690 cm^{-1} was observed when the intermediate was generated in the presence of $^{16}O_2$.[27] This feature was found to be isotopically sensitive, red-shifting to 654 cm^{-1} in the presence of $^{18}O_2$ and 673 cm^{-1} in the presence of the mixed-label $^{16}O^{18}O$ isotope of molecular oxygen. It was also demonstrated that both oxygens from the isotope $^{16}O^{18}O$ were retained in the transformation from **P** to **Q**. Beyond this, it was also demonstrated that a labeled oxygen

was incorporated into the product methanol, showing that **Q** is indeed the active oxidant in the system.[28] Lastly, after oxidation had occurred, the now-reduced enzyme active site retained a labeled oxygen in the diferric mono-μ-oxygen intermediate (unshown intermediate between **R** and $\mathbf{H^{red}}$ in Figure 2). This series of experiments and observations beautifully demonstrated that both oxygens of molecular oxygen are incorporated into the active site of sMMO and that there is little to no incorporation of solvent water in the active site upon oxidation.

However, the reported value of 690 cm^{-1} is incongruent with the assignment of the open core structure proposed by DeBeer and coworkers, as a linear structure should have a vibration closer to 800 cm^{-1}.[9] Subsequently in 2021, Solomon, Park, Lipscomb, and coworkers reported an investigation of **Q** using nuclear resonance vibrational spectroscopy (NRVS),[29] a technique distinct from EXAFS. The NRVS data, in conjunction with over 90 DFT model structures, strongly supported the assignment of **Q** as having a diamond core structure, similar to one that was originally proposed but with a computationally calculated Fe•••Fe distance closer 2.7 Å, which would be consistent with model complexes.

At the present time, the precise core structure for intermediate **Q** remains rife with controversy that is not only limited to the spectroscopy but also the reactivity. To date, two model complexes of diferryl diamond cores have been reported but show reactivity that is drastically slower and less oxidizing than **Q**.[30] An important caveat is that the iron centers in the model complexes are $S = 1$, in comparison to the $S = 2$ centers in

Q. To date, a model diamond core complex with high-spin centers has yet to be reported and might prove vital in finally answering the question as to what the true structure of the oxidant **Q** is in soluble methane monooxygenase.

1.4 — Synthetic Models of Monoiron Non-heme Enzymes

1.4.1 — Usage of Polypodal Ligands to Enable the Synthesis of High-Spin Monoiron-Oxo Centers

Due to the high instability of intermediates found in the mechanistic cycles of non-heme iron enzymes, synthetic models have been made to gain insight into these powerful oxidizing species. While the oxoiron(IV) intermediates of enzymes are $S = 2$, most of the reported synthetic intermediates have been characterized as $S = 1$.[9] The first reported high-spin oxoiron(IV) complex was reported by Bakac and coworkers, which was obtained from the reaction of $[Fe^{II}(H_2O)_6]^{2+}$ with O_3 in a highly acidic (pH = 1) aqueous solution at 4 °C.[31] Although only a yield of 50 % was obtainable, its Mössbauer spectrum showed a quadrupole doublet with an isomer shift of 0.38 mm/s and a quadrupole splitting of 0.33 mm/s This isomer shift is clearly distinct from those previously reported $S = 1$ complexes (δ = 0.0 – 0.2)[9] and even more positive than values associated for the $S = 2$ Fe^{IV}=O intermediates of TauD (δ = 0.31 mm/s),[17] prolyl 4-hydroxylase (δ = 0.30 mm/s),[32] phenylalanine-4-hydroxylase (δ = 0.28 mm/s),[33] and tyrosine 3-hydroxylase (δ = 0.25 mm/s).[34]

In subsequent efforts, Borovik, Chang, Que and others have characterized a number of tripodal ligands that support S = 2 oxoiron(IV) complexes.[9] Many of these complexes enforce C_3 symmetry, which lead to the degeneracy of the $3d_{xy}$ and $3d_{x2-y2}$ orbitals. For example, $[Fe^{IV}(O)(TMG_3tren)]^{2+}$ (TMG_3tren = 1,1,1-tris{2-[N^2-(1,1,3,3-tetramethylguanidino)]ethyl}amine) is based on a derivative of the classic tren (Tris(2-aminoethyl)amine) ligand where a tetramethylurea is attached via a carbonyl group to each terminal amine and has a long enough half-life of 4 h at – 30 °C that allows its characterization.[35, 36] EXAFS analysis has found an O scatterer at 1.65 Å and resonance Raman vibration of 843 cm^{-1}, consistent with an oxoiron(IV) complex. Perdeuteration of the ligand methyl groups lead to a long increase in half-life where the self-decay rate was found to have a nonclassical KIE value of 24 at 25 °C.[36] This allowed for the first crystallographic characterization of a high-spin high-valent intermediate where an iron-oxygen bond length of 1.661(2) Å was found. However, Mössbauer spectroscopy reveals a quadrupole doublet with an isomer shift of 0.09 mm/s and a quadrupole splitting of – 0.29 mm/s.[35] The isomer shift value observed falls in the range associated with synthetic S = 1 complexes and at least 0.15 mm/s lower than found for the S = 2 enzyme intermediates. This difference suggests that the geometry of the enzymatic Fe^{IV}=O intermediates are not likely to be trigonal bipyramidal.

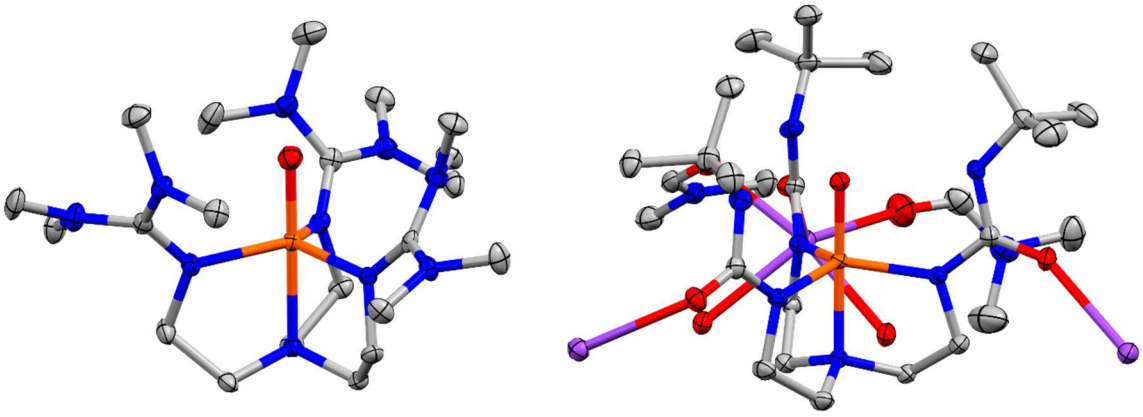

$[Fe^{IV}(O)(TMG_3tren)]^{2+}$ $K^+[Fe^{IV}(O)(H_3buea)]^-$

purple = K^+

Figure 3. Single crystal X-ray diffraction structures of the two characterized *S* = 2 complexes. Adapted from Ref [9] with permission.

Other ligand frameworks that are competent to form a high-spin oxoiron(IV) complex have been investigated. Borovik and coworkers also reported the $[Fe^{IV}(O)(H_3buea)]^{2-}$ complex (H_3buea = tris[(N'-tert-butylureaylato)-N-ethylene]aminato), another trigonal bipyramidal *S* = 2 oxoiron(IV) complex.[37] The H_3buea ligand features a tren-like ligand that can form three hydrogen bonds with the oxoiron(IV) unit. This complex was fully characterized by Mössbauer spectroscopy (δ = 0.02 mm/s, ΔE_Q = 0.43 mm/s), FT-IR and NRVS (ν(Fe=O) = 799 cm^{-1}, 794 cm^{-1}, respectively), and a single crystal X-ray structure with an oxoiron(IV) bond length of 1.680(1) Å.[37] To date, the TMG_3tren and H_3buea ligated oxoiron(IV) complexes are the only crystallized high-spin complexes of their kind.

In 2017 the Bollinger, Krebs, and Boal groups reported a crystal structure of the non-heme iron enzyme L-arginine 3-hydroxylase, VioC with a vanadyl moiety in place of

the ferryl center.[38] This structure provides strong support that the facial triad moiety is bound to one face of the octahedral-like metal center and the oxo and succinate O-atoms occupy the other face.

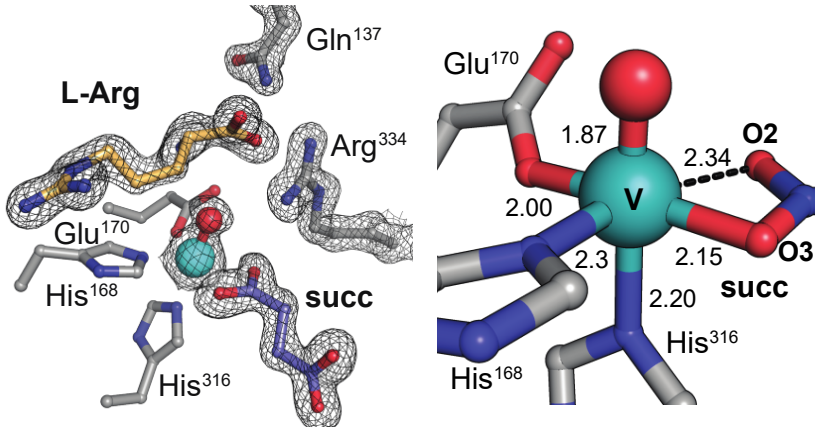

Figure 4. Crystal structure the nonheme iron enzyme L-arginine 3-hydroxylase (VioC) with a stable V^{IV}=O moiety in place of the reactive ferryl unit. Modified from Ref [9] with permission.

It is suggested that the high-spin iron centers in the enzymes are a result of the weak ligand field, which has inspired investigation into the effect of weakening of the ligand field in model complexes. This notion led to an exploration of the effect of the tripodal ligand framework TQA, a sterically more hindered analog of the classic TPA ligand framework that forms a high-spin complex. The TQA ligand employs quinolines in place of the pyridines found in TPA and was found competent to support the formation of the high-valent $[Fe^{IV}(O)(TQA)(CH_3CN)]^{2+}$ complex. However, unlike the complexes of the tren-based tripodal ligands, the $Fe^{IV}(O)(TQA)$ complex gave rise to a Mössbauer quadrupole

doublet with an isomer shift of 0.24 mm/s and a quadrupole splitting of – 1.05 mm/s,[39] parameters more similar to those found for the high-spin *S* = 2 oxoiron(IV) complexes (0.2 – 0.3 mm/s) rather than the *S* = 1 complexes (0.0 – 0.2 mm/s).[9] While structural information was not obtained through XAS or XRD, a DFT calculation shows an oxoiron bond length of 1.64 Å and an experimentally observed bond vibration of 838 cm^{-1}.[39, 40] It is argued that the quinolines in the ligand framework sterically interact with the oxoiron unit, forcing the equatorial metal-ligand bond lengths to elongate, weakening the ligand field to give rise to the high-spin iron center. This hypothesis has been supported when comparing the DFT calculated Fe-N_{ave} distances of 2.15 Å for the TQA complex versus the 1.98 Å for the $[Fe^{IV}(O)(TPA)(CH_3CN)]^{2+}$, which is a well characterized *S* = 1 complex with a near-identical ligand topology.[39, 41] Studies into related TQA-type complexes where the ligating CH_3CN is substituted with a halide, namely Cl and Br, give rise to $[Fe^{IV}(O)(TQA)(Cl)]^{+}$ and $[Fe^{IV}(O)(TQA)(Br)]^{+}$, respectively as models of the ferryl intermediates in halogenase enzymes.[40] Both of these complexes were found by Mössbauer spectroscopy to be high-spin as well, characterized further by resonance Raman (827 cm^{-1} and 828 cm^{-1}, respectively), being the first spectroscopic and functional models of halogenases.[40]

Table 1. Properties of enzymatic and synthetic high-spin oxoiron(IV) complexes.

Complex	*r*(Fe=O) (Å)	ν(Fe=O) (cm^{-1})	δ ($mm\ s^{-1}$)	ΔE_Q ($mm\ s^{-1}$)	half-life (25 °C)	Ref.
Enzymatic Oxoiron(IV) Species						
TauD-***J***	1.62	821	0.31	– 0.88		16-18, 20, 42
P4H	-	-	0.30	– 0.82		32
TyrH	-	-	0.25	– 1.27		34
PheH	-	-	0.28	1.26		33
CytC3-Cl	-		0.30 0.22	– 1.09 – 0.70		43
CytC3-Br	1.62 2.43 (r_{Fe-Br})	-	0.31 0.23	– 1.06 – 0.81		44
SyrB2-Cl	1.66 2.31 (r_{Fe-Cl})	-	0.30 0.23	1.09 0.76		1, 19
SyrB2-Br	-	-	0.29 0.25	1.10 0.77		1
Synthetic Oxoiron(IV) Complexes						
$[Fe^{IV}(O)(H_2O)_5]^{2+}$	-	-	0.38	– 0.33	7 sec	31
$[Fe^{IV}(O)(TMG_3tren)]^{2+}$	1.661	843	0.09	– 0.29	4.3 h (-30 °C)	35, 36
$[Fe^{IV}(O)(H_3buea)]^{-}$	1.680	799	0.02	0.43	2.2 h	37
$[Fe^{IV}(O)(tpa^{Ph})]^{-}$	1.62	850	0.09	0.51	1 h (-40 °C)	45
$[Fe^{IV}(O)(TMG_2dien)(\mathbf{X})]^{2+/+}$						
X = MeCN	1.65	807	0.08	0.58	0.5 h (-30 °C)	46
N_3	-	833	0.12	– 0.30	34 min (-30 °C)	46
Cl	1.65	810	0.08	0.41	2 min (-30 °C)	46
$[Fe^{IV}(O)(TQA)(\mathbf{X})]^{2+}$						
X = MeCN	–	838	0.24	– 1.05	15 min (-40 °C)	39, 40
Cl	–	827	0.22	0.96	5 min (-40 °C)	40
Br	–	828	0.21	0.94	5 min (-40 °C)	40
$[Fe^{IV}(O)(^tBu_3TACN)]^{2+}$	1.66	802	0.11	0.96	20 min (-70 °C)	47

1.4.2 — Overview of *S* = 1 Synthetic Oxoiron(IV) Complexes

In the search for ligand frameworks that enable high-spin oxoiron(IV) complexes, macrocyclic or polypodal frameworks have been used extensively. The interest in monoiron(IV) complexes grew substantially when Que and coworkers reported in *Science* the first oxoiron(IV) complex $[Fe^{IV}(O)(TMC)(CH_3CN)]^{2+}$ (TMC = *N*-tetramethylated cyclam) that was crystallographically characterized.[48] To date, sixteen oxoiron(IV) complexes have been characterized by single crystal X-ray crystallography.[3, 36, 37, 47-56]

The use of this macrocyclic ligand led to many more reports of variations on the TMC framework.[9] Because the TMC ligand is tetradentate and all nitrogens are bound in the equatorial plane (although there are a few exceptions depending on the TMC-derived ligand), a variety of complexes with a range of axial substitutions have been characterized. TMC contains a four methyl groups, each bound to a nitrogen in the framework. Substitution of an H-atom on one these methyl groups with a Lewis basic functional group could give rise to a pentadentate ligand such as TMC-py with a pendant pyridine[50] or TMCS[57] where a pendant thiol group was installed to mimic some heme enzymes where a cysteinate is bound *trans* to the oxoiron unit.[58, 59] When the approximately 40 macrocycle-type oxoiron(IV) complexes are compared, patterns emerge. The Mössbauer isomer shifts of this family of complexes mostly exist within the range of 0.1 and 0.2 mm/s, sometimes nearing 0.0 mm/s for complexes like the $[Fe^{IV}(O)(cyclam\text{-}CH_2CO_2)]^{+}$

complex[60] and even – 0.19 mm/s for the tetraanionic TAML (tetraamido macrocyclic ligand) ligated oxoiron(IV) complex, namely $[Fe^{IV}(O)(TAML)]^{2-}$.[61] The oxoiron(IV) bond lengths range from 1.62 to 1.68 Å, with most of the bond lengths being closer to 1.65 Å and resonance Raman vibrations between 814 and 856 cm^{-1}.[9]

Another family of ligands widely used through literature is the polypodal ligands. The previously discussed TQA and TPA variations are a part of this family, where the TPA and TPA-derivates have been found competent to form monoiron(IV)-oxo complexes.[9] A majority of the characterized complexes feature either tetradentate (ex. TPA) or pentadentate ligand frameworks, with very few ligand frameworks being tridentate. Broadly speaking, two ligand pentadentate ligand frameworks have been found to provide a series of complexes: N4Py and TPEN. The N4Py ligand is arguably a derivative of the TPA framework where one of the pyridine arms has another pyridine bound to it. Similar to TPA, many N4Py derivatives such as N4Py* (3,5-dimethyl,4-methoxy substitutions), $5Me_2N4Py$ (5-methyl substitution), N2Py2Q (two pyridines are replaced with quinolines), have been explored and found to be competent towards supporting high-valent oxoiron species.[9]

The TPEN ligand is tripyridyl ethylene diamine where both amines in the ethylene diamine are trisubstituted with pyridines, making a hexadentate ligand. Many such examples exist where one pyridine is substituted with other functional groups, such as a phenyl ring in BnTPEN or an ethyl group in EtTPEN. There exist many similarities between all the pentadentate complexes. Most of these complexes feature similar Mössbauer,

resonance Raman, and X-ray absorption spectroscopic parameters.[9] Additionally, these complexes tend to have a longer half-life than their tetradentate counterparts, with complexes like $[Fe^{IV}(O)(N4Py)]^{2+}$ having a half-life of 60 h at 25 °C.[53]

The tetradentate frameworks like TPA have been used extensively throughout several decades of work to better understand enzymatic intermediates. While these complexes tend to have low half-lives, on the order of tens of minutes at 10 °C for the $[Fe^{IV}(O)(TPA)(CH_3CN)]^{2+}$ to only a few minutes at – 40 °C for the $[Fe^{IV}(O)(Me_3NTB)(CH_3CN)]^{2+}$ complex, where the Me_3NTB ligand is a TPA-derivative where all the pyridines have been substituted by 2-methylbenzimidazoles.[9] Spectroscopically, these complexes do not differ much from the pentadentate complexes.[9]

However, the tetradentate-ligated oxoiron(IV) complexes are typically significantly more reactive than the related pentadentate-ligated complexes.[9] This leads to an interesting relationship where the pentadentate complexes have proved to be very useful to gain spectroscopic insight into oxoiron(IV) complexes while the tetradentate complexes help understand the reactivity. Additionally, because the oxoiron(IV) pentadentate-ligated complexes are coordinatively saturated, the tetradentate ligands help when understanding the role of *cis* and *trans* substitutions on both the reactivity and spectroscopy of these reactive species.

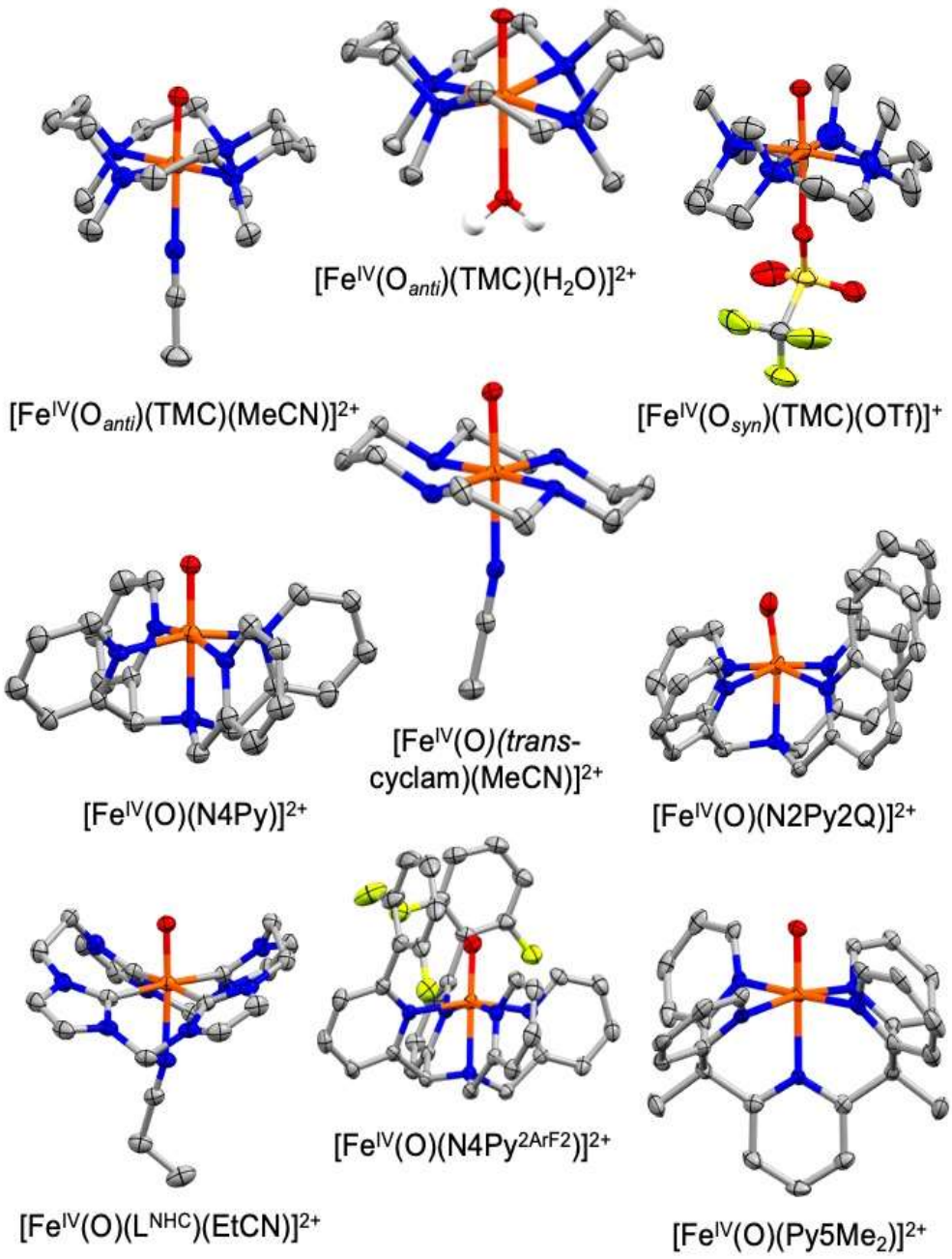

Figure 5. A collection of nine S = 1 $Fe^{IV}(O)$ structures characterized through X-ray crystallography. Adapted from Ref [9] with permission.

1.4.3 — Formation of $Fe^{V}(O)$ Intermediates

Even beyond the high-valent $Fe^{IV}(O)$ complexes $Fe^{V}(O)$ species also exist. A majority of the previously discussed synthetic oxoiron(IV) complexes are formed through the stoichiometric additions of oxygen-atom transfer reagents.[9] Because of the catalytic nature of iron enzymes, efforts towards making model complexes that can perform catalytic transformations has been of great interest. In the field, these higher-valent iron species are typically formed using H_2O_2 and an Fe(III) starting material. Upon the reaction of iron and H_2O_2, a $Fe^{III}(OOH)$ species typically forms. These intermediates are well-known as they have been proposed to be intermediates in the classical Fenton chemistry, which are highly reactive but lack selectivity. Many polypodal and macrocyclic frameworks previously discussed support the formation of this iron-hydroperoxo species, and a majority of them has been characterized by EPR spectroscopy as low-spin $S = 1/2$ iron(III) centers, although there are some outliers with $S = 5/2$ spin states.[9]

These iron(III) intermediates are typically meta-stable, with lifetimes that can be extended at low temperatures. An example is $[Fe^{III}(OOH)(TPA)]^{2+}$, which has an observed λ_{max} at 538 nm and has been well-characterized as a low-spin iron(III)-hydroperoxo species through ESI-MS as well as resonance Raman and EPR spectroscopies.[62-64] Reactivity experiments have suggested that this iron(III) species decays to form a $Fe^{V}(O)(OH)$ species, requiring the participation of water to form this intermediate. This

fleeting intermediate reacts with strong substrates like cyclohexane (BDE = 99.5 kcal/mol) to give the corresponding alcohol and ketone products, suggesting an oxidative transformation.[63] However, this species has yet to directly observed.

There has been great effort in obtaining direct evidence for an $Fe^{V}(O)$ intermediate. Terrence Collins' decades of research on the TAML ligand proved successful in gathering evidence for the to-date best spectroscopically characterized iron(V)-oxo intermediate, namely $[Fe^{V}(O)(TAML)]^{-}$.[65] Independent of Collins' efforts, Costas and coworkers have gathered cryospray ionization mass spectrometry and gas-phase vibrational data for direct evidence of a few $Fe^{V}(O)$ complexes ligated by neutral macrocyclic and polypodal frameworks, as opposed to the tetraanionic TAML ligand.[9, 66-68] Other efforts by Hitomi[69] and many others[70-74] have aided in the understanding of these highly reactive, high-valent iron(V) species.

Recently, pentadentate ligands have been explored in forming $Fe^{III}(OOH)$ intermediates, with the ligand BnTPEN proving very useful in the investigation of iron(V) intermediates.[75] It was found that a sufficiently strong acid could promote the heterolytic activation of the O—O bond in the hydroperoxo intermediate, leading to the putative formation of an $Fe^{V}(O)$ moiety. The BnTPEN framework proved very useful, as the pendant benzyl arm installed in the ligand was found to be susceptible to hydroxylation by the high-valent iron center, resulting in the formation of an Fe^{III}(phenolate) species. A series of experiments were carried out to demonstrate that the putative intermediate is most

likely an $Fe^{V}(O)$ unit that performed the activation of the pendant aromatic ring. This transformation is discussed in greater detail in Chapter 2.

1.5 — Synthetic High-Valent Diiron-Oxo Model Complexes

Inspiration for diiron enzymes came from the efforts of Stubbe and coworkers on ribonucleotide reductase (RNR) R2 that demonstrated the involvement of an Fe^{III}–O– Fe^{IV} intermediate called X as the key oxidant in the mechanism for generating active RNR[76] as well as independent and contemporaneous efforts of Lipscomb and Lippard and their respective collaborators in identifying a diiron(IV) oxidant in the sMMOH mechanism.[21, 24, 77] These active sites share a common 2-His-4-carboxylate first coordination shell that ligates a diiron center and activates O_2. The first synthetic example of an oxo-bridged high-valent diiron core is the $[Fe^{IV}_2(\mu\text{-}O)(TAML)_2]^{2-}$ reported by Collins and coworkers in 2005.[78] The $TAML^{4-}$ ligand is a tetradentate tetraanionic macrocyclic ligand, and two TAML derivatives have been found to give rise to two oxoiron(IV) complexes that were able to be solved structurally through single crystal X-ray diffraction.[78] Bimetallic distances of 3.35 – 3.38 Å and Mössbauer quadrupole doublets with parameters δ = – 0.07 mm/s and ΔE_Q = 3.3 mm/s were found and serve as the starting point for further investigations in $Fe^{V}(O)$ complexes that will be discussed in a later section.

While many other high-valent diiron complexes have been characterized,[9] the employment of the TPA ligand and TPA-like derivatives have proved the most fruitful in understanding high-valent complexes. Early efforts by Que and coworkers resulted in the

observation of an emerald green solution that was characterized as the complex $[Fe^{III,IV}_2(\mu\text{-}O)_2(TPA)_2]^{3+}$.[79] EPR investigations found *g* values consistent with an *S* = 3/2 moiety, implying an unpaired electron is present in the system.[79] Interestingly, Mössbauer spectroscopy showed only one quadrupole doublet with an isomer shift of 0.12 mm/s and a quadrupole doublet of 0.49 mm/s, implying only the two irons were electronically equivalent. This led to the conclusion that the complex is best described as a valence delocalized $Fe^{III}Fe^{IV}$ complex with a resonance Raman core vibration of 666 cm^{-1}.[80] Continued investigation employing $5Et_3TPA$, whereby the pyridines in the TPA ligand each have a methyl substitution in the 5th position, were undertaken. The complex $[Fe^{III,IV}_2(O)_2(5Et_3TPA)_2]^{3+}$ was able to be crystallized and solved with important bond metrics being: two Fe–O bond distances of 1.805(3) Å and 1.860(3) Å, an iron-iron distance of 2.683(1) Å, with an Fe–O–Fe angle of 94.1(1)°.[81]

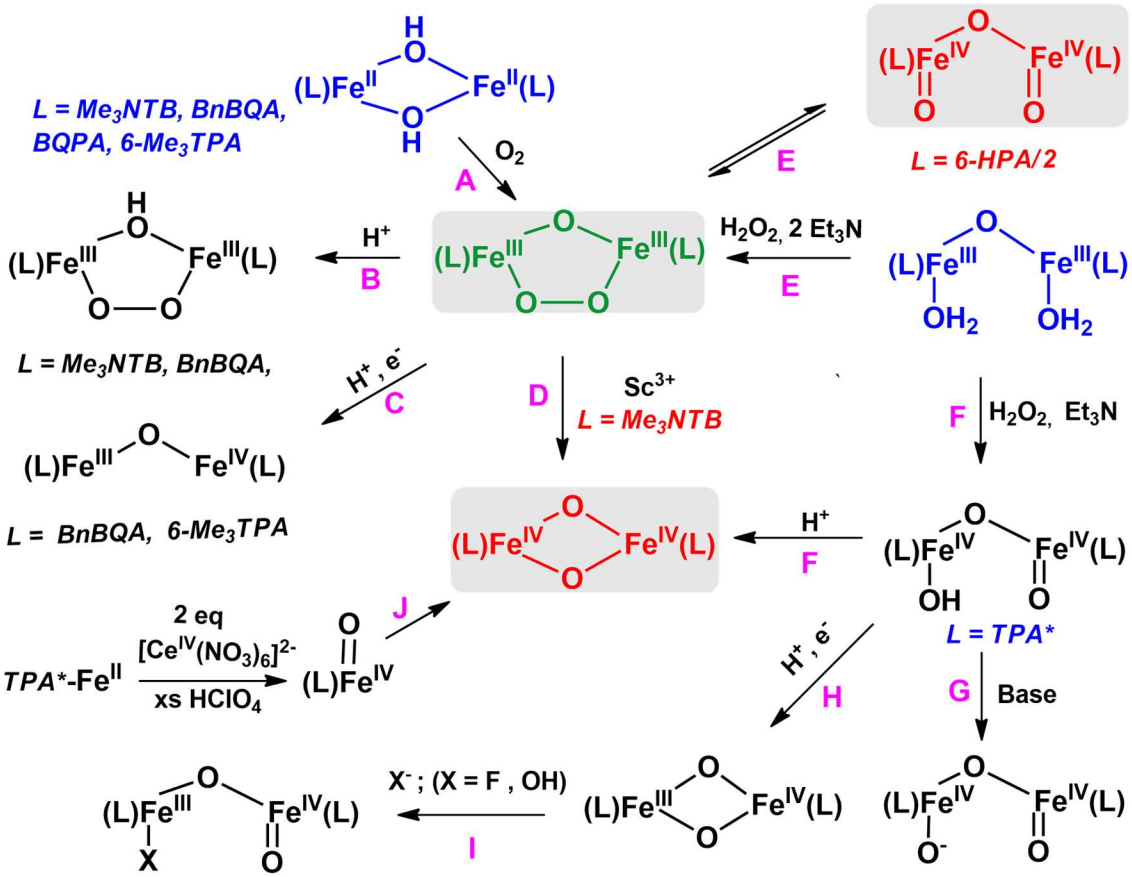

Figure 6. Overview of the many interconversions of diamond core and open core complexes. A: Ref [30, 82]; B: Ref [30, 83]; C: Ref [83, 84]; D: Ref [30]; E: Ref [85]; F: Ref [86]; G: Ref [87]; H: Ref [86, 87]; I: Ref [88-90]; J: Ref [91]. Adapted from Ref [9] with permission.

The TPA derivative that proved to be the most fruitful in exploring high-valent diiron complexes is the electron-rich TPA* ligand where the pyridines are substituted with methyl groups in the 3- and 5-positions and a methoxy group in the 4-position. This ligand gave rise to the first bis-μ-oxodiiron(IV) complex $[Fe^{IV}_2(O)_2(TPA^*)_2]^{2+}$ to be synthesized and was characterized structurally by XAS methods.[92] This complex was subsequently

crystallized and characterized by X-ray crystallography, which gave rise to bond metrics consistent with the initial assignment: two short iron-oxygen bonds of 1.790(6) Å and 1.809(8) Å as well as an Fe•••Fe distance of 2.711(4) Å and an Fe–O–Fe bond angle of 97.8(4)°.[93]

Lower-valent TPA* diiron complexes have also been synthesized and characterized, allowing for comparisons to the diferryl complex. Importantly the ferric/ferryl diamond core complex $[Fe^{III}Fe^{IV}(O)_2(TPA^*)_2]^{3+}$ was characterized by resonance Raman spectroscopy, from which two vibrations at 655 cm^{-1} and 667 cm^{-1} were found, consistent with a closed core species. Recently, this complex has also been characterized by both XAS and X-ray crystallography.[93] The most notable metrics were the diiron distance of 2.596(1) Å and the diamond core bond angle of 92.0(2)°, both structural parameters being found to be actually smaller than the corresponding values for the diferryl complex. These results were surprising and unexpected, as one might expect bond lengths to contract upon an increase in the oxidation state of the iron centers. This has been seen throughout both model and enzymatic complexes, assuming spin state is maintained upon the oxidation of the iron center.[9] One plausible explanation for the longer Fe•••Fe distance in the diferryl complex is the increased electrostatic repulsion between the two higher valent iron centers. More examples may be helpful to understand this phenomenon.

Interesting variations of the synthetic closed core complexes are the corresponding open core derivatives. The open core diferryl complex with terminal hydroxo and oxo groups has been characterized as $[(OH)Fe^{IV}(\mu\text{-}O)Fe^{IV}(O)(TPA^*)_2]^{3+}$ by Mössbauer spectroscopy, showing two quadrupole doublets of equal intensity that have distinct parameters: δ = 0.00(1) mm/s, ΔE_Q = 1.96(3) mm/s; δ = – 0.03(1) mm/s; ΔE_Q = 0.92(2) mm/s.[86] EXAFS analysis revealed an iron-iron distance of 3.32 Å, close to the DFT-predicted distance of 3.38 Å which favors a hydrogen bonding interaction between the terminal hydroxo and oxo units. This complex was found to be approximately 100,000-fold more reactive than the closed core complex in HAT reactions. However, the corresponding lower-valent $[(X)(Fe^{III}(\mu\text{-}O)Fe^{IV}(O)(TPA^*)_2]^{3+}$ (X = OH, F) complexes could be prepared and found to be significantly more reactive than the diferryl complex.[90] Nearly isotropic EPR signals at *g* ~2 supports the fact that this entire complex is a *S* = 1/2 ground state complex, which can be rationalized by the anti-ferromagnetic coupling between a *S* = 5/2 Fe^{III} and a *S* = 2 Fe^{IV}. This effort showed that the addition of a hard anion like hydroxide OR fluoride can perturb the spin state of the iron center from *S* = 1 to *S* = 2. In fact, ^{19}F superhyperfine splitting was observed by EPR, showing that the fluoride ion couples to the unpaired electron in the system. Comparing the two anion partners, the iron-iron distance contracts from 3.56 Å for the fluoride-bound complex to 3.32 Å for the $[(OH)Fe^{IV}(\mu\text{-}O)Fe^{IV}(O)(TPA^*)_2]^{3+}$ complex, providing evidence for the previously hypothesized hydrogen bonding interaction between the terminal hydroxide and oxo units.[86, 90]

Notably, the HAT reactivity of this open-core mixed-valent complex slightly surpasses that of the $[Fe^{IV}(O)(TQA)]^{2+}$ complex, which to date is still the most reactive monoiron complex which was discussed previously in this work.[39] When looking at the controversy surrounding the nature of the core structure in sMMO, these efforts demonstrate that the open core species are more reactive towards HAT than the closed-core counterparts in synthetic models. These reactivity data suggest that a yet unseen open core species may exist for **Q**, which performs the required hydrogen atom abstraction on methane but has yet to be trapped and characterized due to its high reactivity.

1.6 — Conclusion

A variety of synthetic complexes has been investigated to better understand how Nature can design specialized active sites for important physiological transitions. Through the analysis of high-valent species, both monoiron and diiron, it has been possible to gain insight into how these sites can activate oxygen to transform organic substrates.

In this thesis, spectroscopic and reactivity explorations have been carried out on synthetic complexes to mimic enzymatic intermediates and understand their chemistry. High-valent iron-oxo complexes have been synthesized and then characterized by a combination of UV-Vis, resonance Raman and X-ray absorption spectroscopies, as well as by X-ray diffraction. Chapter 2 describes studies on the usage of a strong acid to activate the O—O bond in the $[Fe^{III}(OOH)MeTPEN]^{2+}$ complex to perform interesting desulfonation

and oxidative transformations. Chapter 3 focuses on a series of diiron complexes coordinated by the TQA ligand, which were synthesized and characterized spectroscopically in an effort to gain insight into the sMMO-**Q** intermediate and the pathway through which this powerful species is formed. Lastly, Chapter 4 describes a series of pentadentate oxoiron(IV) complexes, which have been explored to gain insight into how steric interactions on the oxoiron unit can perturb the spectroscopic properties of these complexes and control their reactivity. Lastly, the first what kind of complex with a bound imidazole is characterized by its spectroscopic properties and its reactivity.

Chapter 2: Oxidative Desulfonation of an Aromatic Ring by a High-Valent Iron-Oxo Complex

2.1 — Introduction

Iron-containing enzymes are competent in performing a wide variety of transformations, including difficult oxidations that are typically performed by a high-valent iron-oxo species. These high-valent species are commonly formed as a result of the heterolytic cleavage of an H_2O_2- or O_2-derived O–O bond found in peroxoiron complexes. A well-studied example is the formation of the highly reactive "Compound I" (Cpd I), a $Fe^{IV}(O)(por^{+\bullet})$ species that is proposed to be the active oxidant found in the catalytic cycles of heme systems such as cytochromes P450 and peroxidases, resulting from heterolytic cleavage of the O–O bond of a low-spin S = ½ Fe^{III}–OOH intermediate (Compound 0, Cpd 0).[6, 94] This cleavage is found to require the participation of a proton, typically delivered by a nearby amino acid residue in the distal pocket of the enzyme. In synthetic models, there are less than a handful of bioinspired complexes where the participation of a proton has been investigated in the cleavage of the O–O bond in the Cpd 0-like intermediates. In a synthetic heme system, Van Eldik and coworkers have investigated an octa-anionic porphyrin found competent to form an Fe^{III}–OOH intermediate,[95] which subsequently undergoes pH-dependent O–O bond cleavage to form high-valent derivatives. They report a switch in mechanism at pH 8.5, where homolytic cleavage is observed in more alkaline solutions to form $^{\bullet}$OH, while the 2-electron oxidation similar to that observed for the heterolytic cleavage found in the transformation of Cpd 0 to Cpd I is found to occur at a pH below 8.5. Interestingly, in a non-heme system recently investigated by Xu *et al.*, a similar switch in mechanism is

found in the case of $[Fe^{III}(OOH)(BnTPEN)]^{2+}$ with acids having pK_a < ~8.5 (in CH_3CN) where thermodynamic parameters derived from Eyring analyses consistent with heterolytic cleavage are observed, while acids less acidic than pK_a of 8.5 give rise to observations consistent with O–O bond homolysis.[75] These results necessitate more investigation into the activation of O–O bonds and exploration into whether iron-containing complexes are competent towards performing desulfonation.

2.2 — Formation of 2 with HOAc and H_2O_2 at 25 °C

Similar to BnTPEN, the modified TPEN-type framework MeTPEN has been ((N-methyl-N,N',N'-tris(2-pyridylmethyl)-1,2-diaminoethane) employed in this work. It has been shown previously that for pentadentate ligand frameworks, upwards of 100 equiv of H_2O_2 are required to form an iron(III)-hydroperoxo intermediate in good yield.[96] However, more recently, Xu *et al.* demonstrated that the addition of 10 equiv HOAc prior to the addition of H_2O_2 facilitated the formation of the Fe^{III}–OOH intermediate ligated by a pentadentate framework BnTPEN.[75] This strategy was employed in the present work. The addition of the weak acid HOAc (pK_a = 23.5 in CH_3CN) to the solution prior to the addition of only 10 equiv of H_2O_2 enabled the observation of the formation of the absorption feature associated with $[Fe^{III}(OOH)(MeTPEN)]^{2+}$ (λ_{max} = 500 nm) (**2**), similar to the value previously found for $[Fe^{III}(OOH)(BnTPEN)]^{2+}$ and previously reported for $[Fe^{III}(OOH)(MeTPEN)]^{2+}$ in MeOH (Figure 7).[97, 98]

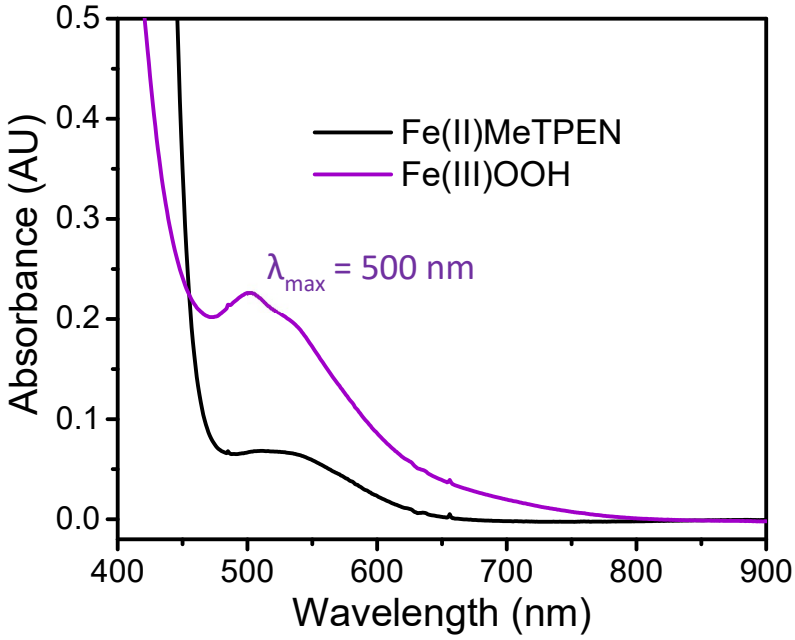

Figure 7. UV-Vis spectrum associated with the addition of 10 equiv of HOAc and 10 equiv of 90 % H_2O_2 to a solution of 1 mM $[Fe^{II}(MeTPEN)(CH_3CN)]^{2+}$ in CH_3CN at 25 °C.

2.3 — Reaction of 2 with Strong Acids

It has been demonstrated that the addition of a strong acid to a Fe^{III}-OOH intermediate can promote the heterolytic cleavage of the O–O bond, unleashing a putative terminal $Fe^{V}(O)$ oxidant capable of hydroxylating strong C–H bonds like those found in cyclohexane (BDE = 99.5 kcal/mol).[75, 99] In the BnTPEN system, a phenolate species has been shown to form upon the addition of 1 equivalent of strong acid to the Fe^{III}–OOH intermediate where the pendant benzyl arm is hydroxylated and then becomes coordinated to the iron center, providing strong indirect evidence for the generation of a

$Fe^{V}(O)$ oxidant.[75] This $Fe^{III}(OAr)$ species has been found to be *ortho*-hydroxylated and associated with a broad optical feature centered at 680 nm (ε ~2000 M^{-1} cm^{-1}), typical of Fe^{III}-phenolate species.[100] In the MeTPEN system, it is observed that the addition of 1 equiv of HOTf (pK_a = 2.6 in CH_3CN) results in the decay of **2** within a few seconds at 20 °C, similar to what has been observed in previous studies.[75, 99] However, MeTPEN features a methyl group in place of the pendant benzyl arm that is present in the BnTPEN framework, so no phenolate species can be formed upon the addition of strong acids such as HOTf and 70 % $HClO_4$ (pK_a = 1.57 in CH_3CN)[101] to **2**. However, the addition of p-toluenesulfonic acid (TsOH, pK_a = 8.5 in CH_3CN)[102] results in the generation of a visible chromophore at 640 nm, similar to that observed upon addition of strong acids to Fe(BnTPEN), including TsOH, which is the least acidic additive found competent to cleave the O–O bond heterolytically in the BnTPEN system.[75]

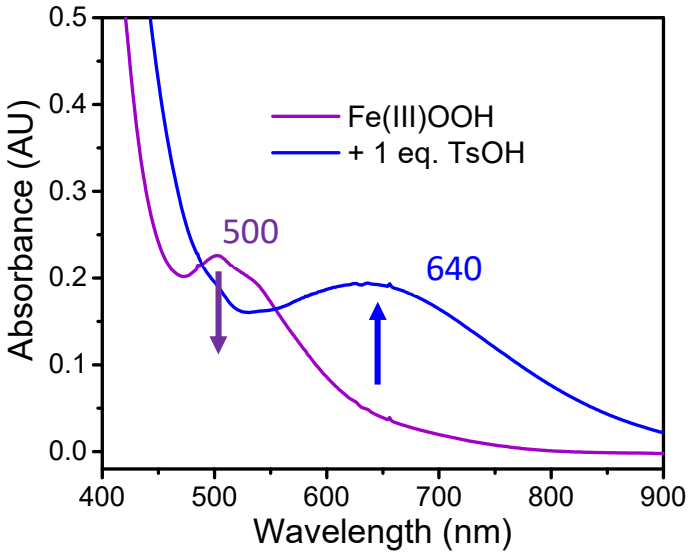

Figure 8. UV-Vis spectrum associated with the addition of 1 equiv TsOH acid to the intermediate 2 in CH_3CN at 1 mM with respect to Fe^{II} starting complex.

The rate of disappearance of the chromophore associated with **2** upon the addition of 1 equiv TsOH is similar to the rate observed upon the addition of 1 equiv of HOTf, demonstrating that the weaker acid TsOH is sufficient to promote the heterolytic cleavage previously reported. The decay rate of this species with 0.5 equiv TsOH is found to be about 0.4 s^{-1} at – 40 °C. However, when TsOH is employed, a broad chromophore centered at 640 nm is observed by UV-Vis spectroscopy (Figure 8). This feature resembles the self-hydroxylated phenolate product observed in the BnTPEN system, but the MeTPEN ligand features no pendant benzyl arm that can be hydroxylated. Similarly, the use of 4-chlorobenzenesulfonic acid (4-Cl, pK_a = 7.16 in CH_3CN)[101] in place of TsOH gives rise to a similar broad feature (λ_{max} = 610 nm), demonstrating the hydroxylation of the aromatic rings in the benzenesulfonic acids and their subsequent coordination to the Fe^{III} center to give rise to the broad Fe^{III}(OAr)-like feature found in Figure 8. This is an unexpected development, as it has not been previously demonstrated that these non-heme synthetic complexes can perform hydroxylation on an arene ring at such low equivalences.

Additional investigation has been carried out to characterize the nature of this intermediate, initially hypothesized to be an iron(III)-phenolate derivative, due to the similarity in the spectral features. On the other hand, the use of 4-chlorobenzenesulfonic acid in place of TsOH gives rise to a similar broad feature with a formation of a phenolate-bound species in about 10 % yield (assuming ε = 2000 M^{-1} cm^{-1}) with respect to the starting

Fe^{II} complex. The absorbance value doubles when 2.5 equiv of TsOH is employed (Table 2).

Table 2. Optical parameters associated with the UV-Vis spectroscopic features of the products formed upon the addition of 2.5 equiv benzenesulfonic acid reacted with **2** (Col. 2, -40 °C) or approximately 10 equiv phenol to starting Fe^{II} material in the presence of atmospheric oxygen (Col. 3, 20 °C). All experiments are normalized to 3 mM [Fe^{II}] and carried out in CH_3CN.

Substitution	**benzenesulfonic acid λ_{max} (nm) / Abs.**	**Phenol λ_{max} (nm) / Abs.**
1,3,5-Me^3	680 / 0.6 (1 equiv)	-
4-Me	643 / 1.2	638 / 1.2
4-Cl	610 / 1.4	600 / 1.2
4-H	590 / 1.6	585 / 1.9
4-F	585 / 0.2 *(sh)*	590 / 1.6
4-NO_2	no formation	-

We hypothesize that the added TsOH becomes hydroxylated, generating the observed chromophore in one of three positions on the aromatic ring: ortho (A), meta (B), or *ipso*-like (C) hydroxylation (Figure 9). Another benzenesulfonic acid derivative 2-mesitylenesulfonic acid (2-Mes) has also been employed as an additional probe, as this acid has substituents in the positions *ortho* and *para* to the sulfonate that block hydroxylation at these positions. Despite its slightly lower acidity, 2-Mes is still found to promote the heterolytic cleavage of the O–O bond, as a broad feature similar to the one found in Figure 8 as well as other Fe^{III}-phenolate species is observed (Figure 15) upon the

addition of 1 equiv of 2-Mes to intermediate **2**. As the *ortho* positions of its arene ring are substituted in 2-Mes, a demethylation would have to occur to form product A. The observation of the formation of this Fe^{III}-phenolate-like intermediate eliminates the possibility of speciation A in this reaction (Figure 9).

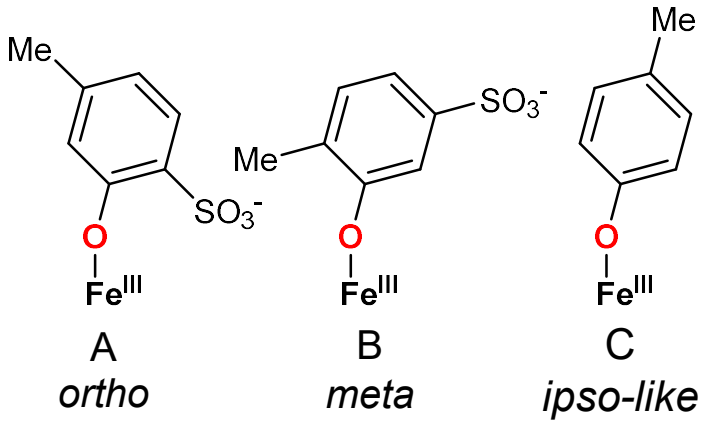

Figure 9. Proposed possible products formed upon the hydroxylation of TsOH that give rise to the broad chromophore observed at 640 nm.

2.4 — Fe^{III}-phenolate Generation and Spectroscopic Characterization

The hypothesis that a Fe^{III}-phenolate product is formed requires a mechanism for its generation from the aryl sulfonate precursor (Figure 10). A series of *para*-substituted phenols has been chosen because they are analogues for the *ipso*-like product generated from the benzenesulfonic acids employed in this study (Figure 9C). The less acidic phenols *p*-cresol and 4-chlorophenol (pK_a's = 27.5 and 25.4, respectively)[101] have been employed as these are direct desulfonated and hydroxylated analogues to TsOH and 4-Cl (Figure 9C). When these phenols are reacted with starting Fe^{II} complex in the presence of air,

broad features associated with Fe^{III}–phenolates are observed to form over several minutes in the UV-Vis region with varying λ_{max} and absorbances. These optical parameters are found to be nearly identical to the analogous reactions of TsOH or 4-chlorobenzenesulfonic acid added to the intermediate Fe^{III}–OOH species, giving rise to distinct Fe^{III}-phenolate species (Table 2). These results suggest that the strong acid used to promote to O–O bond cleavage of intermediate **2** also acts as a substrate where the sulfonate group is replaced with a hydroxyl group that subsequently coordinates to the Fe^{III} center to give rise to the broad feature observed in the UV-Vis spectrum (Figure 8).

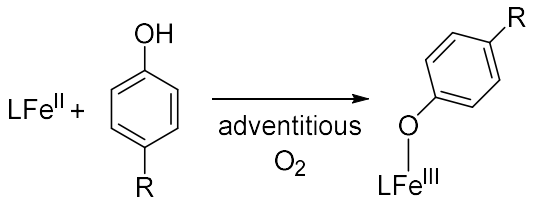

Figure 10. Generation of a generic LFe^{III}-phenolate species formed by the addition of a generic *para* substituted phenol to LFe^{II} starting material in the presence of air, where L = MeTPEN.

The resonance Raman spectra for the products formed from both the benzenesulfonic acid-containing reactions and analogous phenol reactions show that the various Fe^{III}(OAr) species each give rise to vibrations near 600 cm^{-1} that can be readily associated with an Fe–OAr bond.[103] Furthermore, there are additional vibrations in the 1100-1700 cm^{-1} region that arise from phenolate ring deformation modes.[103] In the lower energy region, there is good agreement between spectra 3 and 4, where the Fe^{III}-

phenolate features a methyl substitution *para* to the iron-oxo bond on the arene ring. A single vibration is observed at ~560 cm^{-1}. This is noticeably different from spectra 1 and 2 where a chloro substituent is present *para* to the iron-oxo bond. Two distinct features are observed at ~485 and 703 cm^{-1}, whereas the 560 cm^{-1} vibration is not observed. This set of spectra clearly demonstrates that the product formed upon oxidation of the benzenesulfonic acid is identical to the product formed upon the reaction of phenol and iron complex in the presence of air. Additionally, these pairs of spectra (1 & 2, 3 & 4) are distinct from one another, indicating that the functional group is preserved on the phenolate ring (Figure 11). The phenolate ring deformation regions obtained in this study feature fewer vibrations when compared to spectra reported for *ortho*-substituted phenolate ligands due to the loss of 2-fold symmetry upon *ortho*-substitution the gives rise to more vibrations in the spectra for these complexes.[75] Additional vibrations associated with a lower symmetry complex would also be expected in a *meta*-substituted phenolate species, supporting the elimination of speciation B in Figure 9. The chloro-substituted spectra also feature a unique vibration at 1092 cm^{-1}, not observed in spectra 3 and 4 (Figure 11). These Raman results in conjunction with the UV-Vis results leave two options for the hydroxylation site when intermediate **2** is reacted with benzenesulfonic acids: either the benzenesulfonic acid is being hydroxylated at the 4-position, or the putative sulfonate after deprotonation is being replaced with a hydroxyl group, giving rise to the *ipso*-like product C in Figure 9. The former option is unlikely due to this position being occupied by a methyl group in the case of TsOH and 2-Mes or a chloro group in the

case of 4-chlorobenzenesulfonic acid. Additionally, if these methyl and chloro groups were displaced in TsOH and 4-chlorobenzenesulfonic acid, respectively, the resulting Fe^{III}-phenolate product should be identical and therefore give rise to the same vibrational and optical spectra, which is not what is observed. Lastly, the differences in the UV-Vis parameters tabulated in Table 2 further support the notion that the sulfonate group present in the benzenesulfonic acids employed has been replaced by a hydroxyl group and coordinating to the Fe^{III} center to give rise to a series Fe^{III}(OAr) intermediates.

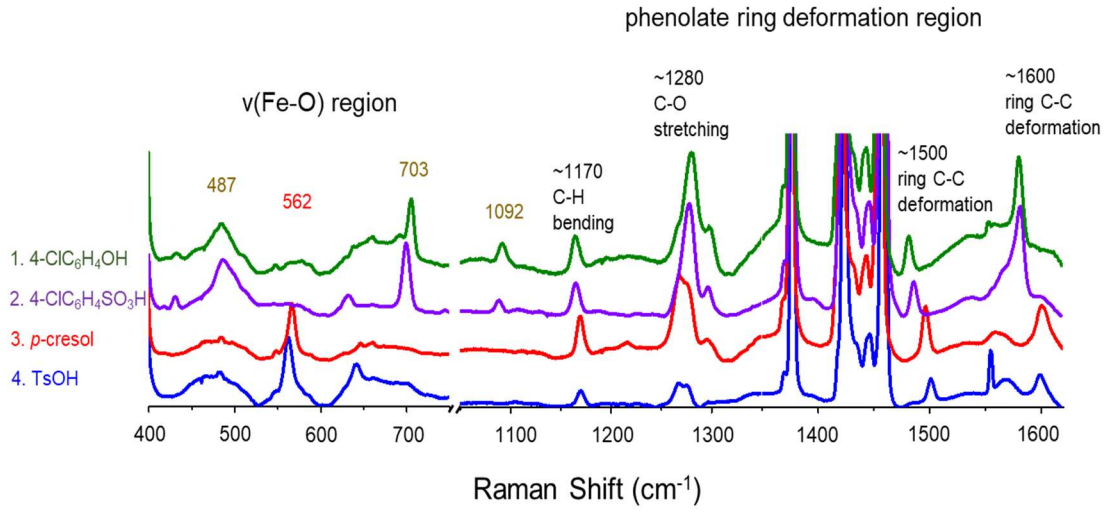

Figure 11. Resonance Raman spectra of the phenolate product when intermediate **2** was reacted with 4-$ClC_6H_4SO_3H$ (2, purple) or TsOH (4, blue) compared to the product generated when Fe^{II} starting material is reacted with 4-ClC_6H_4OH (1, green) or p-cresol (3, red) in the presence of atmospheric oxygen. All values labeling vibrations are in units of cm^{-1}. Values in gold (487, 703, 1092 cm^{-1}) are associated solely with spectra 1 and 2, while the value in red (562 cm^{-1}) is associated with spectra 3 and 4. Values above 1100 cm^{-1} are associated with all spectra. All spectra were obtained in CH_3CN at 77 K with 561 nm laser excitation. Reaction conditions for 2, 4: 3 mM **2**, 10 equiv HOAc, 2.5 equiv 4-$ClC_6H_4SO_3H$ (spectrum 2) or TsOH (spectrum 4) in CH_3CN at 233 K; reaction conditions for 1, 3: 3 mM **1**, 10 equiv 4-ClC_6H_4OH (spectrum 1) or *p*-cresol (spectrum 3) in CH_3CN at 298 K.

2.5 — Mechanistic Investigation

Due to the observation of this unprecedented reactivity, the mechanism for the formation of the desulfonated product has been investigated to further understand this novel transformation. The initial steps of the mechanism likely follow what has been

proposed initially in the BnTPEN system for the formation of the putative $Fe^{V}(O)$ intermediate.[75] Firstly, **2** forms within minutes upon the addition of acetic acid and hydrogen peroxide at room temperature to a solution containing **1**. The solution is then cooled to – 40 °C and allowed to equilibrate (Figure 7). Upon addition of a sufficiently strong acid (pK_a < ~8.5), **2** immediately decays to generate the putative $Fe^{V}(O)$ oxidant upon the heterolytic cleavage of the O–O bond. Neither HOTf nor $HClO_4$ elicits a new chromophore upon the decay of the chromophore associated with **2**. However, when a benzenesulfonic acid is employed as the strong acid, a new chromophore is formed with a λ_{max} dependent on the nature of the substituent present on the aromatic ring of the acid (Table 2). Eyring analysis has been carried out to shed light on the mechanism by comparing the $\Delta H^{‡}$ values to those reported where the O–O bond cleavage has been thoroughly investigated. This series of Eyring analyses currently represents the most thorough investigation of the O–O bond cleavage mechanism for two similar ligand frameworks (MeTPEN and BnTPEN) compared to current values reported in literature (Table 3). These thermodynamic parameters herein are used to explore whether a mechanistic difference between the benzenesulfonic acids and other Brønsted acids explains the new series of chromophores observed in the UV-Vis trace. Thermodynamic parameters found for a solution of **2** when reacted with $HClO_4$, HOTf, TsOH, or 2-Mes are reported herein. Expectedly, it is observed that all four of the latter acids give rise to parameters associated with O–O bond heterolysis, consistent with parameters found for previous experiments with the BnTPEN system and other similar systems (Table 3). When

the same acid, namely HOTf, is used in both the BnTPEN and MeTPEN systems, the thermodynamic parameters observed are quite similar. These lower $\Delta H^{\ddagger}$ values (< ~40 kJ mol^{-1}) are in contrast to those for the self-decay of **2**, which are found to be 65 and 81 kJ mol^{-1} in the presence or absence of acetic acid, respectively.[104] The parameters found for the self-decay of **2** ($\Delta H^{\ddagger}$ = 65 kJ mol^{-1}) are consistent with O–O homolysis, as previously reported for the self-decay pathway of **2** in the absence of substrate or acid.[104] An interesting observation is that an increase in the acidity of the acid employed results in a smaller observed $\Delta H^{\ddagger}$. Previous results with the BnTPEN system have demonstrated that an inverse H/D KIE of 0.9 is observed with $DClO_4$ employed in place of $HClO_4$.[75] This result supports the participation of the H/D proton in the rate determining step of O–O bond heterolytic cleavage and may be related to the smaller $\Delta H^{\ddagger}$ as the pK_a of acid decreases in the present MeTPEN system.

An important distinction between the BnTPEN and MeTPEN is the chromophore used to follow the reaction kinetics. In the BnTPEN system, the kinetics is monitored by following the formation of the Fe^{III}-phenolate chromophore upon addition of strong acid, while in the MeTPEN system, the kinetic data is obtained by monitoring the decay of the Fe^{III}(OOH) chromophore. Despite this difference, nearly identical Eyring parameters are observed. A third system has also been studied that involves Fe^{III}-phenolate formation by the intermolecular hydroxylation of 2-Mes, and this system also gives rise to comparable Eyring parameters. These three sets of data give rise to nearly identical Eyring parameters, which compare well with the thermodynamic parameters found for other heterolytic O–

O cleavage mechanisms (Table 3). These observations underscore the notion that the rate determining step in these reactions all involve a rate-determining heterolytic O–O cleavage. These findings demonstrate that the class of benzenesulfonic acids used maintain the O–O bond heterolytic cleavage pathway, therefore unleashing a putative $Fe^{V}(O)$ intermediate that then is competent to perform difficult oxidative transformations.

To demonstrate that the putative $Fe^{V}(O)$ is capable of hydroxylating aromatic substrates, an experiment is performed where 1 equiv of $HClO_4$ is added concomitantly with 200 equiv of benzene to intermediate **2**. Upon the addition of both acid and substrate, a chromophore centered at ~590 nm forms immediately (Figure 12). This spectral feature is nearly identical to those reported in Table 2 where benzenesulfonic acid has been employed, demonstrating that the putative high-valent iron-oxo species is competent in hydroxylating external aromatic substrates. This observation also supports the previous proposal that the benzenesulfonic acids are desulfonated and hydroxylated to form an Fe^{III}-phenolate product.

Table 3. Eyring parameters for the decay of (L)Fe^{III}–OOR complexes (solvent is CH_3CN unless otherwise specified).

Reaction	$\Delta H^{\ddagger}$ (kJ/mol)	$\Delta S^{\ddagger}$ (J/(K·mol))	proposed O–O bond cleavage mode	Ref
(MeTPEN)Fe^{III}-OOH	81	– 1	homolysis	[104]
(MeTPEN)Fe^{III}-OOH + HOAc	65	– 73	homolysis	this work
(MeTPEN)Fe^{III}-OOH + HOAc + $HClO_4$	15	– 186	***heterolysis***	this work
(MeTPEN)Fe^{III}-OOH + HOAc + HOTf	25	– 146	***heterolysis***	this work
(MeTPEN)Fe^{III}-OOH + HOAc + TsOH	30	– 133	***heterolysis***	this work
(MeTPEN)Fe^{III}-OOH + HOAc + 2-Mes	41	– 88	***heterolysis***	this work
(BnTPEN)Fe^{III}OOH	53(2)	– 72(8)	homolysis	[75]
(BnTPEN)Fe^{III}-OOH + HOAc	52(2)	– 108(10)	homolysis	[75]
(BnTPEN)Fe^{III}-OOH + HOAc + HOTf	30(2)	– 118(20)	***heterolysis***	[75]
(BnTPEN)Fe^{III}-OOH + HOAc + 2-Mes	40	– 91	***heterolysis***	this work
(N4Py)Fe^{III}-OOH in acetone/CF_3CH_2OH	53(1)	– 121(2)	homolysis	[105]
(bbpc)Fe^{III}-OOH	53(1)	– 68(4)	homolysis	[106]
(TPA)Fe^{III}-OO^tBu	52(1)	– 74(3)	homolysis	[107]
(TPA)Fe^{III}(κ^2-$O_2C(CH_3)_2OH$) in acetone	54(3)	– 35(13)	homolysis	[108]
(TPA)Fe^{III}-OOH	45(2)	– 95(10)	***heterolysis***	[109]
($PyNMe_3$)Fe^{III}-OOH	44(3)	– 138(12)	homolysis	[110]
($PyNMe_3$)Fe^{III}-OOH + 1.1 equiv of HOTf	46(4)	– 79(13)	***heterolysis***	[110]
(14-TMC)Fe^{III}-OOH in acetone/CF_3CH_2OH	56(2)	– 75(2)	homolysis	[105]
(14-TMC)Fe^{III}-OOH + $HClO_4$	44(2)	– 90(10)	***heterolysis***	[111]

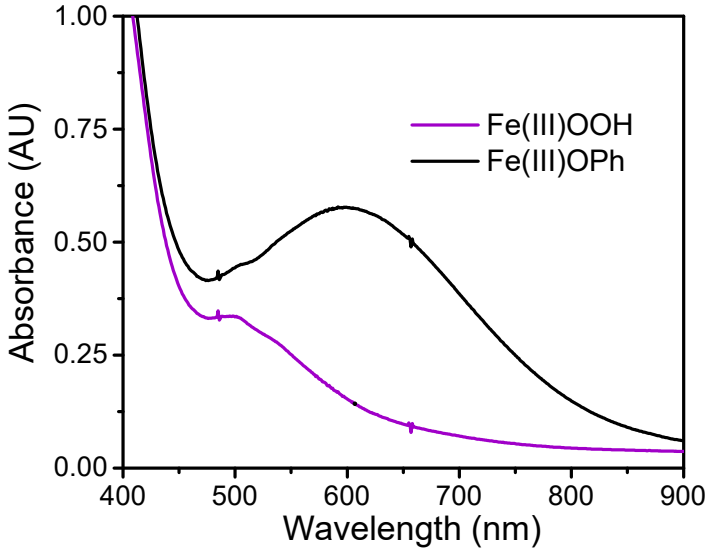

Figure 12. UV-Vis spectrum associated with the addition of 1 equiv $HClO_4$ acid concomitantly with 200 equiv benzene to the intermediate **2** in CH_3CN at 1 mM with respect to Fe^{II} starting complex at 20 °C

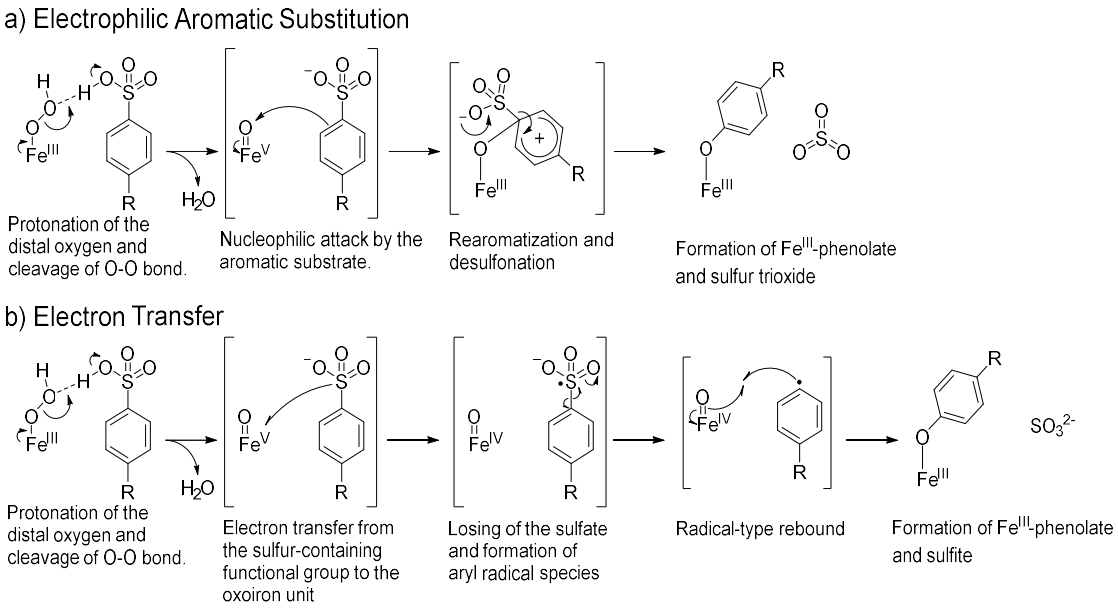

Figure 13. Proposed mechanisms for the hydroxylation of the benzenesulfonate species

As discussed earlier, it is most likely that the intermediate $Fe^{III}(OOH)$ that is formed in the reaction pathway subsequently undergoes O–O heterolysis upon the addition of a strong acid, unleashing a putative $Fe^{V}(O)$ oxidant. Thus, the classical aromatic desulfonation mechanism of sulfonic acids in the presence of a strong acid can be used as a framework for the proposed mechanism **a** in this work to rationalize the observed reactivity associated with the high-valent metal-based oxidant. Classically, a nucleophilic attack by the aromatic substrate by an electrophile typically results in a Wheland intermediate where a carbocation is delocalized on the aromatic ring and the electrophile is bound geminal to the sulfonate.[112] This Wheland intermediate can then be stabilized by electron-donating substituents on the aromatic ring, and rearomatization of the benzene ring occurs contemporaneously with the expulsion of the sulfonate as SO_3.

This mechanism parallels our proposed mechanism where the electrophile in our system is the putative $Fe^{V}(O)$ species, formed upon the heterolytic cleavage of the O–O bond (Figure 13). The $Fe^{V}(O)$ oxidant is proposed to undergo a nucleophilic attack by the benzenesulfonate, forming a transient Wheland-like intermediate where the terminal oxo species is bound geminally to the sulfonate. This transformation is likely to rapidly undergo rearomatization, whereby sulfonate is expelled as sulfur trioxide and a Fe^{III}-phenolate is formed.

Further, support for the formation of a Wheland-type intermediate comes from the observed effect of the *para* substituents. The formation of the final Fe^{III}-phenolate product is severely inhibited or altogether prevented with the introduction of electron

withdrawing fluoro or nitro groups (Table 2), which strongly supports the proposal of a resonance stabilized carbocation-type intermediate in the reaction pathway that is destabilized by the electron-withdrawing groups. These electronic effects are consistent with what has been shown computationally where the charge distribution of Wheland-type intermediates favors the percent charge being most present on the positions para and ortho to the location of aromatic substitution.[112] Therefore, the poor yield in the formation of phenolates with electron withdrawing substituents supports the formation of a Wheland-type intermediate, as electron-deficient aromatic rings cannot support formation of the aromatic carbocation species. In contrast, the electron-donating groups employed in this study all result in product formation of an Fe^{III}-phenolate, as these substituents are competent towards supporting an intermediate Wheland-type species (Table 2). Taken together, these data support the proposed mechanism **a** in Figure 13.

While hydroxylations of aromatic substrates have long been reported in both synthetic and biological systems,[10, 11, 113] a recent investigation into intramolecular aromatic hydroxylation performed by an $Fe^{IV}(O)$ oxidant has been reported in which the authors propose a Wheland-type intermediate that coordinates to the iron center upon the electrophilic attack of the high-valent iron-oxo moiety on the aromatic ring.[4] This intermediate undergoes rearrangement followed by an H-atom abstraction to result in the observed Fe^{III}-phenolate species. In the present work, the oxidation state of the putative iron-based oxidant is proposed to be iron(V) that forms upon heterolytic cleavage of the O–O bond after the addition of an acid to **2**. Such putative iron(V)-oxo

complexes are competent towards electrophilic aromatic substitution as proposed in the present work as well as in the literature, in both intra- and inter-molecular hydroxylation.[75, 99] In these scenarios, the $Fe^{V}(O)$ oxidant is proposed to perform an electrophilic attack on the aromatic ring, forming a Wheland-type intermediate similar to what has been proposed herein (Figure 13). This putative intermediate then undergoes re-aromatization, expelling a suitable leaving group. In the proposed desulfonation mechanism, the expelled leaving group is proposed to be SO_3, parallel to what has been observed in the classical desulfonation mechanism. It is then most likely that this sulfur trioxide reacts with adventitious water found in solution due to the presence of H_2O_2 as the oxidant as well as the stoichiometric equivalency of water formed upon O–O bond cleavage to form sulfate. Additionally, a series of Fe^{III}-phenolate species is observed as the formed product, supporting the proposed mechanism. These phenolate products with a variety of *para*-substitutions give rise to nearly identical vibrational spectra to the related product generated from Fe^{II} and the corresponding *para*-substituted phenols in the presence of air (Figure 11).

It is also possible that the formation of the Fe^{III}-phenolate species proceeds through an electron transfer mechanism (Figure 13**b**). While the formation of the $Fe^{III}(OOH)$ species and subsequent heterolytic O–O bond scission are likely still the first mechanistic steps, the following steps may proceed through an electron transfer-type mechanism. The highly oxidizing iron center may oxidize the sulfonate, followed by the homolytic cleavage of the aromatic C–S bond, resulting in an aryl radical species and a

sulfite ion. A similar electron transfer has been observed in nature, where the sulfur acts as an electron donor in a few desulfonation transformations.[114, 115] This newly-formed aryl-centered radical can then reduce the iron center to Fe^{III} and form an aryl C–O bond, giving rise to the Fe^{III}-phenolate species observed and characterized. Irrespective of the mechanism, to the best of our knowledge, these examples represent the first time that this combination of desulfonation and hydroxylation transformation has been demonstrated in the literature of synthetic non-heme complexes.

There are very few articles that detail oxidative transformations similar to the desulfonation reaction presented here. The observed hydroxylation of the C–S bond in the present work may be the most similar to the intramolecular C–F bond hydroxylation first reported by Goldberg and coworkers in 2014 and furthered investigated in 2016, as it involves the breaking of a non-C–H bond on an arene ring.[54, 116] This reaction also features an oxoiron(IV) complex, but it is ligated by a N4Py-derived ligand framework $N4Py^{2Ar1}$ (N4Py = *N,N*-bis(2-pyridyl)-*N*-bis(2-pyridyl)methylamine; Ar_1=−2,6-difluorophenyl) performing an intramolecular self-hydroxylation to form an iron(III)-phenolate. Similar to our proposed mechanism **a**, a high-valent iron-oxo oxidant is proposed to perform an electrophilic attack on the pendant arene ring. This mechanistic pathway was investigated by introducing electron-donating methoxy groups *ortho*/*para* to the C–F bond. With these substitutions, the rate of self-hydroxylation was reported to increase (>100-fold). In contrast, when a methoxy group was substituted *meta* to the C–F bond, very little increase in rate was observed, further supporting an electrophilic

substitution pathway. These observations parallel very closely those associated with the substituted benzenesulfonic acids employed in this work, where the *p*-substitutions Me, Cl and H facilitate the formation of the final product phenolate (Figure 13). It is arguable that both the Me and Cl substituents are *ortho/para* directing, due to increasing the electron density in the aromatic ring. This series of observations are consistent with an electrophilic aromatic substitution pathway, as the Wheland-type intermediate is stabilized through resonance delocalization and further supports our proposed mechanism. Importantly, the authors argue that substrate orientation is among one of the most important factors in the C–F bond hydroxylation mechanism and that the second-sphere coordination is what allows for this difficult oxidation to be carried out. This explanation along with the intramolecular hydroxylations observed in iron[4, 75] as well as cobalt[117] complexes raise the possibility that the conjugate base of the benzenesulfonic acid interacts with the iron center, which would allow the benzenesulfonate to be oriented more appropriately for hydroxylation. Further investigation is necessary to support this proposed interaction.

2.6 — Summary, Conclusions, and Broader Implications

It has been observed that the polypodal ligand framework MeTPEN is competent towards forming an iron(III)-hydroperoxo species which, upon addition of a sufficiently strong Brønsted acid, undergoes heterolytic O–O bond cleavage to generate a high-valent iron-oxo complex. This complex is capable of oxidizing benzene, resulting in the formation of an Fe^{III}-phenolate complex. Notably, when a series of benzenesulfonic acids is

employed as additives, the corresponding series of new products is observed and characterized. These products are best described as Fe^{III}-phenolate complexes, as demonstrated by UV-Vis and resonance Raman spectroscopic analyses. A thorough investigation has been carried out on two benzenesulfonic acid derivatives, namely 4-methylbenzenesulfonic acid and 4-chlorobenzenesulfonic acid. It is hypothesized that protonation of the distal oxygen atom of the peroxo unit of the $Fe^{III}(OOH)$ moiety and subsequent heterolysis of its O–O bond generating an oxidant that most likely performs electrophilic aromatic substitution (Figure 13**a**), undergoing desulfonation of the conjugate base benzenesulfonate and forming an Fe^{III}-phenolate product. These Fe^{III}-phenolate products that have been formed upon desulfonation and hydroxylation are shown to be spectroscopically consistent with phenolate products formed upon the reaction of substituted phenols with the iron(II) complex in the presence of air. When these substituted Fe^{III}-phenolate products formed through the two different pathways laid out herein are compared spectroscopically, the similarities (Table 2, Figure 11) have led to the initial conclusion that oxidative desulfonation occurs and are further supported by a series of substituted benzenesulfonic acids. Notably, the introduction of strong electron withdrawing substituents results in no formation of the final phenolate product, thereby supporting the hypothesis that an electrophilic aromatic substitution is promoted by the presence of a resonance-stabilized carbocation intermediate on the arene ring. Taken together, these results conclusively demonstrate that oxidative desulfonation

indeed occurs and that it is most likely through an electrophilic aromatic substitution whereby the electrophile is the high-valent iron-oxo complex.

This work has broad-reaching implications, touching on several transformations observed in the natural world such as the *ipso*-hydroxlyation observed in sulfonamide-metabolizing microbes.[114] It has been further demonstrated that protons indeed play an important role in perturbing the O–O bond cleavage of iron(III)-hydroperoxo species found in synthetic systems, illustrating the importance of proton donors in nature. This facilitation of the cleavage of the O–O bond is integral for the unleashing of a high-valent iron-oxo species that is competent in performing several oxidizing transformations. This reactivity can be found in both heme systems in the formation of Cpd I[118] and in non-heme systems such as the formation of the powerful oxidant sMMO-**Q** in the conversion of methane to methanol performed by methane monooxygenase.[119, 120] Additionally, aromatic hydroxylation is an important transformation that has been observed in a variety of non-heme hydroxylases, such as PheH, TyrH, and TrpH. This work demonstrates that these powerful metal-based oxidants are competent towards performing intermolecular aromatic hydroxylation on a variety of substrates but that the electronics of the substrate are important in end-product formation, as observed in our work involving electron-withdrawing substitutions on the substrates.

Sulfonamide antibiotics such as SMX (sulfamethoxazole), SDZ (sulfadiazine), and SML (sulfanilamide) accounted for nearly 11% of total veterinarian pharmaceutical sales in 25 European countries in 2011.[121] However, only a small percentage of sulfonamide

antibiotics are absorbed by the body with excess primarily being excreted through urine, feces, and even sweat.[122] These sulfonamide compounds persist into the environment and are one of the most widely and frequently detected pollutants in the environment, being found in the highest concentrations in livestock and hospital wastewater, groundwater, and manure, with detectable levels as high as 18 mg/kg contamination in manure and 1340 μg/L in pharmaceutical wastewater.[123] These high sulfonamide concentrations are well beyond the estimated 16 μg/L no-effect concentration for SMX-resistance[124] which can exert selective pressure on resistant pathogens, thereby threatening therapeutic effectiveness of these incredibly common antibiotics.[125] There is an increasing concern about the biomagnification and environmental presence of these antibiotics and efforts have been made to use bacteria to assist in the degradation of these pollutants.[126, 127] There are few microbes that have been found competent to metabolize these sulfonamides[128] and sulfonates,[129] some even using these substrates as their only carbon, nitrogen, energy, and even sulfur sources. Of these select few microbes, only very few active sites have been characterized. *Microbacterium* sp. strain BR1 has been found to be a flavin-dependent monooxygenase that degrades various sulfonamides.[126] A Rieske dioxygenase has been implicated as an important oxidant in the microbe *Methylosulfonomonas methylovora*.[130, 131] In other bacteria such as *Acinetobacter* sp. W1, the metabolite 4-hydroxybenzenesulfonic acid was observed along the degradation pathway of various sulfonamides. The authors suggest that a NADH-dependent hydroxylation similar to that observed in *Microbacteriums* sp. strain BR1 may

be responsible for the degradation pathway, but the mechanism is still unknown.[132] In another effort, three bacteria have been isolated and identified: *Labrys* sp. SMX-W1-SC11 (SC11), *Gordonia* sp. SMX-W2-SCD14 (SCD14), and *Ochrobactrum* sp. SMX-PM1-SA1 (SA1), all of which metabolize sulfonamides where 4-aminophenol was identified as an intermediate metabolite.[133] The authors propose an *ipso*-hydroxylation at the carbon geminal to the sulfonamide, although little experimental evidence supports this claim. Interestingly, in SC11 and SCD14, hydroquinone was detected downstream from 4-aminophenol and subsequently gave products consistent with a hydroquinone dioxygenase, demonstrating that iron-based active sites are likely present within these bacteria as non-heme iron enzymes have been found competent to perform this oxidative transformation.[134] Our results are the first indication, to the best of our knowledge, that an iron-incorporating active site may be responsible for the metabolism of these sulfonamides such as SMX in a variety of bacteria where metabolites such as 4-aminophenol have been identified, the *ipso*-hydroxylated product of SMX. Additionally, our work may guide future investigations of the mechanism as to how these bacteria that metabolize sulfonamide- and sulfonate-containing substrate proceed.

2.6.1 — Additional Figures

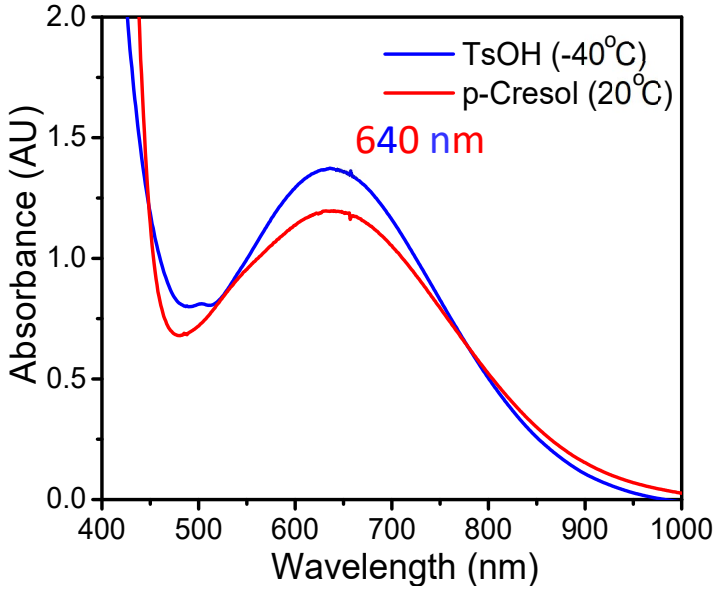

Figure 14. Spectral comparison of a) **2** upon the addition of TsOH at -40 °C (blue) and b) Fe^{II} starting material upon the addition of *p*-cresol in the presence of air at 20 °C. Both spectra were obtained in CH_3CN. [Fe] = 3 mM

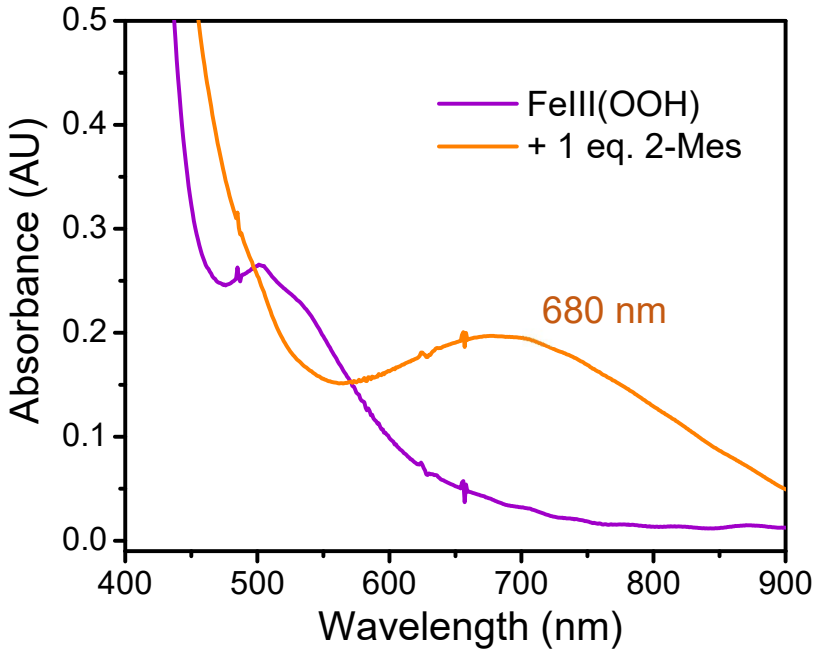

Figure 15. UV-Vis spectrum associated with the addition of 1 equiv 2-mesitylenesulfonic acid (2-Mes) to a solution of intermediate **2** in CH_3CN at 1 mM Fe^{II} complex concentration.

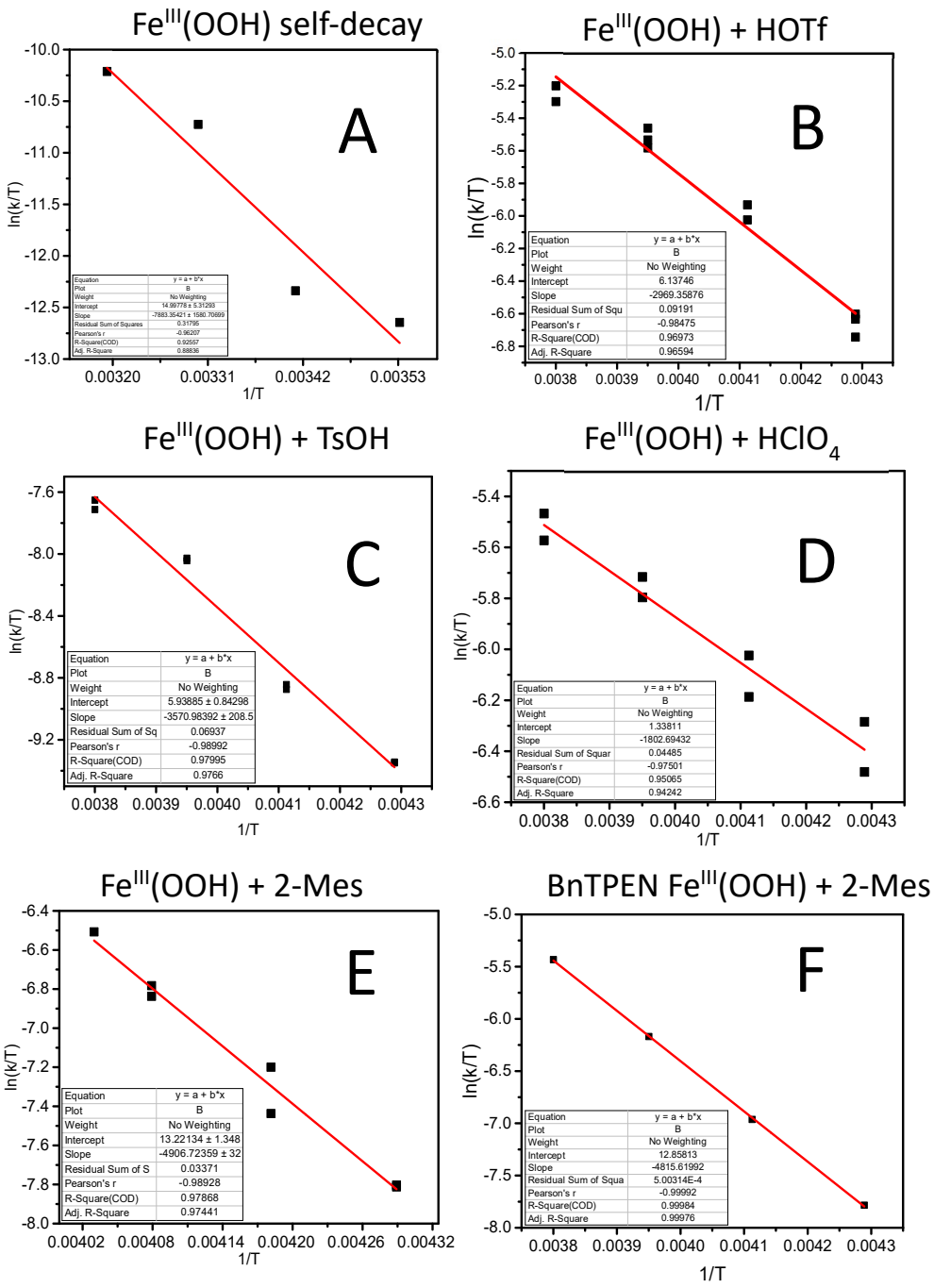

Figure 16. Eyring plots for **2** decay under different conditions. A: with only HOAc; B: with HOAc and 0.5 equiv HOTf; C: with HOAc and 1.0 TsOH; D: with HOAc and 0.5 equiv $HClO_4$; E: with HOAc and 1.0 equiv 2-Mes; F: with HOAc and 1.0 equiv 2-Mes. Reaction conditions A-E: 1 mM **1**/10 equiv HOAc/10 equiv 90% H_2O_2/with or without acid in CH_3CN; reaction condition F: 1 mM $[(Fe^{II}(CH_3CN)(BnTPEN)]^{2+}$ /10 equiv HOAc/10 equiv 90% H_2O_2/0.5 equiv 2-Mes in CH_3CN. Values are listed in Table 3.

Chapter 3: Structural Investigation of a Pathway to Form a High-Spin Bimetallic sMMOH-Q Mimic

3.1 — Introduction

High-valent iron species have been found to be powerful oxidants in both nature as well as in synthetic systems.[9] In enzymatic systems, diiron enzymes such as soluble methane monooxygenase (sMMOH), ribonucleotide reductase (RNR), human deoxyhypusine hydroxylase (hDOHH), and others natively perform powerful oxidative transformations such as the oxidation of methane to methanol and the conversion of ribonucleotides to deoxyribonucleotides.[21, 25, 135, 136] A generalized pathway for these oxygenase enzymes is initialized by the binding of O_2 to the iron active site to form a peroxodiferric species that is then converted to a high-valent diiron complex that is typically proposed as the powerful oxidizing species.

A closer look at the mechanistic cycle of sMMOH shows the involvement of two high-valent intermediates of interest. Upon reduction of both iron centers to iron(II), the active site then binds dioxygen to form a peroxodiferric intermediate **P**, which has been proposed to have a μ-1,2-peroxo unit bridging two ferric centers. These classes of diferric cores are of great interest to the field because upon the activation of the peroxo unit, a putative diferryl closed core species $Fe^{IV}_2(\mu\text{-}O)_2$ (**Q**) is proposed to form. Importantly, both iron centers have been found to be high-spin $S = 2$. There is currently a dispute in the bioinorganic field as to whether or not **Q** is the species that performs the oxidation of methane to methanol or the closed-core opens to a terminal oxoiron species (open core) that is then responsible for the oxidation of methane.[22, 29] High-spin synthetic mimics may be vital in providing key spectroscopic information to help support either the closed or

open core assignments. Additionally, enforcing high-spin iron centers in bimetallic systems may be important in performing difficult oxidative transformations yet to be performed by synthetic diiron complexes.

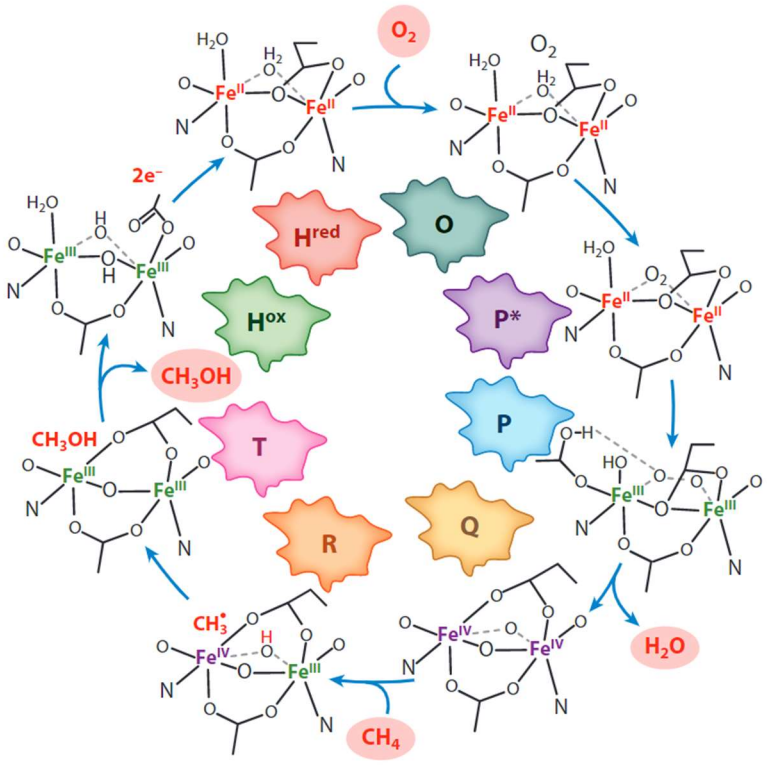

Figure 17. Proposed catalytic cycle of the oxidation of methane to methanol performed by soluble methane monooxygenase. Adapted from Ref [21] with permission.

An interesting ligand is TQA, an abbreviation for tris(quinolinyl-2-methyl)amine. The ligand is a tripodal ligand which coordinates through its four nitrogen atoms to the iron center. What makes TQA of special interest is the high-valent monoiron complex $[Fe^{IV}(O)(TQA)(CH_3CN)]^{2+}$ that forms and is found to be highly reactive towards C–H bond cleavage. This complex has been characterized by Mössbauer spectroscopy to have an *S*

= 2 spin state,[39] which makes it a bioinspired functional mimic of the iron active site found in monometallic enzymes such as TauD where a high-spin $Fe^{IV}(O)$ intermediate, namely TauD-***J***, is responsible for the H-atom abstraction of taurine in a biological pathway.[137] However, to this date, the corresponding synthetic dimeric $Fe^{IV}_2(\mu\text{-}O)_2$ center with $S = 2$ iron centers has yet to be synthesized to serve as a mimic for the oxidant that is formed in the active site of sMMOH-**Q** and is responsible for the hydroxylation of methane in methanotrophic bacteria.

There have been previous synthetic efforts to form diferryl diamond core species. An electron-rich tripodal ligand TPA* (Figure 22) had been employed and found competent to support the formation of $[Fe^{IV}_2(O)_2(TPA^*)]^{2+}$.[92] However, Mössbauer spectroscopy supported the assignment of both iron(IV) centers having $S = 1$ spin states.[92] This is consistent with the observation that the monoiron(IV) complex $[Fe^{IV}(O)(TPA^*)(MeCN)]^{2+}$ has an $S = 1$ spin state and is approximately 100-fold faster at oxidizing weak C—H bonds than the diferryl partner.[86] With TQA being a tetradentate ligand, therefore having 2 open coordination sites in a *cis* conformation, this may allow for the formation of a bimetallic complex. Because the $[Fe^{IV}(O)(TQA)(MeCN)]^{2+}$ was found to be $S = 2$,[39] the TQA ligand may promote two high-spin iron(IV) centers if a $[Fe^{IV}_2(O)_2(TQA)]^{2+}$ complex could be generated.

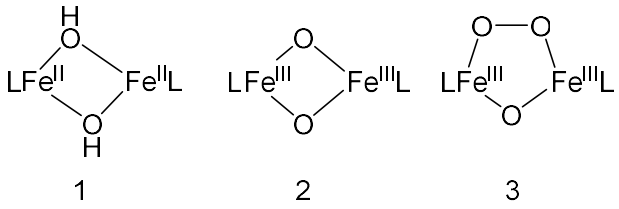

Figure 18. Cartoon depictions of the structures explored in this study. Ligand has been removed for simplicity. L = TQA

3.2 — Pathway for Formation of Complexes

In parallel with the enzymatic systems, a diferrous starting complex ligated by TQA has been formed and characterized, namely $[Fe^{II}_2(\mu\text{-}OH)_2(TQA)_2]^{2+}$ (**1**). This species was generated and characterized spectroscopically by UV-Vis spectroscopy (λ_{max} = 504 nm, ε = 2000 M^{-1} cm^{-1}). Upon exposure to molecular oxygen, **1** forms a new species that has been postulated as being a $[Fe^{III}_2(\mu\text{-}O)_2(TQA)_2]^{2+}$ (**2**), a diferric diamond core species. **2** has been characterized spectroscopically initially with a relatively featureless UV-Vis spectrum with a small shoulder feature at 400 nm. Upon the addition of H_2O_2 to complex **2**, an intermediate with spectroscopic properties that resemble a $[Fe^{III}_2(\mu\text{-}O)(\mu\text{-}O_2)(TQA)_2]^{2+}$ (**3**) has been observed and characterized structurally (λ_{max} = 640 nm, ε = 900 M^{-1} cm^{-1}). Complex **3** is comparable with the intermediate **P** in the sMMOH mechanistic cycle as these species are both proposed to have a diferric core bridged by a peroxo unit. Similar to **P**, it may be possible to active the O—O bond in this species and unleash a diferryl intermediate that may be competent towards methane oxidation. The lifetime of intermediate **Q** is very fleeting, requiring rapid-freeze quenching.[21] If the O—O bond in

complex **3** can be activated to form a **Q**-like intermediate, this new intermediate may provide important insight into the speciation of **Q**.

3.2.1 — XANES Analysis

X-ray absorption near edge structure analysis has been utilized to gain insight into the closed core structures of **1**, **2**, and **3**. The XANES analysis allows for exploration of both oxidation state and centrosymmetry for the metal center. The K-rising edge is a result of the excitation of a 1s electron to a 4p orbital of the metal center. As the oxidation state of the metal center increases, it requires more energy to excite this 1s electron, therefore blue-shifting the rising edge. It is important to consider that the ligand composition as well as the spin-state of the metal center can contribute to a shift in the rising edge without a change in oxidation state and therefore may need to be accounted for when comparing samples. The pre-edge feature grants insight into the centrosymmetry of the metal center. This is due to the pre-edge absorption that arises from the Fe 1s → 3d excitation which is formally quadrupole-allowed dipole-forbidden. The intensity of this feature is proportional to the mixing of the 3d and 4p orbitals which increases upon deviation from centrosymmetry.

The K-edge energy for complex **1** is 7121.8 eV. Upon a 1-electron oxidation of the iron center, the K-edge energy is shifted by approximately 1 eV to 7123.0 eV for complex **2**, consistent with an increase in the oxidation state of the metal center. Complex **1** is the only diferrous diamond core diiron complex thus far characterized by XANES. Two pre-

edge features have been found at 7112.5 and 7114.2 eV, both contributing about 50% of the total pre-edge area. Notably, the pre-edge area of **1** has been found to be quite low at 6.6, reflecting that the relatively high symmetry of the iron(II) centers. In contrast, **2** has a significantly higher pre-edge area of 16.2 units with only one feature centered at 7114.6 eV. This is reflective of a deviation from centrosymmetry upon the formation of the second short iron-oxygen bond in the proposed diferric bis-μ-oxo complex. Only one other member of this family of complexes has been characterized, namely the $[Fe^{III}_2(\mu\text{-}O)_2(6Me_3TPA)_2]^{2+}$ complex.[138] Despite the fact that this $6Me_3TPA$-ligated complex has been characterized with XAS, no XANES analysis was reported for this complex. Therefore, complexes **1** and **2** are the only complexes with an $Fe^{II}_2(\mu\text{-}OH)_2$ or an $Fe^{III}_2(\mu\text{-}O)_2$ core with XANES data available.

Table 4. Comparison of XANES data for the complexes in this work.

Complex	K-edge (eV)	peak position (eV)	component area	pre-edge area (units)
$[Fe^{II}_2(\mu\text{-}OH)_2(TQA)_2]^{2+}$ **1**	7121.8	7114.2 7112.5	3.48 (53%) 3.10 (47%)	6.58
$[Fe^{III}_2(\mu\text{-}O)_2(TQA)_2]^{2+}$ **2**	7123.0	7114.6	16.22 (100%)	16.22
$[Fe^{III}_2(\mu\text{-}O)(\mu\text{-}1,2\text{-}O_2)(TQA)_2]^{2+}$ **3**	7122.7	7114.8	19.07 (100%)	19.07

While there are no diferrous or diferric XANES data available for these closed core complexes, there are data available for higher valent complexes. As previously discussed, TPA* has been well-studied as a ligand that can support high-valent core species. Similar to the pre-edge area found for complex **2** of 16.2, the $Fe^{III,IV}_2(\mu\text{-}O)_2$ and $Fe^{IV,IV}_2(\mu\text{-}O)_2$ species were found to have approximately pre-edge area of 19 units. These are quite similar to each other when compared to the value found for complex **1**. This indicates that the symmetry around the iron centers is more similar between the diferric core when compared to the mixed valent complex and the diferryl diamond core species. It is found that the higher-valent cores feature 2 shorter Fe—O bonds around 1.8 Å and 4 longer Fe—N bonds around 2.0 Å (Table 8). Therefore, we hypothesize to find a diferric core for 2 that is similar in structure to the higher-valent complexes. This hypothesis is consistent with what we found in structural analysis discussed later in this chapter.

Table 5. Comparison of XANES data for diiron diamond core complexes.

Core Structure	ligand	K-edge (eV)	peak position (eV)	component area	pre-edge area (units)	ref
$Fe^{II}_2(\mu\text{-}OH)_2$	TQA	7121.8	7114.2	3.5	6.6	t.w.
			7112.5	3.1		
$Fe^{III}_2(\mu\text{-}O)_2$	TQA	7123.0	7114.6	16.2	16.2	t.w.
$Fe^{III,IV}_2(\mu\text{-}O)_2$	TPA*	7129.0	7113.2	14.7	19.7	[92]
			7115.7	5.0		
$Fe^{IV,IV}_2(\mu\text{-}O)_2$	TPA*	7130.1	7114.7	13.8	19	[92]
			7117.9	5.2		
$Fe^{IV,IV}_2(\mu\text{-}O)_2$	Me_3NTB	7127.5	7113.9	5.8	18.2	[30]
			7114.9	3.2		
			7115.0	9.2		

t.w. – this work

3.2.2 — EXAFS Analysis

In the absence of diffraction quality crystals, significant structural insight can often be obtained from extended X-ray absorption fine structure (EXAFS), shedding light on metal-ligand distances in any metal complex as well as the metal-metal distance in a bimetallic complex. A single EXAFS fit may contain information regarding several atoms around the metal center. These atoms can be described broadly as being in different “shells”, where the closest atoms may be referred to as being in the first shell, the next sphere of atoms being in the second shell, and so on and so forth. We can describe these shells with a few different parameters: N, R, and σ. N refers to the coordination number, providing information with respect to the number of atoms contained within said shell.

Additionally, the R variable is referred to as the radius or distance of the shell from the central atom, usually reported in units of Ångstrom. This can be interpreted as bond distances for shorter interactions or through-space distances for longer interactions. Lastly, the σ is the Debye-Waller factor which is a representation of the thermal displacement in neighboring atoms and can be thought of as a measurement of disorder. Importantly, this value must always be above 0 $Å^2$ and ideally below ~ 5 $Å^2$ but can be higher in certain circumstances. In order to compare the quality of a fit against one-another, the Goodness-of-Fit (GOF) variable F is, broadly speaking, typically minimized as the quality of fit improves. For example, as shown in Table 6, as the number of shells is increased from Fits 1 to 4, the F value decreases, indicating that the quality of the fit is improving upon the addition of more shells.

To explore the connectivity around the metal centers in **1**, EXAFS data has been collected and fit (Table 6). It has been found that the best fit 4 contains 4 shells, being: 1 Fe—N/O at 1.99 Å, assigned to a shorter Fe—OH bond; 5 Fe—N/O at 2.24 Å, assigned to 4 Fe—N ligand bonds and 1 longer Fe—OH bond; 1 Fe·····Fe at 3.17 Å; and lastly 6 Fe·····C at 3.03 Å. A limitation of EXAFS fitting is that one cannot reliably distinguish between two atoms of similar atomic size. The nitrogen and oxygen bond assignments were made based on comparisons with crystallographic data obtained for other $[Fe^{II}_2(\mu\text{-}OH)_2(L)_2]^{2+}$ complexes in Table 8. Notably, the two Fe—OH bond distances are quite different, differing by about 0.15 Å. This is reflected in the EXAFS fit, with only N = 1 found for the shorter iron-hydroxo bond. The second iron-hydroxo bond cannot be distinguished from

the ligand bonds, thereby being fit into the second shell. While an Fe—OH bond distance of 2.24 Å is about 0.14 - 0.06 Å longer than other reported values, this observation can be rationalized by the following argument. If we consider a weighted average where there is 4 Fe—N bonds at approximately 2.25 Å, consistent with the crystallographically reported complexes, and 1 Fe—O bond at 2.14 Å, 0.15 Å longer than the 1.99 Å found for the first shell, we find an average iron-atom bond of 2.23 Å, nearly identical to the R value of 2.24 Å obtained. Additionally, the iron-iron distance of 3.17 Å requires a second ligand bridging the two iron centers, as linear complexes feature significantly longer iron-iron distances closer to 3.5-3.7 Å.[9] Therefore, the assignment of 1 shell consisting of a short Fe—OH bond at 1.98 Å, a second shell of N = 5 atoms consisting of a longer Fe—OH bond and four Fe—N ligands at 2.24 Å is reasonable.

Due to the iron atom's relatively large atomic number when compared to those of oxygen, nitrogen, and carbon, a second iron atom can be distinguished readily in EXAFS fits, allowing for strong support of diiron core structures. Fit 4 contains an iron scatterer at a distance of 3.17 Å, consistent with other iron-iron distances found in similar complexes. Lastly, a carbon shell was found at 3.03 Å, typical for nitrogen-containing heterocyclic ligands. Taken together, our fit support the assignment of a $Fe^{II}_2(\mu\text{-}OH)_2$ core structure with 4 ligating nitrogen atoms.

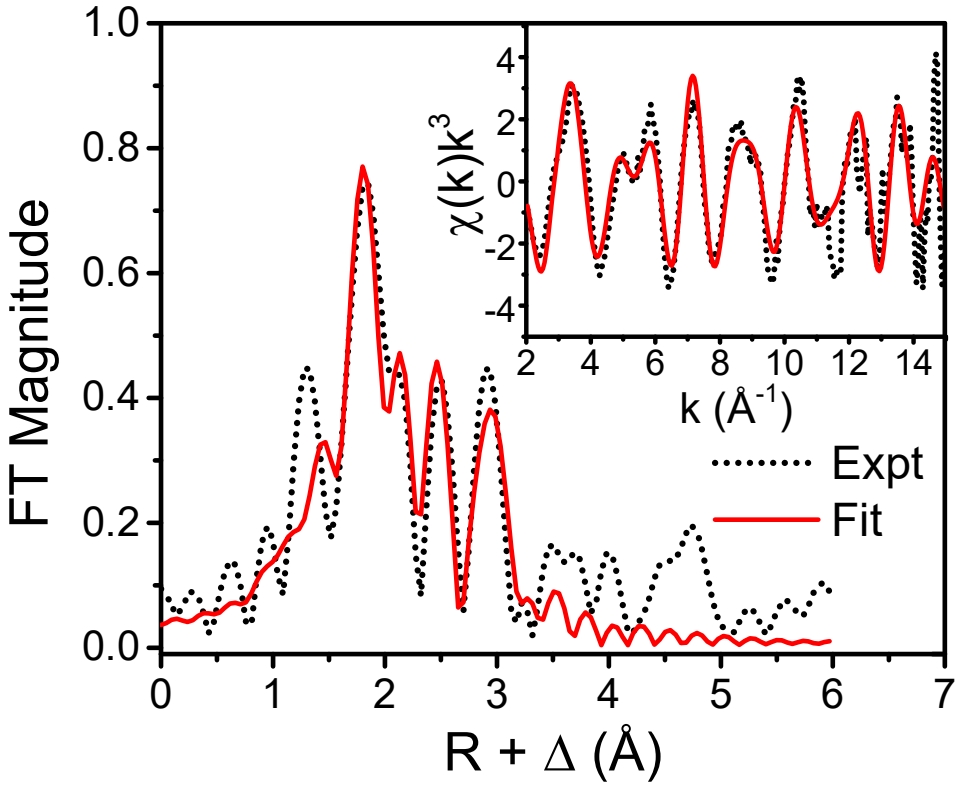

Figure 19. Fourier transformed EXAFS spectrum and the *k*-space data (inset) for $[Fe^{II}_2(\mu\text{-}OH)_2(TQA)_2]^{2+}$ (Fit 4).

Table 6. EXAFS fits for $[Fe^{II}_2(\mu\text{-}OH)_2(TQA)_2]^{2+}$ (1). Best fit in bold.

	Fe-N/O			Fe·····Fe			Fe·····C				GOF	
Fit	N	R (Å)	σ^2	N	R (Å)	σ^2	N	R (Å)	σ^2	E_0	F	F'
1	1	2.25	-0.10							-1.66	760	546
2	1	2.00	5.11							-3.37	646	544
	5	2.25	4.49									
3	1	1.99	5.25	1	3.17	5.84				-2.06	596	542

	5	2.25	4.55									
4	**1**	**1.99**	**4.06**	**1**	**3.17**	**1.16**	**6**	**3.03**	**1.95**	**-5.07**	**496**	**540**
	5	**2.24**	**4.78**									

k range = 2-15 $Å^{-1}$, resolution = 0.121 Å, σ^2 = mean-squared deviation in units of 10^{-3} $Å^2$. Scale Factor S_0^2 = 0.9. Goodness-of-fit (GOF) = F calculated as $F = \sqrt{\sum k^6(\chi_{exp} - \chi_{calc})^2}$. $F' = \sqrt{\sum k^6(\chi_{exp} - \chi_{calc})^2 / \sum k^6 \chi_{exp}{}^2}$.

In conjunction with complex **1**, the diferric diamond core species $[Fe^{III}_2(\mu\text{-}O)_2(TQA)_2]^{2+}$ has been explored structurally through EXAFS. Complex **2** is best fit by 4 shells with 2 short Fe—N/O distances at 1.87 Å, assigned to the short Fe^{III}—O bonds; 4 longer Fe—N/O distances at 2.23 Å, corresponding to the TQA ligand; a notably short Fe·····Fe at 2.65 Å; and a carbon shell at 2.99 Å, similar to what was found for **1**. The EXAFS Fourier transform shows a large second feature between 2 and 3 Å of equivalent intensity to the combined Fe—N/O between 1.5 and 2 Å. This is strong evidence for the short iron-iron distance as the rigidity of this tightly held core combined with short iron-iron distance is what gives rise to this noticeably large feature in the Fourier transform (Figure 20). When compared to the Fourier transform of complex **1**, the feature that contains the iron is much less intense due to the longer distance between the two iron centers as well as the likely more flexible core due to the longer and weaker Fe—O bonds (Figure 19). To help determine the structure of the diamond core, the short iron-iron distance helps

assign the bridging atoms as bis-μ-O instead of a possible μ-O, μ-OH connectivity like the reported $[Fe^{III}_2(\mu\text{-}O)(\mu\text{-}OH)(L)_2]^{2+}$, which has an average iron-iron distance of about 2.9 Å, ~0.2 Å longer than the iron-iron distance found in Fit 4 for complex **2**. Additionally, one would expect two distinguishable Fe—O scatterers, as was reported for $[Fe^{III}_2(\mu\text{-}O)(\mu\text{-}OH)(6Me_3TPA)_2]^{2+}$.[138] Another possibility is that, if the two Fe—O scatterers were within the resolution limit (~0.12 Å) and therefore indistinguishable by EXAFS, a longer shell would still be expected, closer to 1.92 Å, which is 0.05 Å longer than what has been found. Taken all together, our assignment of $[Fe^{III}_2(\mu\text{-}O)_2(TQA)_2]^{2+}$ agrees well with the XAS data obtained and helps support our assignment of the second diferric diamond core structure.

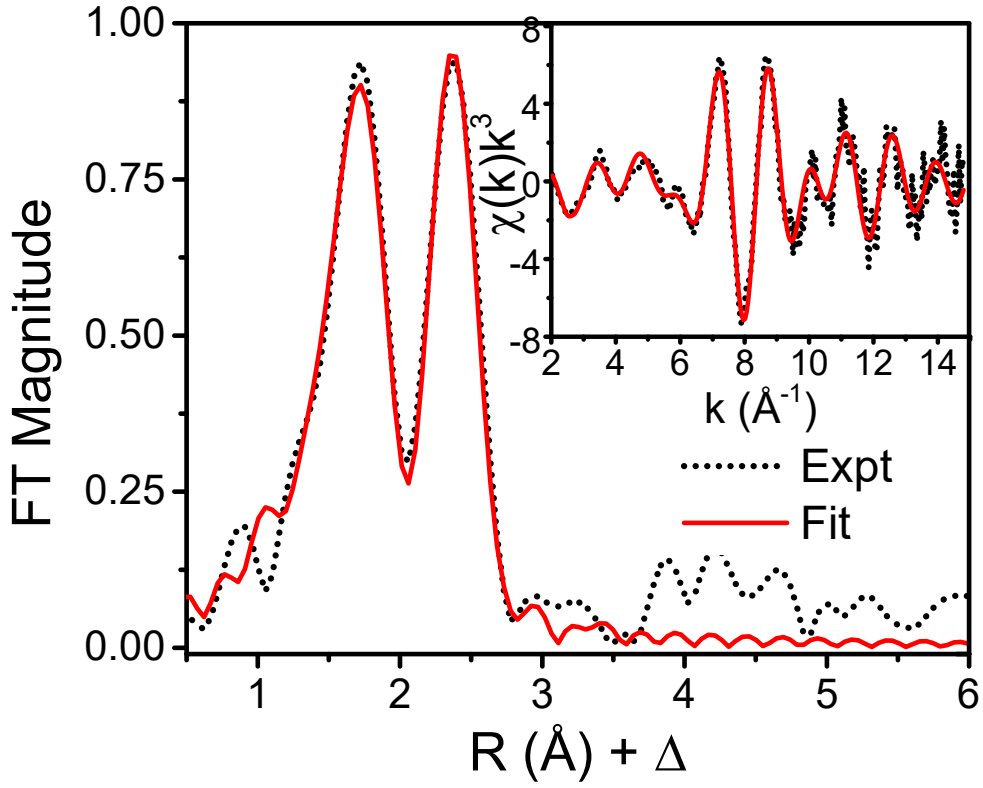

Figure 20. Fourier transformed EXAFS spectrum and the k-space data (inset) for $[Fe^{III}_2(\mu\text{-}O)_2(TQA)_2]^{2+}$ (Fit 4).

Table 7. EXAFS fits for $[Fe^{III}_2(\mu\text{-}O)_2(TQA)_2]^{2+}$ (**2**). Best fit in bold.

	Fe-N/O			Fe·····Fe			Fe·····C				GOF	
Fit	N	R (Å)	σ^2	N	R (Å)	σ^2	N	R (Å)	σ^2	E_0	F	F'
1	2	1.85	4.04							-7.68	926	418
2	2	1.88	3.66							-0.81	703	416
	4	2.24	5.26									
3	2	1.88	3.28	1	2.67	1.99				1.78	371	415
	4	2.25	5.57									
4	**2**	**1.87**	**3.58**	**1**	**2.65**	**2.22**	**4**	**2.99**	**4.5**	**-3.80**	**333**	**413**
	4	**2.23**	**5.03**									

k range = 2-15 $Å^{-1}$, resolution = 0.121 Å, σ^2 = mean-squared deviation in units of 10^{-3} $Å^2$. Scale Factor S_0^2 = 0.9. Goodness-of-fit (GOF) = F calculated as $F = \sqrt{\sum k^6\left(\chi_{exp} - \chi_{calc}\right)^2}$. $F' = \sqrt{\sum k^6\left(\chi_{exp} - \chi_{calc}\right)^2 / \sum k^6 {\chi_{exp}}^2}$.

Complex **2** has also been recently characterized through single crystal X-ray diffraction (Figure 21).[139] The X-ray diffraction bond metrics agree very well with the EXAFS fitting results. The short Fe—O scatterer found in EXAFS at 1.87 Å is an average of the two Fe—O bonds found in the crystal structure (1.839, 1.917 Å). Additionally, both the average ligand bond distances and iron-iron distance agree very well between the EXAFS and X-ray crystal structure, differing by only 0.02 Å and 0.01 Å, respectively.

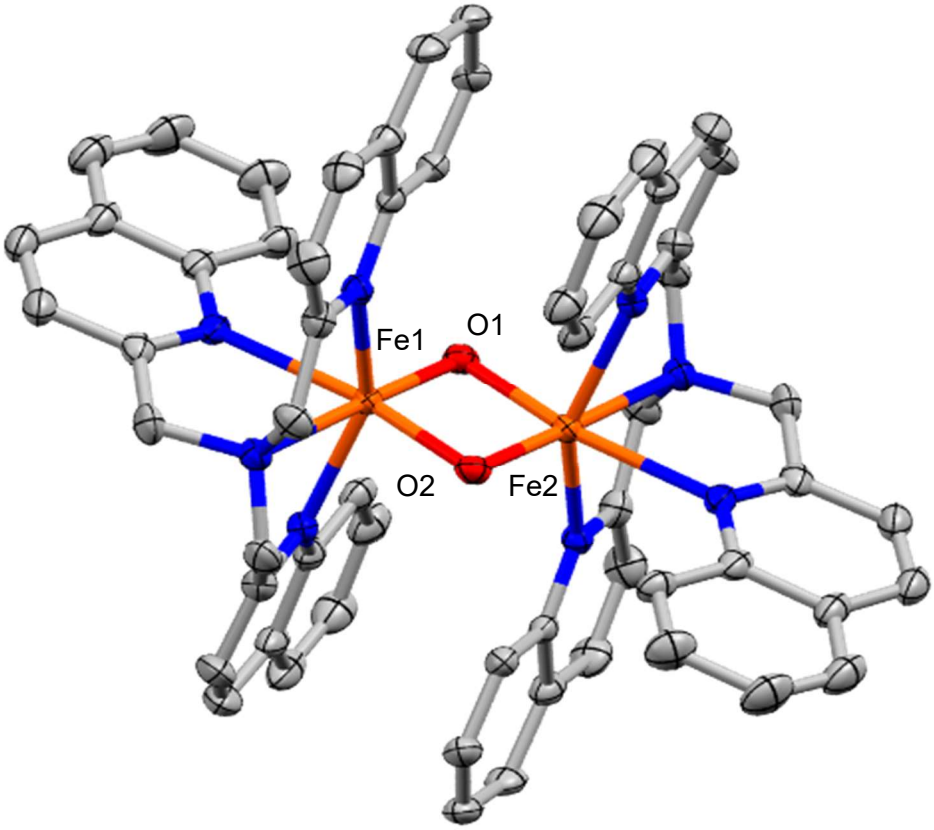

Figure 21. Single crystal X-ray diffraction for $[Fe^{III}_2(\mu\text{-}O)_2(TQA)_2]^{2+}$ (**2**) drawn at 50 % probability with H-atoms, solvent, and counteranionic $^{-}$OTf omitted for clarity. Color scheme: Fe, orange; O, red; N, blue; C, gray. Selected bond lengths (Å): Fe1—O1, 1.839(3); Fe1—O2, 1.917(3); Fe—N_{ave}, 2.255(13); Fe1·····Fe2, 2.6679(8). Data available from Ref [139].

There are many similarities between the TQA- and $6Me_3TPA$-ligated complexes. Firstly, the ligand structures are quite similar to one another. It is reported that 6-position substitutions on pyridines weaken the ligand field by imposing a steric influence between the 6-position and the iron center.[140] The same has also been hypothesized for TQA, supporting an argument that the benzene ring appended to the pyridine moiety of the quinoline can be thought of as a 6-substituent on the pyridine heterocycle.[39] When

comparing the bond metrics for the $[Fe^{II}_2(\mu\text{-}OH)_2(L)_2]^{2+}$ (L = $6Me_3TPA$, TQA) with other diferrous complexes, the most notable difference can be observed in the iron-iron distances. The most sterically hindered ligands lengthen the iron-iron distance by about 0.1 Å. The ligand BnBQA can be thought of as an intermediary between $6Me_3TPA$/TQA and TPA. BnBQA is a bipodal ligand with a central amine and two quinolines compared to $6Me_3TPA$/TQA being tripodal ligands with a central amine and three 6-substituted heterocycles. Therefore, one would expect the BnBQA to be less sterically hindered than TQA but more hindering than TPA. This is reflected in the iron-iron distance in the $[Fe^{II}_2(\mu\text{-}OH)_2(L)_2]^{2+}$ structures, where the least sterically hindered ligand TPA has an iron-iron distance of 3.048 Å (average between two structures), the next sterically hindered BnBQA has a distance of 3.135 Å, and the most sterically hindered TQA and $6Me_3TPA$ have iron-iron distances of 3.17 Å and 3.194 Å (average among three structures). There is a noticeable increase in iron-iron distance as quinolines or 6-position pyridine substitutions are introduced into the ligand framework.

The ligand-field weakening of the 6-position pyridine substitutions may be responsible for the unique diferric intermediates that can be trapped and characterized for the $6Me_3TPA$ and TQA complexes when compared to less sterically hindered ligands like TPA. As is shown in Table 8, there are several examples of protonated diamond core structures, but only $6Me_3TPA$ and TQA have been found to support a bis-μ-O structure. As stated previously, the EXAFS and X-ray diffraction data for $[Fe^{III}_2(\mu\text{-}O)_2(TQA)_2]^{2+}$ agree very well, and the same is true for the EXAFS and X-ray diffraction data for the $6Me_3TPA$

analog. Additionally, the TQA- and $6Me_3$TPA-ligated complex data are also incredibly similar to one another, further cementing the similarities between the ligand frameworks and illustrating the steric influence of 6-position substitutions on pyridine ligands.

Importantly, the mononuclear TQA oxoiron(IV) complex is high-spin (S = 2), which makes TQA a good biomimetic ligand for enzymatic non-heme oxoiron(IV) complexes, which are also high-spin.[9, 39] It is postulated that the quinolines impose a steric hinderance, weakening the ligand field and reducing the energy of the S = 2 state.[39, 140] A shortcoming of the diiron(IV,IV) complexes that have been studied thus far is that these complexes are found to have low-spin S = 1 iron centers. This is different from the spin states reported for sMMOH-**Q**, a highly reactive postulated $Fe^{IV}_2(\mu\text{-}O)_2$ diamond core structure where both spin states have been found to be S = 2.[21] Because TQA enforces a S = 2 in the mono-oxoiron(IV) system, it may be possible that in a diiron system, TQA may enforce S = 2 iron centers in the corresponding $Fe^{IV}_2(\mu\text{-}O)_2$ diamond core, allowing for further insight into the diiron enzymatic systems that employ these highly oxidizing S = 2 high-valent iron centers. However, the existence of such a complex has not yet been demonstrated in synthetic complexes.

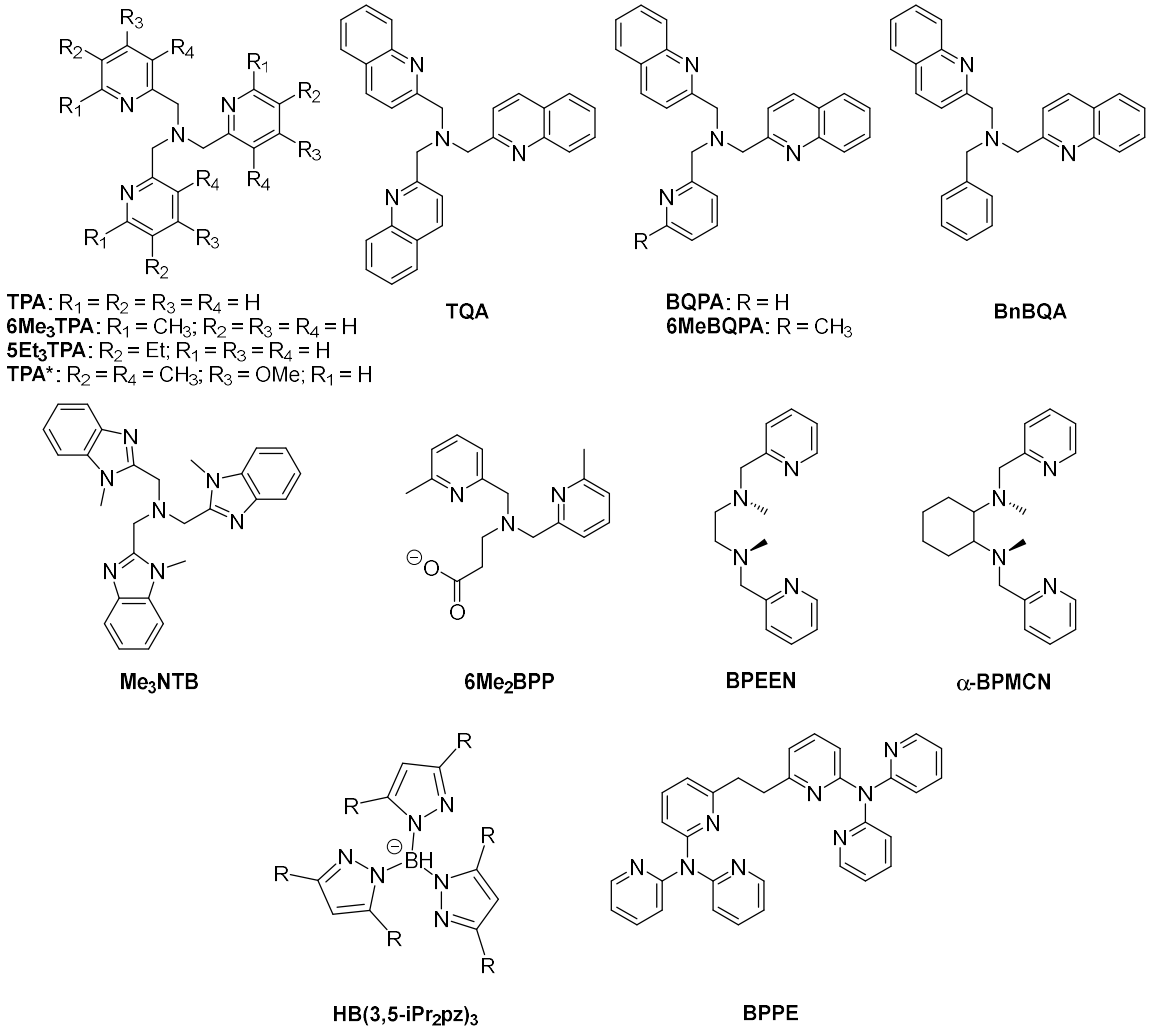

Figure 22. Collection of ligands discussed in this chapter.

Table 8. Comparison of diiron diamond core structures of diiron complexes. All distances are in Å. Values that are italicized are obtained through X-ray diffraction, while values in print are obtained using X-ray Absorption Spectroscopy. Ligand structures can be found in Figure 22.

Ligand	Fe^xFe^y (x, y)	Bridging moiety	Fe-O	Fe-O*	Fe-N_{ave}	Fe·····Fe	Fe-O-Fe angle (°)	Ref
TQA	2,2	OH,OH	1.98	2.24	2.24	3.17	97.2	t.w.
$6Me_3TPA$	2,2	OH,OH	*1.973(2)*	*2.168(2)*	*2.281(10)*	*3.187*	*100.55(9)*	[84]
$6Me_3TPA$	2,2	OH,OH	*1.995(2)*	*2.182(2)*	*2.288(12)*	*3.175*	*98.82(10)*	[82]
	a		*2.032(2)*	*2.208(2)*	*2.286(12)*	*3.221*	*98.75(10*	
TPA	2,2	OH,OH	*2.0059(15)*	*2.1595(16)*	*2.226(8)*	*3.087*	*95.57(6)*	[82]
TPA	2,2	OH,OH	*1.9726(17)*	*2.1344(18)*	*2.213(8)*	*3.010*	*94.20(7)*	[82]
BQPA	2,2	OH,OH	*1.9837(14)*	*2.1007(15)*	*2.296(74)*	*3.086*	*98.11(6)*	[82]
BnBQA	2,2	OH,OH	*1.985(2)*	*2.090(2)*	*2.263(11)*	*3.135*	*104.3*	[82]
HB(3,5-$iPr_2pz)_3$	2,2	OH,OH	*2.016(9)*	*2.04(1)*	*2.17(4)*	*3.179(5)*	*103.3(5)*	[141]
α-BPMCN	2,2	OH,OH	*2.050(2)*	*2.080(2)*	*2.252(11)*	*3.048*	*95.26(9)*	[142]
α-BPMCN	2	OH,OH	*2.084(2)*	*2.082(2)*	*2.214(12)*	*3.023*	*98.78(10)*	[142]
	3		*1.895(2)*	*1.897(2)*	*2.190(12)*	*3.023*	*98.78(10)*	[142]
TQA	3,3	O,O	*1.839(3)*	*1.917(3)*	*2.255(13)*	*2.6679(8)*	*90.5(1)*	[139]
			1.87	1.87	2.23	2.65	90.3	t.w.
$6Me_3TPA$	3,3	O,O	*1.842(5)*	*1.917(4)*	*2.242(34)*	*2.714(1)*	*92.4(2)*	[138]
			1.84	1.92	2.25	2.67		[143]
$6Me_3TPA$	3,3	O,OH	*1.890(7)*	*1.975(7)*	*2.202(28)*	*2.948(3)*	*99.4(3)*	[144]
	a		*1.895(10)*	*1.960(8)*	*2.197(29)*	*2.936(3)*	*99.2(5)*	[144]
			1.82	1.99	2.20	2.91	106	[145]
BQPA	3,3	O,OH	*1.897(3)*	*1.942(3)*	*2.188(16)*	*2.8926(9)*	*97.8(2)*	[144]

BPEEN	3,3	O,OH	*1.850(3)*	*1.976(4)*	*2.195(17)*	*2.835(1)*	*100.2(2)*	[144]
	a		*1.846(3)*	*1.993(4)*	*2.197(16)*	-	*91.1(2)* ∠*Fe-OH-Fe*	[144]
α-BPMCN	3,3	O,OH	*1.866(2)*	*1.989(2)*	*2.189(11)*	*2.867*	*91.97(9)*	[142]
TPA*	3,3	O,OH	*1.883(3)*	*1.934(2)*	*2.154(21)*	*2.7920(9)*	*94.0(1)*	[93, 146]
			1.80	1.97	2.14	2.80		[93]
TPA*	3,3	OH,OH	*1.926(2)*	*1.995(2)*	*2.114(26)*	*3.0224(10)*	*100.86(11)*	[93]
			1.91	1.91	2.10	3.04		[93]
5-Et_3TPA	3.5,3.5	O,O	*1.805(3)*	*1.860(3)*	*2.026(19)*	*2.683(1)*	*94.1(1)*	[81]
			1.82	1.82	2.00	2.61		[81]
TPA*	3.5,3.5	O,O	*1.781(4)*	*1.827(5)*	*1.995(13)*	*2.596(1)*	*92.0(2)*	[93]
			1.75	1.75	1.96	2.57		[93]
TPA*	4,4	O,O	*1.790(6)*	*1.809(8)*	*1.973(14)*	*2.711(4)*	*97.8(4)*	[93]
			1.77	1.77	1.97	2.73		[92]
Me_3NTB	4,4	O,O	1.78	1.78	1.97	2.70	98.7	[30]

t.w. - this work

a – second molecule found in the unit cell

3.3 — Generation and Structural Characterization of Complex 3

Exposure of **2** to H_2O_2 forms a new intermediate that can be trapped at – 40 °C. XAS data collected and analyzed shows that **3** has a K-edge energy of 7122.7 eV, which is blue-shifted from **1** by nearly 1 eV and very similar to that of **2** (Table 11). This result supports the assignment of **3** as a diferric species. Again, similar to complex **2**, the pre-edge feature of complex **3** is best fit by only 1 function centered at 7114.8 eV with a total pre-edge area of 19.1. It appears that the iron centers in **3** are less centrosymmetric when

compared to those found in complex **2** as evidenced by the larger pre-edge area found for **3**.

EXAFS data was also collected and fit for complex **3**. This intermediate has been found to be best fit with 2 Fe—N/O scatterers at 1.86 Å assigned to the two bridging oxygens, 4 Fe—N/O scatterers at 2.21 Å assigned to the nitrogens present in the TQA framework, an iron scatterer found at 3.15 Å, and lastly a carbon shell at 2.98 Å

EXAFS provides an important insight into the nature of the bridging oxygen atom. A short first shell of N = 2 and R = 1.86 Å is consistent with similar complexes and supports the assignment of a μ-O, μ-1,2-O_2 bridging moiety (Table 9). It is well known that iron complexes can support a Fe^{III}_2(μ-OH)(μ-1,2-O_2) formulation.[9] However, these complexes have bimetallic distances of around 3.4 Å and tend to have a longer first shell.[9, 25] The iron-iron distance that was found for complex **3** is very consistent with other reported values for $[Fe^{III}_2(\mu\text{-}O)(\mu\text{-}1,2\text{-}O_2)(L)_2]^{2+}$ complexes, helping to assign the overall connectivity of the peroxo core and support the hypothesis of no proton being present on the bridging oxygen atom.

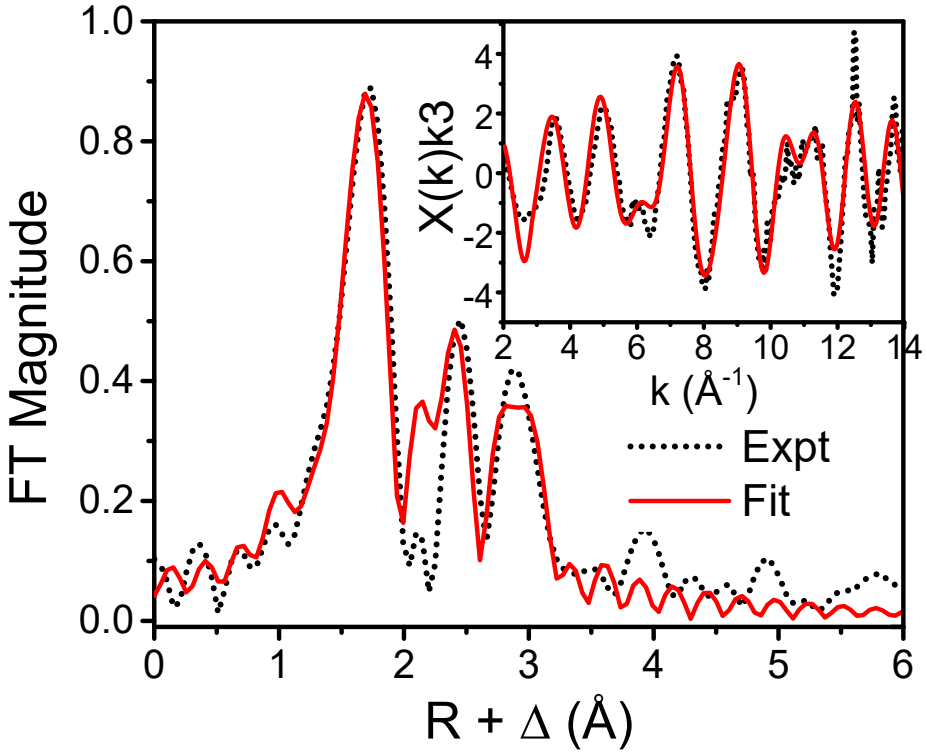

Figure 23. Fourier Transform EXAFS spectrum and the k-space data (inset) for $[Fe^{III}_2(\mu\text{-}O)(\mu\text{-}1,2\text{-}O_2)(TQA)_2]^{2+}$ (Fit 4).

Table 9. EXAFS fits for $[Fe^{III}_2(\mu\text{-}O)(\mu\text{-}1,2\text{-}O_2)(TQA)_2]^{2+}$ (3). Best fit in bold.

	Fe-N/O			Fe·····Fe			Fe·····C				GOF	
Fit	N	R (Å)	σ^2	N	R (Å)	σ^2	N	R (Å)	σ^2	E_0	F	F'
1	2	1.83	4.96							-7.15	892	545
2	2	1.86	5.03							-2.8	592	542
	4	2.21	5.44									
3	2	1.87	4.56	1	3.19	3.30				1.79	542	540
	4	2.23	6.40									
4	**2**	**1.86**	**4.60**	**1**	**3.15**	**1.71**	**8**	**2.98**	**4.22**	**-3.36**	**394**	**538**
	4	**2.21**	**5.95**									

k range = 2-14 $Å^{-1}$, resolution = 0.131 Å, σ^2 = mean-squared deviation in units of 10^{-3} $Å^2$. Scale Factor S_0^2 = 0.9. Goodness-of-fit (GOF) = F calculated as $F = \sqrt{\sum k^6(\chi_{exp} - \chi_{calc})^2}$. $F' = \sqrt{\sum k^6(\chi_{exp} - \chi_{calc})^2 / \sum k^6 {\chi_{exp}}^2}$.

Not surprisingly, we find that the structural features of the TQA-peroxo complex are nearly identical to those of the closely related $6Me_3TPA$ complex. This is consistent with the previous comparison between the diferric diamond core complexes (Table 8). While no XANES data were reported for the corresponding peroxo complex of $6Me_3TPA$, complex **3** has a pre-edge area and a K-edge value very consistent with other reported complexes, like those found for the 6MeBQPA and BQPA complexes.[147] An interesting outlier in Table 10 is the Me_3NTB-ligated complex, where the K-edge has been reported as being more than 2 eV higher than the next most blue-shifted value, namely the BnBQA-ligated complex at 7124.2 eV. Additionally, the Me_3NTB framework is one of only two

synthetic ligand frameworks that have been found competent to support a $Fe^{IV}_2(\mu\text{-}O)_2$ core structure, species of great interest due to their similarity to sMMOH-**Q**.[30] There may be something unique about the precursor to the high-valent diamond core that allows the activation of the O—O bond to form the **Q**-mimic complex. Further investigation into the TPA*-ligated oxygen activation mechanism is required as this is the other ligand framework that has been found to support a $Fe^{IV}_2(O)_2$ core structure.[93] At this time unfortunately, we have not yet found a way to activate the O—O bond in complex **3** and unlock the proposed $Fe^{IV}_2(O)_2$ species that may feature $S = 2$ iron centers.

Table 10. Comparison of structural and XANES data for different peroxo complexes with the general formula $[Fe^{III}_2(\mu\text{-}O)(\mu\text{-}1,2\text{-}O_2)(L)_2]^{2+}$ where L is the ligand listed in column 1. Ligand structures can be found in Figure 22. All distances in columns 2-4 are in units of Å. Values in italics are obtained through X-ray diffraction.

Ligand (L)	Fe-O	Fe-OO	$Fe\text{-}N_{ave}$	Fe·····Fe	pre-edge area (units)	K-edge (eV)	Ref
TQA	1.86	1.86	2.21	3.15	19.1	7122.7	t.w.
$6Me_3TPA$	1.84	1.84	2.23	3.14	nr[a]	nr[a]	[143]
6MeBQPA	1.83	1.83	2.19	3.14	20.4	7122.8	[147]
BQPA	1.82	1.82	2.17	3.13	18.3	7122.7	[147]
BPPE	1.77	1.94	2.11	3.04	29.1	7123.6	[147]
BnBQA	1.81	1.92	2.21	3.16	15.1	7124.2	[83]
Me_3NTB	1.84	1.84	2.11	3.07	18.2	7126.3	[30]
$6Me_2BPP$	*1.743(7)*	*2.102(8)*	*2.18(23)*	*3.171(1)*	-	-	[148]

[a] – not reported
t.w. – this work

Comparing all 3 complexes reported in this study amongst each other can provide insight into the sequential oxidation found in biological systems. Notably, the iron-oxygen distances fit by EXAFS for complex **3** have been found to be similar in bond length to the diferric diamond core complex **2** and the iron-iron distance elongates to nearly the same value found for complex **1**. It might have been expected that upon the oxidation of the iron centers from 2+ to 3+ should result in the slight contraction of the iron-nitrogen ligand distances. For example, the $Fe—N_{ave}$ = 2.30 Å value of the $Fe^{II}_2(OH)_2$BQPA complex has been found to shorten to 2.19 Å upon core oxidation to $Fe^{III}_2(\mu\text{-}O)(\mu\text{-}OH)$, a change of

about 0.1 Å (Table 8).[82, 144] As an example of a 3^+–to–4^+ oxidation, the $[Fe^{III}_2(\mu\text{-}O)(\mu\text{-}1,2\text{-}O_2)(Me_3NTB)_2]^{2+}$ complex with a $d(Fe—N)_{ave}$ of 2.11 Å has been demonstrated to contract to 2.03 Å upon oxidation of both iron centers to a $Fe^{IV}_2(\mu\text{-}O)_2$ diamond core structure.[30] Additionally, a DFT structure has been reported for the complex $[Fe^{IV}(O)(TQA)(CH_3CN)]^{2+}$.[39] This monoiron complex was calculated as having an $Fe—N_{ave}$ = 2.15 Å, which includes the elongated $Fe—NCCH_3$ bond of 2.27 Å. Therefore, one would expect the metal-ligand bond distances to shorten upon oxidation; however, in this diiron system, that does not appear to be the case and may be a useful parameter when evaluating the propensity for ligand frameworks to support high-spin *S* = 2 iron centers.

Table 11. Comparison between best EXAFS fits for the complexes explored in this study. All complexes are ligated by two TQA molecules and have an overall charge of 2+.

	Fe-N/O			Fe·····Fe			Fe·····C			E	GOF	
Complex	N	R (Å)	σ^2	N	R (Å)	σ^2	N	R (Å)	σ^2		F	F’
$Fe^{II}_2(\mu\text{-}OH)_2$	1	1.99	4.06	1	3.17	1.16	6	3.03	1.95	-5.07	496	540
1	5	2.24	4.78									
$Fe^{III}_2(\mu\text{-}O)_2$	2	1.87	3.58	1	2.65	2.22	4	2.99	4.5	-3.80	333	413
2	4	2.23	5.03									
$Fe^{III}_2(\mu\text{-}O)$ $(\mu\text{-}1,2\text{-}O_2)$	2	1.86	4.60	1	3.15	1.71	8	2.98	4.22	-3.36	394	538
3	4	2.21	5.95									

σ^2 = mean-squared deviation in units of 10^{-3} Å^2 . Scale Factor S_0^2 = 0.9. Goodness-of-fit (GOF) = F calculated as $F = \sqrt{\sum k^6\left(\chi_{exp} - \chi_{calc}\right)^2}$. $F' = \sqrt{\sum k^6\left(\chi_{exp} - \chi_{calc}\right)^2 / \sum k^6 {\chi_{exp}}^2}$.

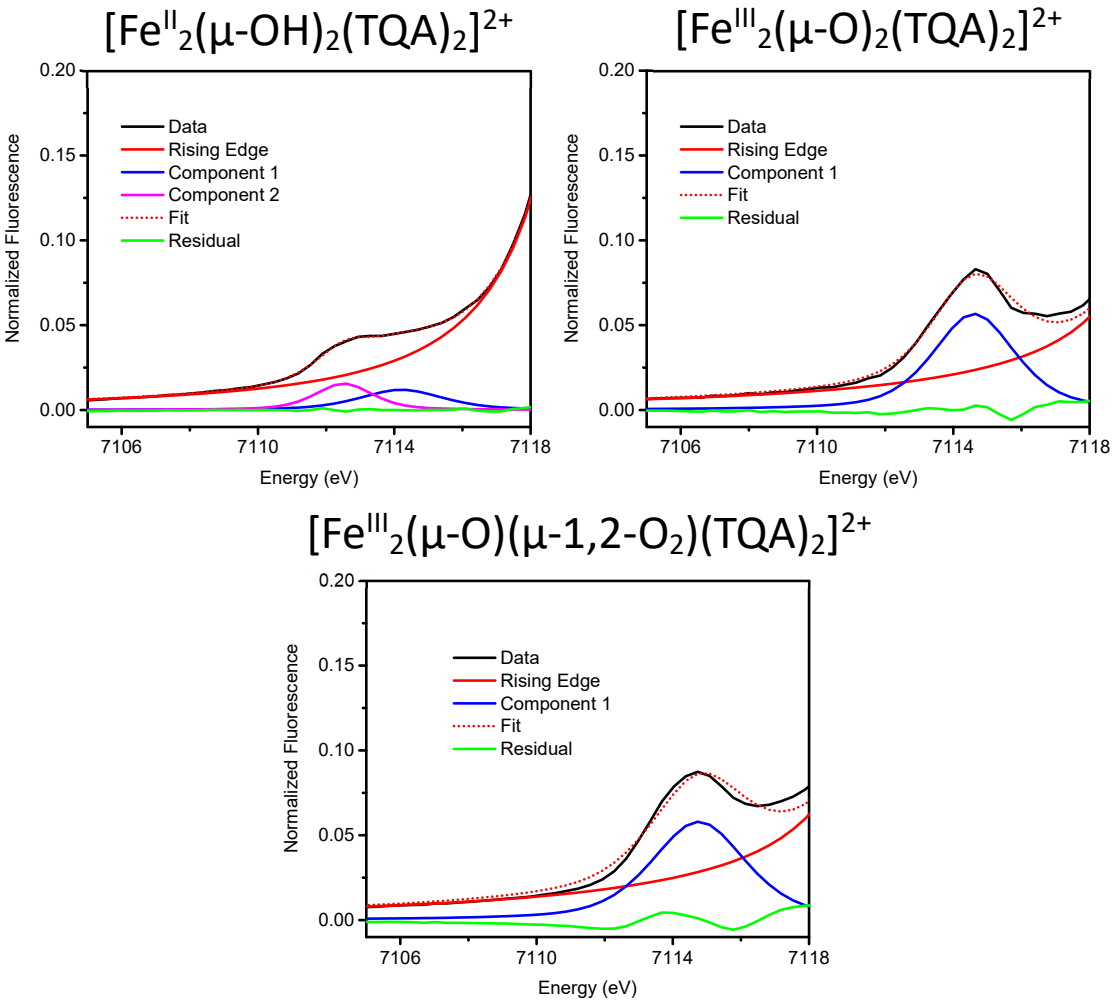

Figure 24. Pre-edge area fitting of all 3 complexes explored in this study.

3.4 — Conclusion

This study demonstrates that a clear structural picture can be painted for the oxidation of diiron systems on a pathway towards high-valent sMMOH-**Q**-like intermediates. Firstly, a bimetallic complex, namely **1**, can be formed upon the addition of base to a solution containing monoiron(II) starting material. Complex **1** has been well

characterized as having a $Fe^{II}_2(\mu\text{-}OH)_2$ core structure, which is found to be quite distorted, with very dissimilar iron-oxygen bond lengths as found in a collection of crystal structures of similar complexes (Table 8). Upon the exposure of this solution to molecular oxygen, a new intermediate is observed and characterized, namely complex **2**. A clear shift of 1 eV is observed in the K-edge energy upon the oxidation of complex **1** to **2**. Comparing the best EXAFS fits of complexes **1** and **2**, the two striking differences are the contractions of the iron-oxygen bond lengths as well as the reduction in the bimetallic distance (Table 11). The only other structurally characterized $Fe^{III}_2(\mu\text{-}O)_2$ complex, namely the $6Me_3$TPA-ligated complex **2**, shows a significant distortion in core structure as well. Additionally, complex **2** has been crystallographically characterized.[139] Importantly, the agreement between the EXAFS and XRD structures for complex **2** demonstrates that both the solution- and solid-state compositions are nearly identical. Then, H_2O_2 has been added to a solution containing complex **2**, forming an intermediate that has been demonstrated to be consistent with a $Fe^{III}_2(\mu\text{-}O)(\mu\text{-}1,2\text{-}O_2)$ structure, similar to the intermediate sMMOH-**P** which contains a bridging peroxo unit. Complex **3** has been found to have a similar K-edge energy as complex **2**, supporting the assignment of the iron(III) oxidation states. urther investigation is required to figure out a way to activate the O—O bond and achieve an $Fe^{IV}_2(O)_2$ diamond core structure where both iron centers are likely to be $S = 2$. Such a transformation could provide the first synthetic mimic of sMMOH-**Q** with an electronic structure that matches that of the enzymatic complex **Q**.

Chapter 4: Modeling Transient Enzymatic Oxoiron(IV) Complexes

4.1 — Introduction

Nature employs high-valent oxoiron intermediates to perform powerful oxidations (CCC3). A class of enzymes known as non-heme iron oxygenases feature many common structural and mechanistic features. One of the best characterized non-heme enzymes is taurine: α-ketoglutarate dioxygenase (TauD). TauD is known to activate oxygen to form an oxoiron(IV) intermediate (TauD-***J***) that is capable of oxidizing the strong C-H bond found in taurine.[11] Like many non-heme enzymes, TauD is ligated by 2 histidines and 1 carboxylate-containing amino acid (aspartate or glutamate) in a triangular array commonly referred to as the facial triad.[149] As the name suggests, TauD utilizes the co-

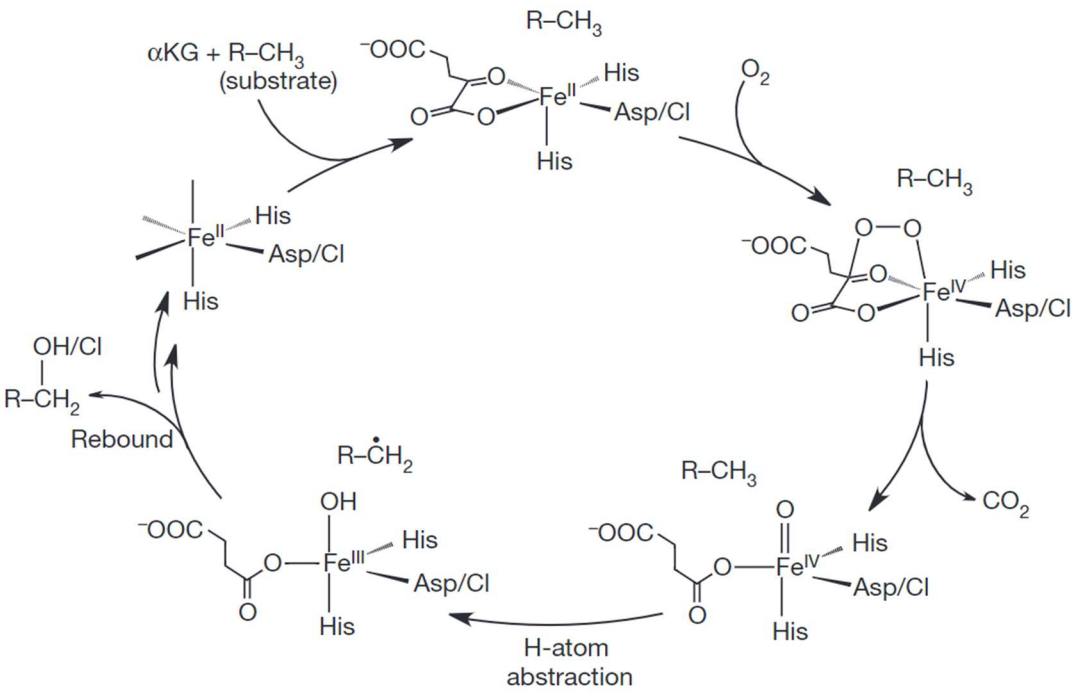

Figure 25. Generic catalytic cycle of the oxidation of alkyl products performed by α-ketoglutarate dioxygenase-dependent non-heme iron enzymes. Adapted from Ref [1] with permission.

substrate α-ketogluarate (αKG) to help facilitate the activation of oxygen. αKG is oxidized by molecular dioxygen to generate the powerful oxidant TauD-***J***. TauD-***J***, first trapped and characterized in 2003, is the first enzymatic oxoiron(IV) species to be observed in a non-heme enzyme.[137] This intermediate was found by XAS analysis to have an iron-oxygen bond length of 1.62 Å,[16] consistent with other oxoiron(IV) complexes that have been characterized in the subsequent years.[9]

Similar to the oxygenase class of non-heme iron enzymes, there are also halogenase enzymes that use a similar ligand environment, except that the carboxylate is replaced by a halogen (Asp/Cl in Figure 25). Several years after the trapping of TauD-***J***, a breakthrough article by Walsh, Green, Krebs, Bollinger, and coworkers reported the structure of the oxoiron(IV) intermediate found in the SyrB2-Cl enzymatic cycle.[19] The chloroferryl intermediate was found by XAS to have an iron-oxygen bond length of 1.66 Å,[19] slightly longer than the Fe=O bond length found for TauD-**J**.[16] Additionally, the SyrB2*Fe(II)*α-KG*Cl^- species was also structurally characterized by EXAFS to have a notable Fe—Cl distance of 2.40 Å, which contracts to 2.31 Å upon the oxidation of the iron(II) center to iron(IV).[19]

Both TauD and SyrB2 as well as other non-heme iron enzymes serve as inspiration to synthesize analogues to the enzymatic oxoiron(IV) intermediates. The first oxoiron(IV) crystal structure was obtained with the macrocycle ligand tetramethylcyclam (TMC), namely $[Fe^{IV}(O)(TMC)(CH_3CN)]^{2+}$ (1'-$NCCH_3$).[48] This complex was fully characterized and found to have an Fe=O bond distance of 1.646 Å.[48] The crystallization and further

characterization of 1'-$NCCH_3$ generated much interest in exploring derivatives of this ligand framework. Because TMC is a cyclam-type ligand, there is an open coordination site *trans* to the oxo moiety, which allows the introduction of various functional groups at this position, both tethered (1-L) and untethered (1-L'), to form a number of TMC derivatives with 6th ligands that can modulate the electronic structure of the oxoiron unit while maintaining a consistent steric environment.

4.2 — Characterization of Fe^{II}(TMC)-like Complexes

To broaden our understanding of the electronic structure of the iron center in these enzymes, the first ligand employing the histidine analogue imidazole has been synthesized and characterized structurally. The TMC-im ligand features a pendant methyl imidazole attached to one of the nitrogen atoms on the cyclam ligand. TMC-im represents an effort to make the coordination environment of the iron center to more closely resemble those of the enzymes where the facial triad is present. As imidazole is an electronic analogue to histidine, a better understanding of the electronic structure of non-heme iron active sites may be obtained.

Initial efforts have been undertaken to characterize the Fe^{II}(TMC-im) starting material. This species was crystallized by vapor dilution of diethyl ether into an acetonitrile solution of the iron(II) complex at room temperature inside an inert atmosphere glovebox. This structure was solved and found to be consistent with the suggested complexation of $[Fe^{II}(TMC\text{-}im)]^{2+}$ with no extraneous ligand coordinated in the 6th position *trans* to the imidazole (Figure 26). Importantly, bond lengths could be

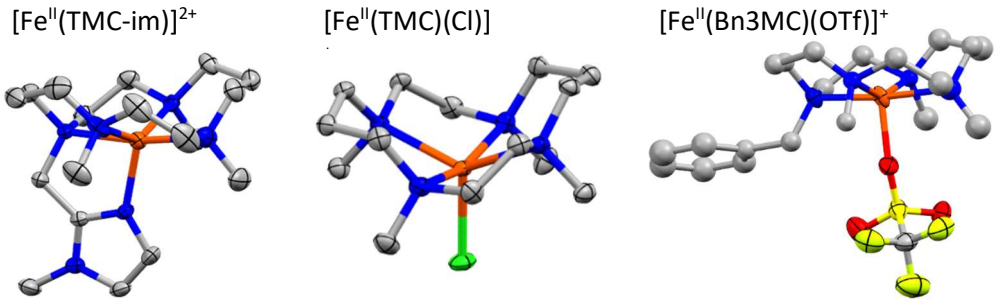

Figure 26. Crystal structures of three TMC-related iron(II) structures. Selected bond lengths available in Table 12. Additional structural information for both $[Fe^{II}(TMC\text{-}im)]^{2+}$ and $[Fe^{II}(TMC)(Cl)]^{+}$ are available at the end of this chapter. Additional information for $[Fe^{II}(Bn3MC)(OTf)]^{+}$ has been published in Ref [4].

resolved, and the Fe^{II}(TMC-im) complex is found to have an Fe–N_{ave} distance = 2.175 Å and an Fe—N_{im} distance = 2.077 Å. Additional crystallographic efforts were made in this work to crystallize the Fe^{II}(TMC) complex with an ancillary chloride ligand bound to the metal center (Figure 26). These two structures together with that of $[Fe^{II}(Bn3MC)(OTf)]^{+}$ complement earlier efforts of Schindler and coworkers on $[Fe^{II}(TMC)(L)]^{2+/+}$ (L = CH_3CN, OTf, H_2O) to provide an overview of the structural changes upon varying the nature of the axial ligand in iron(II) complexes.[4, 49] Comparison of the structural features of the six solved structures shows some similarities and trends, with all structures having similar average Fe—N_{eq} distances of around 2.2 Å (Table 12). Interestingly, the Fe—O_{axial} bond distance for L_{ax} = H_2O is 2.005 Å, the shortest among the six complexes and even shorter than found for the two complexes with Fe—OTf bonds despite the anionic nature of the triflate. This difference may be owed to steric effects of the bulkier O–SO_2CF_3 group bound to the metal center or, more likely, to the greater basicity of the water ligand. As expected, the iron-chloride bond is the longest at 2.284 Å, the longest metal-ligand bond

length found among the six structures.

Something to note for the crystallographic efforts of TMC-like complexes is the severe disorder that is found during refinement. All six of these structures feature high amounts of disorder due to the cyclam framework being nearly symmetric due to the alternating ethylene and propylene bridges in the macrocycle. This near-symmetry has resulted in full molecule disorder that leads to higher least-squares refinement factors reported in both this work and the published literature.[4, 49] The Bn3MC crystal structure determination features hypersymmetry around a local center (Z' = 2). This is reported to be not uncommon in the space group that the Bn3MC structure was solved in, $Pna2_1$.[150] This structure suffered from whole molecule disorder of the cationic group, whereby the ligand framework featuring alternating ethylene and propylene bridges was disordered. This required each cation to be modeled with two independent fragments, with occupancies 0.58:0.42 and 0.73:0.27, respectively. Finally, the Flack X parameter suggested that the data should be modeled as an inversion twin. These issues have led to a difficult least-squares refinement. Thus, many refinement restraints and constraints were included in this refinement. Even in the Fe^{II}(TMC-im) structure, where the ligand is pentadentate and should therefore be more rigid when compared to Bn3MC, significant disorder is still found, specifically in the alternating ethylene and propylene bridges as previously discussed. However, this structure can still be refined anisotropically, albeit with several restraints and constraints included in the refinement. A similar refinement was also required for the chloride-bound Fe^{II}(TMC) structure. Similar refinements were

also required for the three structures contributed by Schlinder and coworkers.[49] Therefore, the Bn3MC structure stands out as the most difficult structure, likely due to the non-tethered, pendant benzyl arm combined with the space group which leads to the hypersymmetry found in the unit cell.

Table 12. Comparison of single crystal X-ray diffraction of iron(II) complexes ligated by TMC-related complexes. The atom (L) in parentheses in column 3 indicate the metal-L bond.

Complex	Fe-N_{eq}(ave) (Å)	Fe-L_{axial} (Å)	Ref
[Fe(II)(TMC-im)]OTf	2.175	2.077 (N)	this work
[Fe(II)(TMC)(Cl)]$FeCl_4$	2.219	2.284 (Cl)	this work
[Fe(II)(Bn3MC)(OTf)]OTf	2.206	2.073 (O)	4
[Fe(II)(TMC)(CH_3CN)]$(OTf)_2$	2.177	2.056 (N)	49
[Fe(II)(TMC)(OTf)](OTf)	2.192	2.025 (O)	49
[Fe(II)(TMC)(OH_2)]$(OTf)_2$	2.197	2.005 (O)	49

4.3 — Characterization of Corresponding High-Valent Oxoiron(IV) Intermediates

After sufficient structural characterization of the iron(II) starting material, efforts have been made to form high-valent intermediates. TMC-im has been found competent to support the formation of an oxoiron(IV) complex $[Fe^{IV}(O)(TMC\text{-}im)]^{2+}$. The addition of 1 equivalent of an iodosylbenzene derivative (sPhIO) to a solution containing starting Fe^{II}

complex results in the formation of the oxoiron(IV) complex with a near IR feature observed at λ_{max} = 820 nm (ε = 300 M^{-1} cm^{-1}). Both the λ_{max} and ε values resemble those found for related oxoiron(IV) complexes,[9] supporting the initial assignment of this species as being an $Fe^{IV}(O)$ complex.

While this species is relatively thermally unstable with a $t_{1/2}$ = 30 min at 25 °C, frozen solution XAS can be performed in lieu of XRD. A solution of oxoiron(IV) complex can be freeze-quenched in liquid nitrogen and then structural data can be collected. The XAS spectrum can be broken into two regions: extended X-ray absorption fine structure spectroscopy (EXAFS) and X-ray at near-edge spectroscopy (XANES). The EXAFS region can be fit mathematically to provide insight into different "shells", where each shell consists of three values: the coordination number (N) or number of atoms in a shell, the distance (R) of the shell from the metal center, and the Debye-Waller factor (σ), which is the thermal displacement of the shell. The quality of fit can be assessed by the Goodness-of-Fit (GOF) value where, simply put, the goal is to minimize the F value while abiding by the resolution restrictions of the data quality, which can be found in the footnote of the tables associated with the fittings.

For the $[Fe^{IV}(O)(TMC\text{-}im)]^{2+}$ complex, the EXAFS region is best fit by 4 shells: a short N = 1 bond length at 1.65 Å, a longer shell of N = 5 at 2.07 Å, and two carbon shells both N = 4 at 2.96 Å and 3.40 Å (Figure 27, Table 13). The short first shell can be assigned to the iron-oxygen bond as this has been typically observed at this distance for Fe=O bonds in both TMC- and non-TMC-ligated oxoiron(IV) complexes (Table 14).[9, 51, 151, 152] The TMC-

im complex is among the shorter of the oxoiron(IV) bond lengths. The second shell is likely due to the iron-nitrogen bonds for the ligand framework found at 2.07 Å. This distance is shorter than the Fe—N_{eq}(ave) observed for the Fe^{II} complex at 2.18 Å (Table 12). This contraction is to be expected upon the two-electron oxidation of the iron center. The assignment of two carbon shells is typical for cyclam-type frameworks.[151]

XANES data has been gathered and compared alongside similar complexes. The K-rising edge value was found to be 7124.2 eV, consistent with the assignment of an iron(IV) oxidation state for this complex. The pre-edge area can provide insight into the centrosymmetry around the metal center. A high value of 30 units has been found and is consistent with other oxoiron(IV) complexes (Table 14). All the XAS data taken together clearly supports the assignment of the oxidized intermediate as being the $[Fe^{IV}(O)(TMC\text{-}im)]^{2+}$ complex.

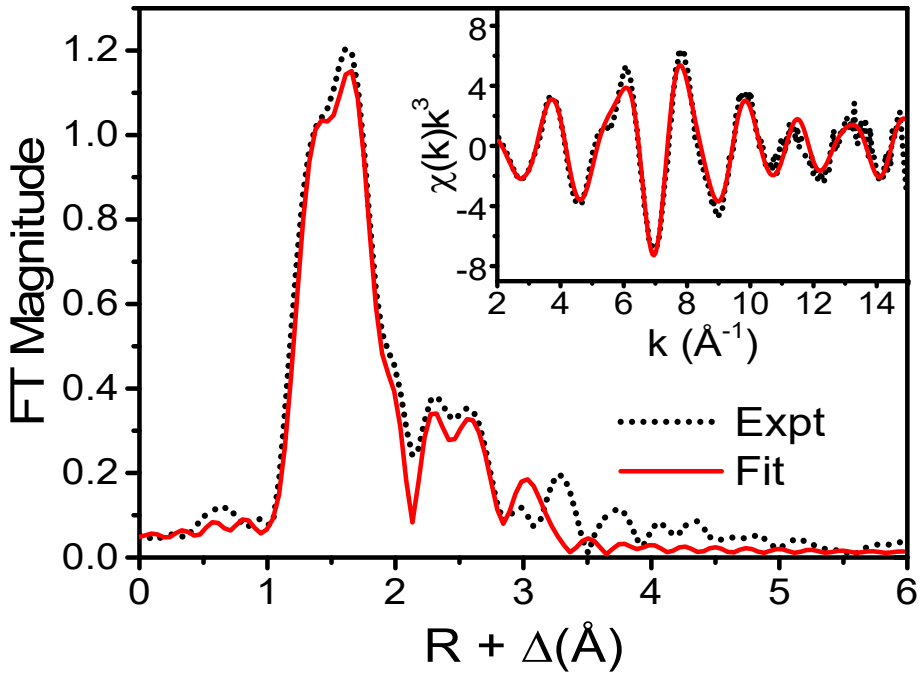

Figure 27. Fourier transformed EXAFS spectrum and the k-space data (inset) for $[Fe^{IV}(O)(TMC\text{-}im)]^{2+}$ (Fit 4).

Table 13. EXAFS fits for $[Fe^{IV}(O)(TMC\text{-}im)]^{2+}$ (1-Im). Best fit in bold.

	Fe-N/O			Fe·····C			GOF		
Fit	N	R (Å)	σ^2	N	R (Å)	σ^2	E_0	F	F'
1	1	1.70	2.98				-1.66	760	546
2	1	1.65	3.74				-3.37	646	544
	5	2.07	3.74						
3	1	1.65	3.27	4	2.96	5.22	-2.06	596	542
	5	2.07	3.39						
4	**1**	**1.65**	**3.25**	**4**	**2.96**	**5.62**	**-5.07**	**496**	**540**
	5	**2.07**	**3.39**	**4**	**3.40**	**4.82**			

k range = 2-15 $Å^{-1}$, resolution = 0.121 Å, σ^2 = mean-squared deviation in units of 10^{-3} $Å^2$. Scale Factor S_0^2 = 0.9. Goodness-of-fit (GOF) = F calculated as $F = \sqrt{\sum k^6(\chi_{exp} - \chi_{calc})^2}$. $F' = \sqrt{\sum k^6(\chi_{exp} - \chi_{calc})^2 / \sum k^6 \chi_{exp}{}^2}$.

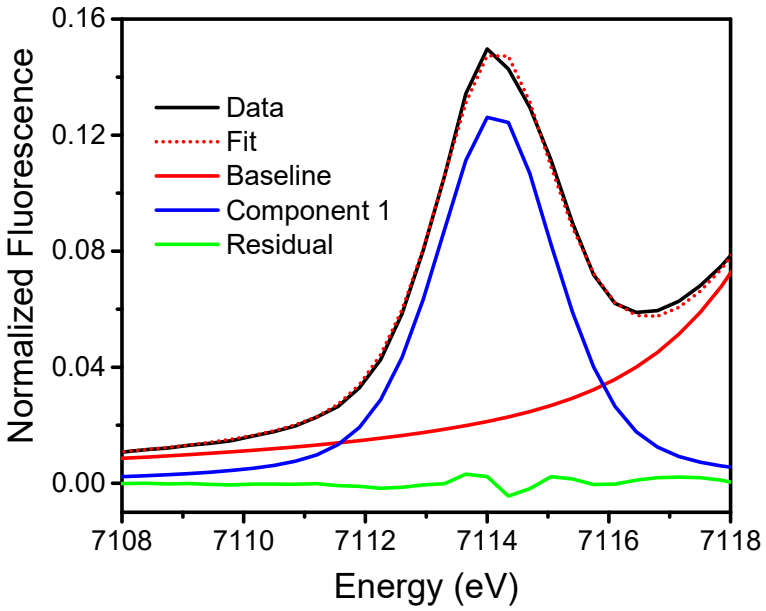

Figure 28. Pre-edge area fitting of $[Fe^{IV}(O)(TMC\text{-}im)]^{2+}$.

Table 14. Comparison of XANES and Fe=O bond distance for TMC oxoiron(IV) structures with the generic structure $[Fe^{IV}(O)(L)]^{2+/+}$. In column one, 1 corresponds to an $Fe^{IV}(O)$ with a TMC ligand framework derivative where the 6th ligand is bound through a nitrogen present in the cyclam. Complexes with 1' indicate that the 6th coordinating ligand is non-pendant. Weighted area is calculated as: pre-edge area/yield.

Ligand (L)	K-edge (eV)	peak position (eV)	pre-edge area (units)	weighted area (units)	*r*(Fe=O) (Å)	ref
1-im	7124.2	7114.2	30	30	1.65	this work
1'-NCMe	7124.5	7114.1	26	33	1.64	[151]
1'-O_2CCF_3	7124.0	7114.2	31	39	1.64	[151]
1'-NCO	7125.3	7114.7	26	31	1.67	[151]
1'-NCS	7125.4	7114.3	24	29	1.65	[151]
1'-N3	7125.3	7114.4	24	30	1.66	[151]
1-SR	7125.1	7114.3	18	20	1.70	[151]
1'-CN	7124.8	7114.1	21	26	1.66	[151]
1'-OH	7125.4	7115.1	20	22	1.68	[151]
1-dma	7125.9	7114.2	30	30	1.63	[51]
1-dma-H^+	7125.8	7114.1	21	23	1.67	[51]
1-OAc	7124.7	7114.0	27	28	1.64	[152]
1-OPr	7125.4	7114.2	22	31	1.65	[152]
1'-OAc	7125.0	7114.2	30	31	1.65	[152]

4.3.1 — Structural Characterization of Oxoiron(IV) Species

There has been a great interest in the crystallographic characterization of oxoiron(IV) intermediates ever since the first crystal structure obtained in 2003.[48] Of the over-100 high-valent oxoiron complexes that have been reported, only sixteen of these complexes have been crystallographically characterized as of 2021.[9] The Que research group has contributed several of the structures, with a few being reported in recent years.

We reported two structures of oxoiron(IV) complexes using a crystallization method that has proved to be successful for obtaining crystals of these high-valent iron complexes.[3, 56] This methodology requires the pre-solubilizing of ~10 equiv $NaClO_4$ and 4 equiv ceric ammonium nitrate (CAN) in water, resulting in a yellow solution. This solution is then mixed with 1 equiv of starting iron(II) triflate salt complex dissolved in minimal acetonitrile. Upon mixing, this solution typically changes color immediately, usually some shade of green due to the typical UV-Vis-NIR absorption of oxoiron(IV) complexes.[9] The now-reacted solution is immediately place in a 0 °C freezer to allow slow evaporation of the solvent over the course of several hours to several days, depending on the stability of the complex. The employment of $NaClO_4$ provides the counteranion ClO_4^- that has been useful for crystallization when compared to triflate. CAN is the oxidant in solution which oxidizes the iron(II) to iron(IV) while the oxygen comes from the water used for dissolving the $NaClO_4$ and CAN. These ratios of reagents may need to be altered slightly depending on the stability of the oxoiron(IV) complex and the inherent crystallinity of the ligand framework and iron complex in general.

This methodology led to the successful crystallization and characterization of two complexes: $[Fe^{IV}(O)((5Me)_2\text{-}N4Py)]^{2+}$ and $[Fe^{IV}(O)(Py_5Me_2)]^{2+}$, both of which have been reported.[56] Efforts have been made towards the crystallization of the $[Fe^{IV}(O)(TMC\text{-}im)]^{2+}$ complex. Initial efforts proved to be conditionally successful. Low-quality crystals were obtained and proved to be severely disordered. The crystals were microscopic in size, likely due to the thermal instability of the oxoiron(IV) complex not allowing for high

quality crystals to grow over the course of several hours. The severe disorder observed is similar to the efforts towards crystallization of the iron(II) complexes, but the stability of the iron(II) complexes allowed for higher quality crystals to be grown. The ligand framework of TMC-im was fully disordered and proved to be too difficult to model at a publication quality. A caveat is that the iron-oxygen bond could be easily identified in the electron density map, allowing for a preliminary bond length of 1.65 Å to be found upon anisotropic refinement of the iron and oxygen atoms (Table 15). This value compares well with the Fe=O bond length of 1.65 Å obtained from EXAFS analysis. While the XRD model is of insufficient quality for publication at this moment, the agreement between the EXAFS and XRD bond lengths further support the assignment of the TMC-im complex as being the proposed $[Fe^{IV}(O)(TMC\text{-}im)]^{2+}$ complex.

Table 15. Comparison of data obtained for eleven of the crystallographically characterized complexes.

Complex	λmax (nm) (ε (1/(M*cm)))	r(Fe=O) (Å)	XANES pre-edge (units)	half-life (25 °C)	Refs
$[Fe^{IV}(O)(TMC\text{-}im)]^{2+}$	820 (300)	1.65	30	0.5 h	this work
$[Fe^{IV}(O)(TMC)(MeCN)]^{2+}$	824 (400)	1.646	33	10 h	48, 151, 153
$[Fe^{IV}(O)(TMC)(H_2O)]^{2+}$	820 (250)	1.650	-	-	153
$[Fe^{IV}(O)(TMC\text{-}py)]^{2+}$	834 (260)	1.667	34	7 h	51, 154
$[Fe^{IV}(O)(TMC\text{-}dma)]^{2+}$	810 (270)	1.658	30	120 h	51
$[Fe^{IV}(O)(N4Py)]^{2+}$	695 (400)	1.639	34	60 h	2, 53, 154, 155
$[Fe^{IV}(O)((5Me)_2\text{-}N4Py)]^{2+}$	695 (-)	1.654	-	60 h	56
$[Fe^{IV}(O)(N4Py^{2PhF2})]^{2+}$	750 (250)	1.666	-	-	54, 116
$[Fe^{IV}(O)(N2Py2B)]^{2+}$	725 (450)	1.656	-	2.5 h	3, 156
$[Fe^{IV}(O)(N2Py2Q)]^{2+}$	770 (380)	1.677	-	2.5 h	3, 157
$[Fe^{IV}(O)(Py5Me_2)]^{2+}$	712 (310)	1.656	-	2 h	56, 158

4.3.2 — HAT Reactivity of Oxoiron(IV) Species

The $[Fe^{IV}(O)(TMC\text{-}im)]^{2+}$ complex was explored for its oxidative power towards 1,4-cyclohexadiene and compared to other cyclam-based complexes. The reactivity of the TMC-im complex is unremarkable, being comparable to that of the parent $[Fe^{IV}(O)(TMC)(CH_3CN)]^{2+}$ complex but slightly less reactive than the related TMC-py derivative (Table 16). However, the half-life of the TMC-im complex is more than an order

of magnitude shorter than the other two. One might hypothesize that the imidazole sixth ligand is more basic compared to the MeCN or pyridine found in the other two, which may stabilize the high-valent iron(IV) center. It is unclear at the present time why the TMC-im complex is much less stable than the other two. Substitutions on the imidazole ring to perturb the basicity of the iron center may shed light on this hypothesis. Another hypothesis may be that the pendant imidazole moiety is more susceptible to degradation that the pyridine found in TMC-py or the acetonitrile in the parent TMC complex.

Table 16. Comparison of self-decay and reactivity for TMC and TMC-like oxoiron(IV) complexes.

Complex	**$t_{1/2}$ (h) 25 °C**	**CHD[a] k_2 (M^{-1} s^{-1}) 0 °C**	**Ref**
$[Fe^{IV}(O)(TMC)(CH_3CN)]^{2+}$	10	0.12	[159]
$[Fe^{IV}(O)(TMC\text{-}py)]^{2+}$	7	0.22(1)	[50]
$[Fe^{IV}(O)(TMC\text{-}im)]^{2+}$	0.5	0.14	this work
$[Fe^{IV}(O)(TMC\text{-}dma)]^{2+}$	120	0.037	[51]
$[Fe^{IV}(O)(TMC\text{-}dma\text{-}H]^{+}$	~1.5 (0 °C)	0.016	[51]

[a] - 1,4-cyclohexadiene

4.4 — Comparison of Oxoiron(IV) Complexes Modulated by Sterically-Imposed Tilt of the Iron-Oxo Bond

Similar to the TMC framework, the N4Py ligand framework has been used to gain insight into electronic and steric effects on the oxoiron(IV) unit. The high stability of the $[Fe^{IV}(O)(N4Py)]^{2+}$ complex has allowed for its complete characterization, crystallographically, spectroscopically and through reactivity.[2, 53, 154, 155] This complex was found competent towards the hydroxylation of cyclohexane (BDE = 99.5 kcal/mol) with a rate of 5.5 x 10^{-6} M^{-1} s^{-1}. While this rate is incredibly low, this result nonetheless demonstrates the capability of this complex to cleave the strong C-H bonds of cyclohexane, something that the $[Fe^{IV}(O)(TMC)(CH_3CN)]^{2+}$ complex has been demonstrated as being incompetent to do.

The N4Py ligand proved to be a useful framework, allowing for many substitutions at the pyridine sites.[9] In fact, some patterns emerge upon further observation of reported data alongside efforts performed herein. Recently, two of the pyridines have been substituted with quinolines and both the Fe^{II} precursor $[Fe^{II}(OTf)(N2Py2Q)]^{+}$ and the $Fe^{IV}(O)$ derivative $[Fe^{IV}(O)(N2Py2Q)]^{2+}$ were crystallographically characterized.[3] Notably, the N_{axial}–Fe–O unit of $[Fe^{IV}(O)(N2Py2Q)]^{2+}$ was observed to be substantially tilted when compared to the parent complex (170.5° vs 178.6°). This structural difference is interesting as the $[Fe^{IV}(O)(N2Py2Q)]^{2+}$ complex has been found to have a C-H bond activation rate of 2.9 x 10^{-2} M^{-1} s^{-1} (25 °C, substrate = cyclohexane), four orders of magnitude faster than the corresponding N4Py complex.[3] It has been hypothesized that

the imposed tilt of the steric interaction due to the quinoline is what gives rise to this increased reactivity.

To further explore this, we synthesized derivatives of the N4Py ligand. Briefly, the N4Py ligand framework contains two "halves". One half consists of two pyridines each bound to the central amine through a methylene carbon (*methylene*), while the other half consists of two pyridines bound geminal to a methine carbon that is connected to the central amine (*methine*). We synthesized and characterized the complex $[Fe^{IV}(O)(6Me_2N4Py)]^{2+}$ where the pyridines on the *methylene* half of the N4Py framework has been substituted with methyl groups at the 6-position. DFT optimized structures of the complex and its "partner" $[Fe^{IV}(O)(N4Py^{Me2})]^{2+}$ complex where the *methine* pyridines are substituted with 6-position methyl groups.[5] When these four complexes are looked at together, a clear tilt to the N_{axial}–Fe–O unit is imposed upon substitutions to the *methylene* side of the N4Py complex.

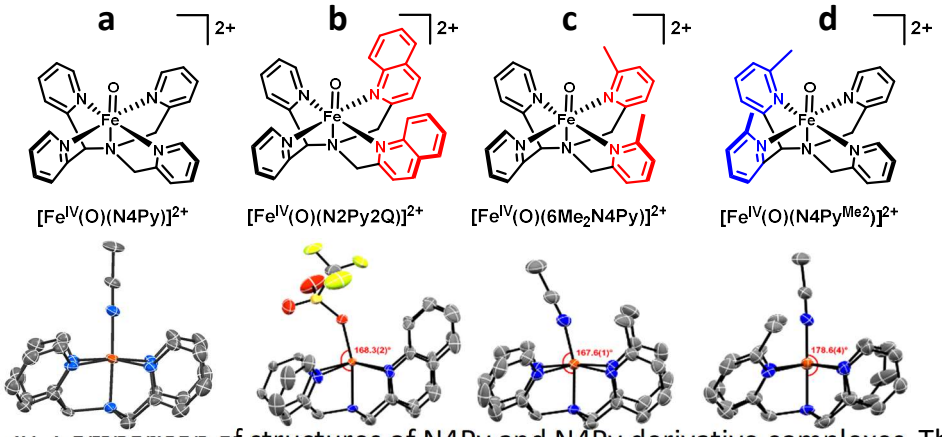

Figure 29. Comparison of structures of N4Py and N4Py derivative complexes. The second crystal structure is of the Fe^{II} starting material. Complexes **c** and **d** are DFT optimized structures. Ref: **a**[2]; **b**[3]; **c**[5], **d**[5]

This tilt has important implications on the lifetime of the complexes and their C-H bond cleavage reactivity. The two complexes that have substitutions on the *methylene* half of the N4Py ligand are significantly higher in HAT reactivity than the parent N4Py complex and reasonably more reactive than the corresponding *methine* substitutions (Table 17). The $[Fe^{IV}(O)(6Me_2N4Py)]^{2+}$ complex is 1000 times more reactive towards cyclohexane than the parent complex. This increased reactivity is also equivalent to the quinoline substitutions, supporting the hypothesis that the steric-imposed tilt can lead to increased reactivity. In further support of this hypothesis, the complex **d** is only one order of magnitude more reactive towards cyclohexane than complex **a**. It is clear that the tilting of the oxoiron(IV) unit increases reactivity. Interestingly, there are stark differences between the $t_{1/2}$ values. While we have found that complex **c** is the least thermally stable (0.5 h @ 25 °C), the complexes **b** and **d** are not very different, only being approximately 5 and 4 times more thermally stable, respectively. The most interesting comparison is found when looking at complex **c** and **d**, arguably "partners" in substitution to understand the impact of 6-methyl substitutions. While the HAT reactivity towards cyclohexane is 2 orders of magnitude greater for **c** when compared to **d**, the thermal stability is only a factor of 4 larger for **d** than **c**. We hypothesize that addition of the methyl positions in the 6^{th} position of the pyridines leads to an intramolecular hydroxylation that is responsible for the decrease in stability. Efforts have been made towards the crystallization of complex **c** but have been unsuccessful. It is likely that deuteration of the methyl positions may increase the stability of this complex and, combined with the previously discussed

methodology for growing crystals, may prove to be useful in obtaining high-quality crystals of the $[Fe^{IV}(O)(6Me_2N4Py)]^{2+}$ and $[Fe^{IV}(O)(N4Py^{Me2})]^{2+}$ complexes.

Table 17. Comparison of the structure, reactivity and thermal stability of the four N4Py and N4Py-derivative complexes.

		a[i]	b[ii]	c	d[iii]
$\angle N_{axial}$-Fe-O (°)		178.6	170.5	167.6	178.6
self-decay @ 25 °C (hr)	-	60	2.5	0.5	2
Substrate	BDE_{C-H} (kcal/mol)	k_2 (x 10^{-3} M^{-1} s^{-1})			
Cumene	84.5	2	160	130	
Ethylbenzene	87	4	100	100	
Toluene	90	0.063	12	19	3.5
Cyclohexane	99.3	0.055	29	25	0.67

i – Ref [2, 53]
ii – Ref [3]
iii – Ref [160]

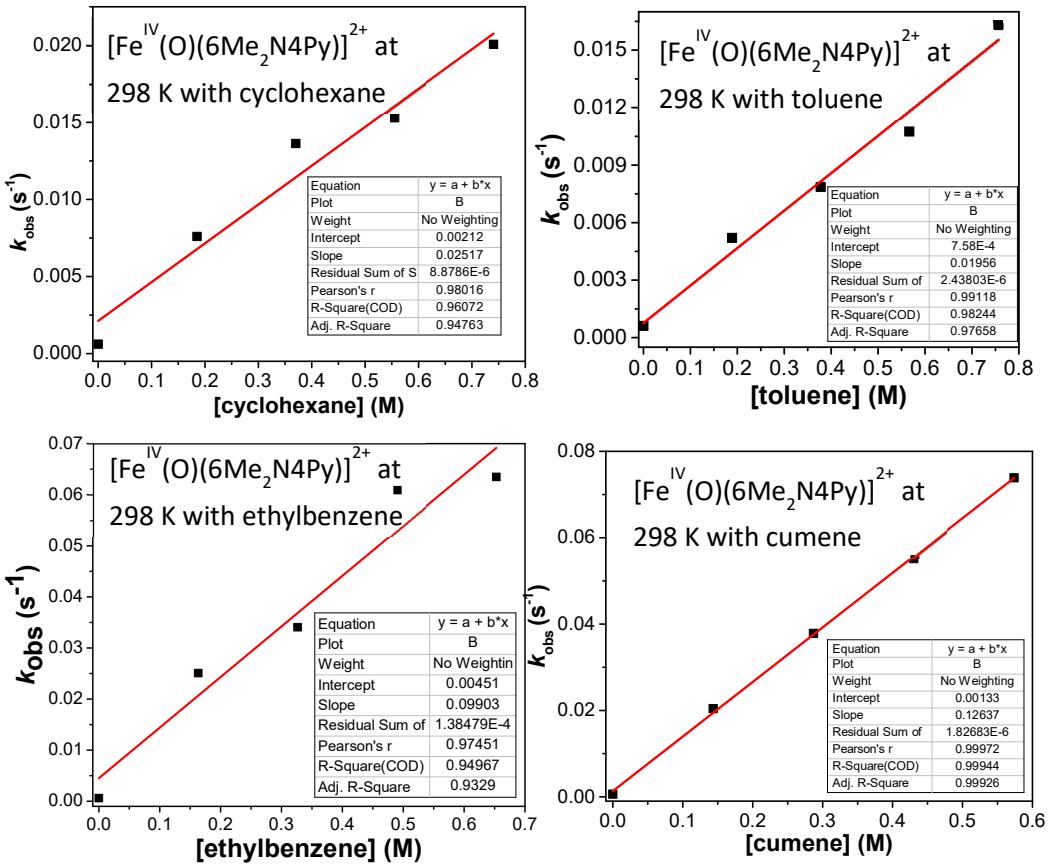

Figure 30. k_2 plots for the anaerobic oxidation of different HAT substrates performed by $[Fe^{IV}(O)(6Me_2N4Py)]^{2+}$. The slopes of the fitted red lines represent the second-order rate constants (k_2 M^{-1} s^{-1}) at 298 K in acetonitrile.

4.5 — Conclusion

Many efforts have been undertaken in an attempt to correlate structure, spectroscopy, and reactivity to better understand non-heme iron enzymes that utilize high-valent oxoiron intermediates to perform powerful oxidations. This work has spanned a wide variety of monoiron complexes. The high-valent oxoiron(IV) crystal structures ($[Fe^{IV}(O)(5Me_2\text{-}N4Py)]^{2+}$, preliminary $[Fe^{IV}(O)(TMC\text{-}im)]^{2+}$) provide structural information,

gaining insight into the iron-oxo bond length as well as the ligand structure. These are complemented by iron(II) complexes ($[Fe^{II}(TMC\text{-}im)]^{2+}$, $[Fe^{II}(Bn3MC)(OTf)]^{+}$, $[Fe^{II}(TMC)(Cl)]^{+}$) where the iron(IV) crystal structures were unobtainable due to the thermal instability of these higher reactivity complexes. In lieu of crystallographic characterization of these high-valent complexes, XAS data has been collected, providing important structural information such as the iron-oxo bond length, the iron-ligand bond lengths, and the centrosymmetry of the iron center alongside insight into the oxidation state of the iron. These structural and spectroscopic characterization can be compared to the reactivity data that we have obtained, providing a relationship between the structure, spectroscopy, and reactivity of these highly reactive species. As more complexes are characterized in any or all of these three characteristics, a better understanding of how nature modulates the first coordination sphere around the active site to control reactivity and unleash powerful oxidants.

4.6 — Additional X-ray Diffraction Data

Fe(II)(TMC-im)

Data collection

A crystal (approximate dimensions 0.200 x 0.200 x 0.100 mm was placed onto the tip of a 0.5 mm MiTeGen loop and mounted on a Bruker Photon-III CPAD diffractometer for a data collection at 125(2) K.[161] A preliminary set of cell constants was calculated from reflections harvested from two sets of 12 frames. These initial sets of frames were oriented such that orthogonal wedges of reciprocal space were surveyed. This produced initial orientation matrices determined from 150 reflections. The data collection was carried out using MoKα radiation (graphite monochromator) with a frame time of 10 seconds and a detector distance of 7.0 cm. A randomly oriented region of reciprocal space was surveyed to the extent of one sphere and to a resolution of 0.71 Å. Four major sections of frames were collected with 0.30º steps in ω or ϕ. The intensity data were corrected for absorption and decay.[161] Final cell constants were calculated from the xyz centroids of 5921 strong reflections from the actual data collection after integration.[161] Please refer to Table 18 for additional crystal and refinement information.

Structure solution and refinement

The structure was solved using SHELXT 2014/5 (Sheldrick, 2014)[162] and refined using SHELXL-2018/1 (Sheldrick, 2018)[163]. The space group $P2_1/n$ was determined based on systematic absences and intensity statistics. A direct-methods solution was calculated

which provided most non-hydrogen atoms from the E-map. Full-matrix least squares / difference Fourier cycles were performed which located the remaining non-hydrogen atoms. All non-hydrogen atoms were refined with anisotropic displacement parameters. All hydrogen atoms were placed in ideal positions and refined as riding atoms with relative isotropic displacement parameters. The final full matrix least squares refinement converged to $R1 = 0.0519$ and $wR2 = 0.1353$ (F^2, all data).

Table 18. Crystal data and structure refinement for $[Fe^{II}(TMC\text{-}Im)]^{2+}$.

Identification code	CCDC 1984621	
Empirical formula	$C_{20}\ H_{36}\ F_6\ Fe\ N_6\ O_6\ S_2$	
Formula weight	690.52	
Temperature	125(2) K	
Wavelength	0.71073 Å	
Crystal system	Monoclinic	
Space group	$P2_1/n$	
Unit cell dimensions	a = 19.4830(14) Å	α = 90°
	b = 13.9247(10) Å	β = 110.689(2)°
	c = 22.7840(18) Å	γ = 90°
Volume	5782.6(7) $Å^3$	
Z	8	
Density (calculated)	1.586 Mg/m^3	
Absorption coefficient	0.751 mm^{-1}	
F(000)	2864	
Crystal color, morphology	colourless, block	
Crystal size	0.200 x 0.200 x 0.100 mm^3	
Theta range for data collection	2.235 to 27.133°	
Index ranges	$-24 \le h \le 24$, $-17 \le k \le 17$, $-28 \le l \le 29$	
Reflections collected	90337	
Independent reflections	12778 [R(int) = 0.1083]	
Observed reflections	7169	
Completeness to theta = 25.242°	99.9%	
Absorption correction	Semi-empirical from equivalents	
Refinement method	Full-matrix least-squares on F^2	
Data / restraints / parameters	12778 / 0 / 747	
Goodness-of-fit on F^2	1.014	
Final R indices [I>2sigma(I)]	$R1$ = 0.0519, $wR2$ = 0.1078	
R indices (all data)	$R1$ = 0.1114, $wR2$ = 0.1353	
Extinction coefficient	n/a	
Largest diff. peak and hole	0.623 and -0.445 $e.Å^{-3}$	

Some equations of interest:

$$R_{int} = \Sigma\ |F_o^2 - < F_o^2 >| \ / \ \Sigma |F_o^2|$$

$$R_1 = \Sigma ||F_o| - |F_c|| \ / \ \Sigma |F_o|$$

$$wR2 = [\Sigma [w(F_o^2 - F_c^2)^2] \ / \ \Sigma\ [w(F_o^2)^2]]^{1/2}$$

where $w = q \ / \ [\sigma^2 (F_o^2) + (a*P)^2 + b*P + d + e*\sin(\theta)]$

$$\text{GooF} = S = [\Sigma [w(F_o^2 - F_c^2)^2] \ / \ (n-p)]^{1/2}$$

Table 19. Atomic coordinates (x 10^4) and equivalent isotropic displacement parameters ($Å^2$x 10^3) for $[Fe^{II}(TMC\text{-}Im)]^{2+}$. U_{eq} is defined as one third of the trace of the orthogonalized U_{ij} tensor.

	x	y	z	U_{eq}
N1	1867(2)	8571(2)	2864(2)	38(1)
C1	1380(3)	8206(3)	2244(2)	48(1)
S1	1338(1)	4722(1)	3231(1)	28(1)
O1	1945(2)	4078(2)	3341(2)	45(1)
F1	983(1)	5831(2)	4012(1)	57(1)
Fe1	1523(1)	9971(1)	3093(1)	20(1)
N2	1219(2)	10469(2)	2151(1)	23(1)
S2	4210(1)	7963(1)	4593(1)	30(1)
O2	1338(2)	5537(2)	2845(1)	44(1)
F2	2133(1)	5776(2)	4177(1)	55(1)
C2	1307(2)	8842(3)	1695(2)	37(1)
N3	998(2)	11314(2)	3271(2)	27(1)
C3	864(2)	9743(3)	1655(2)	30(1)
O3	642(1)	4259(2)	3091(1)	39(1)
F3	1610(2)	4591(2)	4438(1)	61(1)
N4	1127(2)	9154(3)	3693(2)	46(1)
C4	675(2)	11254(3)	2106(2)	31(1)
O4	3584(1)	8210(2)	4756(1)	41(1)
F4	3923(2)	6140(2)	4674(1)	57(1)
N5	2425(2)	10788(2)	3614(1)	23(1)
C5	917(2)	11870(3)	2694(2)	37(1)
O5	4861(1)	8514(2)	4905(1)	44(1)
F5	4602(1)	6775(2)	5548(1)	54(1)
N6	2889(2)	11998(2)	4246(1)	27(1)
C6	265(2)	11180(4)	3341(2)	48(1)
O6	4062(2)	7808(2)	3937(1)	41(1)
F6	5050(2)	6441(2)	4831(1)	69(1)
C7	244(3)	10401(4)	3796(2)	58(2)
C8	374(3)	9382(4)	3629(2)	64(2)

C9	1157(3)	8105(3)	3501(2)	60(2)
C10	1840(3)	7916(3)	3358(3)	66(2)
C11	2647(2)	8594(3)	2889(2)	55(1)
C12	1866(2)	10887(3)	2041(2)	34(1)
C13	1505(2)	11829(3)	3817(2)	31(1)
C14	1623(3)	9280(4)	4361(2)	64(2)
C15	2273(2)	11548(2)	3889(2)	22(1)
C16	3181(2)	10759(3)	3801(2)	34(1)
C17	3469(2)	11498(3)	4190(2)	32(1)
C18	2936(2)	12847(3)	4636(2)	43(1)
C19	1522(2)	5251(3)	4002(2)	37(1)
C20	4453(2)	6777(3)	4928(2)	41(1)
Fe1'	3583(1)	-14(1)	6899(1)	21(1)
N1'	3393(2)	1492(2)	7044(2)	38(1)
C1'	3640(3)	2014(3)	6557(2)	54(1)
S1'	824(1)	1944(1)	5418(1)	30(1)
O1'	157(2)	1452(2)	5066(1)	52(1)
F1'	47(2)	3516(2)	5266(1)	68(1)
N2'	4172(2)	525(2)	6327(2)	33(1)
C2'	4315(3)	1556(3)	6496(2)	49(1)
S2'	3661(1)	5263(1)	6840(1)	25(1)
O2'	972(1)	2012(2)	6081(1)	38(1)
F2'	1182(2)	3761(2)	5418(1)	59(1)
N3'	3975(2)	-1498(2)	6814(1)	25(1)
O3'	1450(2)	1703(2)	5249(1)	43(1)
F3'	464(2)	3232(2)	4524(1)	61(1)
C3'	4903(2)	59(3)	6439(2)	45(1)
N4'	3740(2)	-422(2)	7842(1)	22(1)
O4'	3687(1)	4392(2)	7187(1)	35(1)
F4'	2815(1)	4326(2)	5855(1)	52(1)
C4'	4894(2)	-1000(3)	6334(2)	44(1)
N5'	2615(2)	-696(2)	6366(1)	25(1)
O5'	3060(1)	5898(2)	6796(1)	34(1)
F5'	3333(1)	5562(2)	5637(1)	52(1)

C5'	4732(2)	-1612(3)	6818(2)	40(1)
N6'	2052(2)	-1953(2)	5828(1)	25(1)
O6'	4357(1)	5738(2)	6972(1)	34(1)
F6'	3954(1)	4272(2)	5976(1)	50(1)
C6'	3946(2)	-1971(3)	7398(2)	33(1)
C7'	4211(2)	-1288(3)	7957(2)	32(1)
C8'	4108(2)	306(3)	8331(2)	31(1)
C9'	3767(2)	1297(3)	8221(2)	36(1)
C10'	3861(2)	1842(3)	7677(2)	42(1)
C11'	2622(2)	1719(3)	6921(2)	56(1)
C12'	3704(3)	450(3)	5654(2)	48(1)
C13'	3440(2)	-1979(3)	6263(2)	28(1)
C14'	3025(2)	-683(3)	7893(2)	34(1)
C15'	2705(2)	-1550(2)	6148(2)	21(1)
C16'	1864(2)	-551(3)	6170(2)	33(1)
C17'	1513(2)	-1320(3)	5837(2)	31(1)
C18'	1935(2)	-2876(3)	5503(2)	36(1)
C19'	625(2)	3172(3)	5146(2)	41(1)
C20'	3428(2)	4838(3)	6035(2)	34(1)

Table 20. Bond lengths [Å] and angles [°] for $[Fe^{II}(TMC\text{-}Im)]^{2+}$.

N(1)-C(10)	1.464(6)	F(3)-C(19)	1.319(5)
N(1)-C(1)	1.485(5)	N(4)-C(8)	1.457(6)
N(1)-C(11)	1.502(6)	N(4)-C(14)	1.498(5)
N(1)-Fe(1)	2.183(3)	N(4)-C(9)	1.532(6)
C(1)-C(2)	1.499(6)	C(4)-C(5)	1.519(5)
C(1)-H(1A)	0.9900	C(4)-H(4A)	0.9900
C(1)-H(1AB)	0.9900	C(4)-H(4AB)	0.9900
S(1)-O(3)	1.431(3)	F(4)-C(20)	1.330(5)
S(1)-O(1)	1.434(3)	N(5)-C(15)	1.316(4)
S(1)-O(2)	1.437(3)	N(5)-C(16)	1.382(4)
S(1)-C(19)	1.821(4)	C(5)-H(5A)	0.9900
F(1)-C(19)	1.331(5)	C(5)-H(5AB)	0.9900
Fe(1)-N(5)	2.077(3)	F(5)-C(20)	1.337(5)
Fe(1)-N(4)	2.122(3)	N(6)-C(15)	1.344(4)
Fe(1)-N(2)	2.131(3)	N(6)-C(17)	1.373(5)
Fe(1)-N(3)	2.237(3)	N(6)-C(18)	1.461(5)
N(2)-C(12)	1.489(4)	C(6)-C(7)	1.510(7)
N(2)-C(3)	1.491(4)	C(6)-H(6A)	0.9900
N(2)-C(4)	1.500(4)	C(6)-H(6AB)	0.9900
S(2)-O(6)	1.435(3)	F(6)-C(20)	1.343(5)
S(2)-O(5)	1.437(3)	C(7)-C(8)	1.514(7)
S(2)-O(4)	1.438(3)	C(7)-H(7A)	0.9900
S(2)-C(20)	1.810(5)	C(7)-H(7AB)	0.9900
F(2)-C(19)	1.331(4)	C(8)-H(8A)	0.9900
C(2)-C(3)	1.507(5)	C(8)-H(8AB)	0.9900
C(2)-H(2A)	0.9900	C(9)-C(10)	1.501(7)
C(2)-H(2AB)	0.9900	C(9)-H(9A)	0.9900
N(3)-C(13)	1.474(4)	C(9)-H(9AB)	0.9900
N(3)-C(5)	1.486(5)	C(10)-H(10C)	0.9900
N(3)-C(6)	1.502(5)	C(10)-H(10D)	0.9900
C(3)-H(3A)	0.9900	C(11)-H(11A)	0.9800
C(3)-H(3AB)	0.9900	C(11)-H(11B)	0.9800

C(11)-H(11C)	0.9800	C(2')-H(2'B)	0.9900
C(12)-H(12A)	0.9800	S(2')-O(4')	1.439(3)
C(12)-H(12B)	0.9800	S(2')-O(6')	1.441(2)
C(12)-H(12C)	0.9800	S(2')-O(5')	1.443(2)
C(13)-C(15)	1.498(5)	S(2')-C(20')	1.825(4)
C(13)-H(13A)	0.9900	F(2')-C(19')	1.326(5)
C(13)-H(13B)	0.9900	N(3')-C(13')	1.479(4)
C(14)-H(14A)	0.9800	N(3')-C(5')	1.479(5)
C(14)-H(14B)	0.9800	N(3')-C(6')	1.502(5)
C(14)-H(14C)	0.9800	F(3')-C(19')	1.341(5)
C(16)-C(17)	1.344(5)	C(3')-C(4')	1.493(6)
C(16)-H(16)	0.9500	C(3')-H(3'A)	0.9900
C(17)-H(17)	0.9500	C(3')-H(3'B)	0.9900
C(18)-H(18A)	0.9800	N(4')-C(7')	1.482(4)
C(18)-H(18B)	0.9800	N(4')-C(14')	1.484(4)
C(18)-H(18C)	0.9800	N(4')-C(8')	1.491(4)
Fe(1')-N(5')	2.077(3)	F(4')-C(20')	1.327(4)
Fe(1')-N(4')	2.136(3)	C(4')-C(5')	1.512(6)
Fe(1')-N(2')	2.154(3)	C(4')-H(4'A)	0.9900
Fe(1')-N(1')	2.175(3)	C(4')-H(4'B)	0.9900
Fe(1')-N(3')	2.236(3)	N(5')-C(15')	1.324(4)
N(1')-C(11')	1.462(5)	N(5')-C(16')	1.386(4)
N(1')-C(10')	1.489(5)	F(5')-C(20')	1.325(4)
N(1')-C(1')	1.539(6)	C(5')-H(5'A)	0.9900
C(1')-C(2')	1.512(7)	C(5')-H(5'B)	0.9900
C(1')-H(1'A)	0.9900	N(6')-C(15')	1.344(4)
C(1')-H(1'B)	0.9900	N(6')-C(17')	1.377(5)
S(1')-O(2')	1.436(3)	N(6')-C(18')	1.460(5)
S(1')-O(1')	1.437(3)	F(6')-C(20')	1.337(4)
S(1')-O(3')	1.443(3)	C(6')-C(7')	1.527(5)
S(1')-C(19')	1.814(5)	C(6')-H(6'A)	0.9900
F(1')-C(19')	1.338(5)	C(6')-H(6'B)	0.9900
N(2')-C(12')	1.485(5)	C(7')-H(7'A)	0.9900
N(2')-C(2')	1.487(5)	C(7')-H(7'B)	0.9900
N(2')-C(3')	1.502(5)	C(8')-C(9')	1.513(5)
C(2')-H(2'A)	0.9900	C(8')-H(8'A)	0.9900

C(8')-H(8'B)	0.9900	O(3)-S(1)-O(1)	114.52(17)
C(9')-C(10')	1.519(6)	O(3)-S(1)-O(2)	115.12(18)
C(9')-H(9'A)	0.9900	O(1)-S(1)-O(2)	114.98(18)
C(9')-H(9'B)	0.9900	O(3)-S(1)-C(19)	104.22(18)
C(10')-H(10A)	0.9900	O(1)-S(1)-C(19)	102.44(19)
C(10')-H(10B)	0.9900	O(2)-S(1)-C(19)	103.23(19)
C(11')-H(11D)	0.9800	N(5)-Fe(1)-N(4)	110.62(13)
C(11')-H(11E)	0.9800	N(5)-Fe(1)-N(2)	106.01(11)
C(11')-H(11F)	0.9800	N(4)-Fe(1)-N(2)	141.99(13)
C(12')-H(12D)	0.9800	N(5)-Fe(1)-N(1)	110.89(12)
C(12')-H(12E)	0.9800	N(4)-Fe(1)-N(1)	83.54(15)
C(12')-H(12F)	0.9800	N(2)-Fe(1)-N(1)	92.82(12)
C(13')-C(15')	1.487(5)	N(5)-Fe(1)-N(3)	77.75(11)
C(13')-H(13C)	0.9900	N(4)-Fe(1)-N(3)	92.14(14)
C(13')-H(13D)	0.9900	N(2)-Fe(1)-N(3)	85.88(12)
C(14')-H(14D)	0.9800	N(1)-Fe(1)-N(3)	171.24(12)
C(14')-H(14E)	0.9800	C(12)-N(2)-C(3)	109.4(3)
C(14')-H(14F)	0.9800	C(12)-N(2)-C(4)	108.8(3)
C(16')-C(17')	1.351(5)	C(3)-N(2)-C(4)	108.4(3)
C(16')-H(16')	0.9500	C(12)-N(2)-Fe(1)	110.2(2)
C(17')-H(17')	0.9500	C(3)-N(2)-Fe(1)	115.6(2)
C(18')-H(18D)	0.9800	C(4)-N(2)-Fe(1)	104.1(2)
C(18')-H(18E)	0.9800	O(6)-S(2)-O(5)	114.40(18)
C(18')-H(18F)	0.9800	O(6)-S(2)-O(4)	115.45(17)
C(10)-N(1)-C(1)	109.5(4)	O(5)-S(2)-O(4)	115.10(18)
C(10)-N(1)-C(11)	107.1(4)	O(6)-S(2)-C(20)	103.23(19)
C(1)-N(1)-C(11)	110.0(4)	O(5)-S(2)-C(20)	103.02(19)
C(10)-N(1)-Fe(1)	105.9(3)	O(4)-S(2)-C(20)	103.21(19)
C(1)-N(1)-Fe(1)	112.8(2)	C(1)-C(2)-C(3)	115.1(4)
C(11)-N(1)-Fe(1)	111.3(2)	C(1)-C(2)-H(2A)	108.5
N(1)-C(1)-C(2)	115.6(4)	C(3)-C(2)-H(2A)	108.5
N(1)-C(1)-H(1A)	108.4	C(1)-C(2)-H(2AB)	108.5
C(2)-C(1)-H(1A)	108.4	C(3)-C(2)-H(2AB)	108.5
N(1)-C(1)-H(1AB)	108.4	H(2A)-C(2)-H(2AB)	107.5
C(2)-C(1)-H(1AB)	108.4	C(13)-N(3)-C(5)	108.8(3)
H(1A)-C(1)-H(1AB)	107.4	C(13)-N(3)-C(6)	110.5(3)

C(5)-N(3)-C(6)	110.6(3)	C(7)-C(6)-H(6A)	108.6
C(13)-N(3)-Fe(1)	110.3(2)	N(3)-C(6)-H(6AB)	108.6
C(5)-N(3)-Fe(1)	100.8(2)	C(7)-C(6)-H(6AB)	108.6
C(6)-N(3)-Fe(1)	115.3(3)	H(6A)-C(6)-H(6AB)	107.5
N(2)-C(3)-C(2)	114.6(3)	C(6)-C(7)-C(8)	117.0(4)
N(2)-C(3)-H(3A)	108.6	C(6)-C(7)-H(7A)	108.0
C(2)-C(3)-H(3A)	108.6	C(8)-C(7)-H(7A)	108.0
N(2)-C(3)-H(3AB)	108.6	C(6)-C(7)-H(7AB)	108.0
C(2)-C(3)-H(3AB)	108.6	C(8)-C(7)-H(7AB)	108.1
H(3A)-C(3)-H(3AB)	107.6	H(7A)-C(7)-H(7AB)	107.3
C(8)-N(4)-C(14)	110.0(4)	N(4)-C(8)-C(7)	115.5(4)
C(8)-N(4)-C(9)	108.5(4)	N(4)-C(8)-H(8A)	108.4
C(14)-N(4)-C(9)	108.9(4)	C(7)-C(8)-H(8A)	108.4
C(8)-N(4)-Fe(1)	113.7(3)	N(4)-C(8)-H(8AB)	108.4
C(14)-N(4)-Fe(1)	109.9(3)	C(7)-C(8)-H(8AB)	108.4
C(9)-N(4)-Fe(1)	105.6(3)	H(8A)-C(8)-H(8AB)	107.5
N(2)-C(4)-C(5)	111.1(3)	C(10)-C(9)-N(4)	110.8(4)
N(2)-C(4)-H(4A)	109.4	C(10)-C(9)-H(9A)	109.5
C(5)-C(4)-H(4A)	109.4	N(4)-C(9)-H(9A)	109.5
N(2)-C(4)-H(4AB)	109.4	C(10)-C(9)-H(9AB)	109.5
C(5)-C(4)-H(4AB)	109.4	N(4)-C(9)-H(9AB)	109.5
H(4A)-C(4)-H(4AB)	108.0	H(9A)-C(9)-H(9AB)	108.1
C(15)-N(5)-C(16)	105.7(3)	N(1)-C(10)-C(9)	109.5(4)
C(15)-N(5)-Fe(1)	115.1(2)	N(1)-C(10)-H(10C)	109.8
C(16)-N(5)-Fe(1)	139.0(3)	C(9)-C(10)-H(10C)	109.8
N(3)-C(5)-C(4)	112.9(3)	N(1)-C(10)-H(10D)	109.8
N(3)-C(5)-H(5A)	109.0	C(9)-C(10)-H(10D)	109.8
C(4)-C(5)-H(5A)	109.0	H(10C)-C(10)-H(10D)	108.2
N(3)-C(5)-H(5AB)	109.0	N(1)-C(11)-H(11A)	109.5
C(4)-C(5)-H(5AB)	109.0	N(1)-C(11)-H(11B)	109.5
H(5A)-C(5)-H(5AB)	107.8	H(11A)-C(11)-H(11B)	109.5
C(15)-N(6)-C(17)	107.2(3)	N(1)-C(11)-H(11C)	109.5
C(15)-N(6)-C(18)	126.6(3)	H(11A)-C(11)-H(11C)	109.5
C(17)-N(6)-C(18)	126.2(3)	H(11B)-C(11)-H(11C)	109.5
N(3)-C(6)-C(7)	114.8(4)	N(2)-C(12)-H(12A)	109.5
N(3)-C(6)-H(6A)	108.6	N(2)-C(12)-H(12B)	109.5

H(12A)-C(12)-H(12B)	109.5	F(1)-C(19)-S(1)	111.9(3)
N(2)-C(12)-H(12C)	109.5	F(4)-C(20)-F(5)	107.6(4)
H(12A)-C(12)-H(12C)	109.5	F(4)-C(20)-F(6)	106.3(4)
H(12B)-C(12)-H(12C)	109.5	F(5)-C(20)-F(6)	107.2(3)
N(3)-C(13)-C(15)	108.1(3)	F(4)-C(20)-S(2)	112.2(3)
N(3)-C(13)-H(13A)	110.1	F(5)-C(20)-S(2)	112.0(3)
C(15)-C(13)-H(13A)	110.1	F(6)-C(20)-S(2)	111.2(3)
N(3)-C(13)-H(13B)	110.1	N(5')-Fe(1')-N(4')	104.13(11)
C(15)-C(13)-H(13B)	110.1	N(5')-Fe(1')-N(2')	111.90(12)
H(13A)-C(13)-H(13B)	108.4	N(4')-Fe(1')-N(2')	141.60(11)
N(4)-C(14)-H(14A)	109.5	N(5')-Fe(1')-N(1')	111.22(12)
N(4)-C(14)-H(14B)	109.5	N(4')-Fe(1')-N(1')	94.32(13)
H(14A)-C(14)-H(14B)	109.5	N(2')-Fe(1')-N(1')	84.94(13)
N(4)-C(14)-H(14C)	109.5	N(5')-Fe(1')-N(3')	78.12(11)
H(14A)-C(14)-H(14C)	109.5	N(4')-Fe(1')-N(3')	84.78(11)
H(14B)-C(14)-H(14C)	109.5	N(2')-Fe(1')-N(3')	89.88(12)
N(5)-C(15)-N(6)	111.2(3)	N(1')-Fe(1')-N(3')	170.49(12)
N(5)-C(15)-C(13)	122.9(3)	C(11')-N(1')-C(10')	110.6(4)
N(6)-C(15)-C(13)	125.9(3)	C(11')-N(1')-C(1')	108.7(4)
C(17)-C(16)-N(5)	109.5(3)	C(10')-N(1')-C(1')	107.6(3)
C(17)-C(16)-H(16)	125.3	C(11')-N(1')-Fe(1')	113.4(3)
N(5)-C(16)-H(16)	125.3	C(10')-N(1')-Fe(1')	112.6(2)
C(16)-C(17)-N(6)	106.5(3)	C(1')-N(1')-Fe(1')	103.5(3)
C(16)-C(17)-H(17)	126.8	C(2')-C(1')-N(1')	111.8(3)
N(6)-C(17)-H(17)	126.8	C(2')-C(1')-H(1'A)	109.3
N(6)-C(18)-H(18A)	109.5	N(1')-C(1')-H(1'A)	109.3
N(6)-C(18)-H(18B)	109.5	C(2')-C(1')-H(1'B)	109.3
H(18A)-C(18)-H(18B)	109.5	N(1')-C(1')-H(1'B)	109.3
N(6)-C(18)-H(18C)	109.5	H(1'A)-C(1')-H(1'B)	107.9
H(18A)-C(18)-H(18C)	109.5	O(2')-S(1')-O(1')	115.08(18)
H(18B)-C(18)-H(18C)	109.5	O(2')-S(1')-O(3')	114.95(17)
F(3)-C(19)-F(2)	107.0(3)	O(1')-S(1')-O(3')	114.99(19)
F(3)-C(19)-F(1)	107.7(4)	O(2')-S(1')-C(19')	103.75(19)
F(2)-C(19)-F(1)	106.8(3)	O(1')-S(1')-C(19')	102.5(2)
F(3)-C(19)-S(1)	111.9(3)	O(3')-S(1')-C(19')	103.1(2)
F(2)-C(19)-S(1)	111.2(3)	C(12')-N(2')-C(2')	109.0(3)

C(12')-N(2')-C(3')	110.1(3)	C(3')-C(4')-H(4'A)	108.3
C(2')-N(2')-C(3')	107.1(3)	C(5')-C(4')-H(4'A)	108.3
C(12')-N(2')-Fe(1')	109.6(2)	C(3')-C(4')-H(4'B)	108.3
C(2')-N(2')-Fe(1')	105.7(3)	C(5')-C(4')-H(4'B)	108.3
C(3')-N(2')-Fe(1')	115.0(2)	H(4'A)-C(4')-H(4'B)	107.4
N(2')-C(2')-C(1')	110.0(4)	C(15')-N(5')-C(16')	105.9(3)
N(2')-C(2')-H(2'A)	109.7	C(15')-N(5')-Fe(1')	114.7(2)
C(1')-C(2')-H(2'A)	109.7	C(16')-N(5')-Fe(1')	139.4(3)
N(2')-C(2')-H(2'B)	109.7	N(3')-C(5')-C(4')	113.6(4)
C(1')-C(2')-H(2'B)	109.7	N(3')-C(5')-H(5'A)	108.9
H(2'A)-C(2')-H(2'B)	108.2	C(4')-C(5')-H(5'A)	108.9
O(4')-S(2')-O(6')	115.11(16)	N(3')-C(5')-H(5'B)	108.9
O(4')-S(2')-O(5')	115.14(16)	C(4')-C(5')-H(5'B)	108.9
O(6')-S(2')-O(5')	114.42(15)	H(5'A)-C(5')-H(5'B)	107.7
O(4')-S(2')-C(20')	103.09(18)	C(15')-N(6')-C(17')	107.8(3)
O(6')-S(2')-C(20')	103.93(17)	C(15')-N(6')-C(18')	126.2(3)
O(5')-S(2')-C(20')	102.81(17)	C(17')-N(6')-C(18')	126.0(3)
C(13')-N(3')-C(5')	111.0(3)	N(3')-C(6')-C(7')	111.0(3)
C(13')-N(3')-C(6')	108.5(3)	N(3')-C(6')-H(6'A)	109.4
C(5')-N(3')-C(6')	107.3(3)	C(7')-C(6')-H(6'A)	109.4
C(13')-N(3')-Fe(1')	109.4(2)	N(3')-C(6')-H(6'B)	109.4
C(5')-N(3')-Fe(1')	118.0(2)	C(7')-C(6')-H(6'B)	109.4
C(6')-N(3')-Fe(1')	102.0(2)	H(6'A)-C(6')-H(6'B)	108.0
C(4')-C(3')-N(2')	116.3(3)	N(4')-C(7')-C(6')	110.6(3)
C(4')-C(3')-H(3'A)	108.2	N(4')-C(7')-H(7'A)	109.5
N(2')-C(3')-H(3'A)	108.2	C(6')-C(7')-H(7'A)	109.5
C(4')-C(3')-H(3'B)	108.2	N(4')-C(7')-H(7'B)	109.5
N(2')-C(3')-H(3'B)	108.2	C(6')-C(7')-H(7'B)	109.5
H(3'A)-C(3')-H(3'B)	107.4	H(7'A)-C(7')-H(7'B)	108.1
C(7')-N(4')-C(14')	109.1(3)	N(4')-C(8')-C(9')	115.4(3)
C(7')-N(4')-C(8')	108.4(3)	N(4')-C(8')-H(8'A)	108.4
C(14')-N(4')-C(8')	109.0(3)	C(9')-C(8')-H(8'A)	108.4
C(7')-N(4')-Fe(1')	104.8(2)	N(4')-C(8')-H(8'B)	108.4
C(14')-N(4')-Fe(1')	109.9(2)	C(9')-C(8')-H(8'B)	108.4
C(8')-N(4')-Fe(1')	115.5(2)	H(8'A)-C(8')-H(8'B)	107.5
C(3')-C(4')-C(5')	115.7(4)	C(8')-C(9')-C(10')	114.7(3)

C(8')-C(9')-H(9'A)	108.6	H(14D)-C(14')-H(14E)	109.5
C(10')-C(9')-H(9'A)	108.6	N(4')-C(14')-H(14F)	109.5
C(8')-C(9')-H(9'B)	108.6	H(14D)-C(14')-H(14F)	109.5
C(10')-C(9')-H(9'B)	108.6	H(14E)-C(14')-H(14F)	109.5
H(9'A)-C(9')-H(9'B)	107.6	N(5')-C(15')-N(6')	110.7(3)
N(1')-C(10')-C(9')	114.6(3)	N(5')-C(15')-C(13')	122.7(3)
N(1')-C(10')-H(10A)	108.6	N(6')-C(15')-C(13')	126.6(3)
C(9')-C(10')-H(10A)	108.6	C(17')-C(16')-N(5')	109.5(3)
N(1')-C(10')-H(10B)	108.6	C(17')-C(16')-H(16')	125.3
C(9')-C(10')-H(10B)	108.6	N(5')-C(16')-H(16')	125.3
H(10A)-C(10')-H(10B)	107.6	C(16')-C(17')-N(6')	106.1(3)
N(1')-C(11')-H(11D)	109.5	C(16')-C(17')-H(17')	126.9
N(1')-C(11')-H(11E)	109.5	N(6')-C(17')-H(17')	126.9
H(11D)-C(11')-H(11E)	109.5	N(6')-C(18')-H(18D)	109.5
N(1')-C(11')-H(11F)	109.5	N(6')-C(18')-H(18E)	109.5
H(11D)-C(11')-H(11F)	109.5	H(18D)-C(18')-H(18E)	109.5
H(11E)-C(11')-H(11F)	109.5	N(6')-C(18')-H(18F)	109.5
N(2')-C(12')-H(12D)	109.5	H(18D)-C(18')-H(18F)	109.5
N(2')-C(12')-H(12E)	109.5	H(18E)-C(18')-H(18F)	109.5
H(12D)-C(12')-H(12E)	109.5	F(2')-C(19')-F(1')	107.0(4)
N(2')-C(12')-H(12F)	109.5	F(2')-C(19')-F(3')	107.6(4)
H(12D)-C(12')-H(12F)	109.5	F(1')-C(19')-F(3')	107.1(3)
H(12E)-C(12')-H(12F)	109.5	F(2')-C(19')-S(1')	112.4(3)
N(3')-C(13')-C(15')	108.4(3)	F(1')-C(19')-S(1')	111.1(3)
N(3')-C(13')-H(13C)	110.0	F(3')-C(19')-S(1')	111.3(3)
C(15')-C(13')-H(13C)	110.0	F(5')-C(20')-F(4')	107.6(3)
N(3')-C(13')-H(13D)	110.0	F(5')-C(20')-F(6')	107.9(3)
C(15')-C(13')-H(13D)	110.0	F(4')-C(20')-F(6')	106.9(3)
H(13C)-C(13')-H(13D)	108.4	F(5')-C(20')-S(2')	111.5(3)
N(4')-C(14')-H(14D)	109.5	F(4')-C(20')-S(2')	111.3(3)
N(4')-C(14')-H(14E)	109.5	F(6')-C(20')-S(2')	111.4(3)

Table 21. Anisotropic displacement parameters ($Å^2 x\ 10^3$) for $[Fe^{II}(TMC\text{-}Im)]^{2+}$. The anisotropic displacement factor exponent takes the form: $-2p^2[\ h^2\ a^{*2}U_{11} + ...\ + 2\ h\ k\ a^*\ b^*\ U_{12}\ ]$

	U_{11}	U_{22}	U_{33}	U_{23}	U_{13}	U_{12}
N1	52(2)	20(2)	35(2)	-2(2)	6(2)	1(2)
C1	59(3)	29(2)	46(3)	-13(2)	6(2)	3(2)
S1	21(1)	28(1)	36(1)	1(1)	11(1)	-1(1)
O1	31(2)	46(2)	61(2)	-1(2)	19(2)	15(1)
F1	51(2)	57(2)	58(2)	-24(1)	13(1)	8(1)
Fe1	23(1)	18(1)	19(1)	2(1)	5(1)	-3(1)
N2	21(2)	26(2)	22(2)	0(1)	9(1)	-5(1)
S2	23(1)	42(1)	21(1)	-6(1)	5(1)	-4(1)
O2	44(2)	46(2)	35(2)	10(1)	7(1)	-9(1)
F2	42(2)	62(2)	44(2)	-3(1)	-6(1)	-20(1)
C2	30(2)	43(3)	32(2)	-15(2)	4(2)	0(2)
N3	16(2)	36(2)	28(2)	-9(1)	5(1)	2(1)
C3	23(2)	44(2)	21(2)	-2(2)	7(2)	-3(2)
O3	27(2)	39(2)	56(2)	-15(1)	21(1)	-12(1)
F3	83(2)	60(2)	43(2)	16(1)	27(2)	1(2)
N4	59(3)	49(2)	33(2)	3(2)	18(2)	-26(2)
C4	28(2)	30(2)	29(2)	7(2)	3(2)	7(2)
O4	31(2)	52(2)	43(2)	-7(2)	16(1)	5(1)
F4	81(2)	45(2)	49(2)	-10(1)	27(2)	-19(2)
N5	19(2)	25(2)	22(2)	-3(1)	4(1)	1(1)
C5	37(2)	31(2)	36(3)	-2(2)	3(2)	8(2)
O5	34(2)	57(2)	34(2)	-7(2)	3(1)	-19(1)
F5	67(2)	59(2)	28(2)	5(1)	8(1)	5(1)
N6	23(2)	25(2)	26(2)	0(1)	0(1)	-5(1)
C6	19(2)	78(4)	45(3)	-29(3)	11(2)	1(2)
O6	38(2)	62(2)	20(2)	-5(1)	6(1)	-1(1)
F6	66(2)	72(2)	73(2)	4(2)	33(2)	31(2)
C7	37(3)	101(4)	46(3)	-15(3)	28(2)	-15(3)
C8	73(4)	89(4)	43(3)	-14(3)	35(3)	-42(3)
C9	101(4)	36(3)	40(3)	6(2)	23(3)	-23(3)

C10	101(5)	31(3)	61(4)	8(2)	22(3)	3(3)
C11	46(3)	49(3)	60(3)	-12(2)	5(2)	22(2)
C12	31(2)	43(2)	31(2)	0(2)	16(2)	-14(2)
C13	24(2)	34(2)	31(2)	-11(2)	6(2)	4(2)
C14	96(4)	63(3)	25(3)	10(2)	10(3)	-27(3)
C15	20(2)	23(2)	21(2)	0(2)	4(2)	-1(2)
C16	15(2)	48(3)	35(2)	-4(2)	5(2)	6(2)
C17	17(2)	48(3)	26(2)	5(2)	1(2)	-2(2)
C18	48(3)	29(2)	36(3)	-11(2)	-5(2)	-2(2)
C19	34(2)	37(2)	35(3)	4(2)	7(2)	-2(2)
C20	42(3)	48(3)	32(3)	-7(2)	12(2)	3(2)
Fe1'	24(1)	18(1)	22(1)	1(1)	9(1)	-1(1)
N1'	39(2)	23(2)	44(2)	-2(2)	3(2)	6(2)
C1'	86(4)	20(2)	46(3)	10(2)	12(3)	1(2)
S1'	24(1)	44(1)	23(1)	-9(1)	7(1)	-6(1)
O1'	40(2)	65(2)	43(2)	-17(2)	5(2)	-20(2)
F1'	57(2)	76(2)	73(2)	-3(2)	26(2)	28(2)
N2'	45(2)	32(2)	21(2)	0(1)	11(2)	-14(2)
C2'	77(3)	35(3)	37(3)	4(2)	24(3)	-23(2)
S2'	19(1)	22(1)	34(1)	0(1)	10(1)	2(1)
O2'	37(2)	55(2)	22(2)	-7(1)	12(1)	-6(1)
F2'	77(2)	54(2)	46(2)	-7(1)	21(2)	-24(2)
N3'	17(2)	27(2)	28(2)	-8(1)	6(1)	-1(1)
O3'	37(2)	64(2)	33(2)	-3(2)	18(1)	10(2)
F3'	76(2)	69(2)	30(2)	8(1)	9(1)	10(2)
C3'	36(2)	64(3)	42(3)	8(2)	21(2)	-8(2)
N4'	19(2)	23(2)	26(2)	0(1)	12(1)	-2(1)
O4'	33(2)	29(2)	39(2)	9(1)	8(1)	5(1)
F4'	36(1)	59(2)	51(2)	-11(1)	3(1)	-19(1)
C4'	31(2)	66(3)	39(3)	-17(2)	18(2)	-10(2)
N5'	17(2)	25(2)	30(2)	-1(1)	6(1)	4(1)
O5'	24(1)	30(2)	52(2)	6(1)	19(1)	8(1)
F5'	65(2)	53(2)	43(2)	16(1)	24(1)	8(1)
C5'	24(2)	49(3)	46(3)	-15(2)	11(2)	1(2)
N6'	21(2)	26(2)	24(2)	0(1)	5(1)	-1(1)
O6'	20(1)	36(2)	45(2)	-11(1)	13(1)	-5(1)

F6'	47(2)	54(2)	49(2)	-18(1)	17(1)	11(1)
C6'	33(2)	25(2)	37(2)	4(2)	9(2)	5(2)
C7'	32(2)	34(2)	27(2)	8(2)	9(2)	6(2)
C8'	38(2)	31(2)	29(2)	-6(2)	17(2)	-11(2)
C9'	35(2)	36(2)	42(3)	-13(2)	17(2)	-2(2)
C10'	46(3)	27(2)	49(3)	-10(2)	12(2)	-3(2)
C11'	43(3)	37(3)	73(4)	-18(2)	1(3)	15(2)
C12'	64(3)	51(3)	26(2)	5(2)	14(2)	-13(2)
C13'	21(2)	28(2)	28(2)	-8(2)	3(2)	2(2)
C14'	30(2)	39(2)	40(3)	-5(2)	23(2)	-10(2)
C15'	17(2)	24(2)	21(2)	2(2)	6(2)	-1(1)
C16'	22(2)	41(2)	35(2)	-3(2)	9(2)	9(2)
C17'	17(2)	45(3)	27(2)	2(2)	4(2)	3(2)
C18'	31(2)	34(2)	33(2)	-7(2)	-2(2)	-3(2)
C19'	36(2)	56(3)	28(2)	-1(2)	9(2)	2(2)
C20'	26(2)	33(2)	40(3)	4(2)	9(2)	2(2)

Table 22. Hydrogen coordinates (x 10^4) and isotropic displacement parameters (Å^2 x 10^3) for $[Fe^{II}(TMC\text{-}Im)]^{2+}$.

	x	y	z	U(eq)
H1A	885	8101	2262	58
H1AB	1568	7574	2171	58
H2A	1077	8467	1305	44
H2AB	1804	9027	1712	44
H3A	767	10042	1240	35
H3AB	384	9563	1683	35
H4A	190	10968	2046	37
H4AB	624	11661	1737	37
H5A	1393	12175	2741	45
H5AB	553	12388	2645	45
H6A	-103	11028	2924	57
H6AB	120	11794	3482	57
H7A	-241	10425	3843	70
H7AB	618	10555	4210	70
H8A	221	8938	3900	77
H8AB	53	9258	3190	77
H9A	1147	7678	3846	72
H9AB	720	7959	3126	72
H10C	2277	8014	3741	79
H10D	1841	7243	3219	79
H11A	2774	7972	2755	83
H11B	2974	8727	3320	83
H11C	2703	9099	2610	83
H12A	1705	11214	1634	50
H12B	2211	10374	2043	50
H12C	2109	11350	2374	50
H13A	1404	11658	4200	37
H13B	1441	12531	3752	37
H14A	2116	9048	4411	96
H14B	1431	8911	4636	96

H14C	1648	9961	4474	96
H16	3455	10290	3675	40
H17	3975	11645	4388	38
H18A	2771	13412	4366	64
H18B	3445	12940	4915	64
H18C	2623	12758	4887	64
H1'A	3236	2002	6145	65
H1'B	3747	2694	6684	65
H2'A	4447	1893	6168	59
H2'B	4732	1615	6898	59
H3'A	5129	370	6160	55
H3'B	5224	192	6877	55
H4'A	5378	-1193	6322	53
H4'B	4522	-1144	5918	53
H5'A	4813	-2295	6741	48
H5'B	5082	-1442	7240	48
H6'A	4257	-2554	7489	39
H6'B	3435	-2171	7329	39
H7'A	4201	-1621	8338	38
H7'B	4724	-1095	8031	38
H8'A	4626	363	8360	38
H8'B	4109	68	8740	38
H9'A	3986	1681	8608	43
H9'B	3236	1233	8143	43
H10A	3748	2528	7713	50
H10B	4381	1800	7712	50
H11D	2331	1564	6484	84
H11E	2573	2405	6995	84
H11F	2445	1341	7202	84
H12D	3952	758	5397	72
H12E	3234	770	5584	72
H12F	3617	-229	5536	72
H13C	3428	-2676	6343	33
H13D	3583	-1888	5891	33
H14D	2717	-108	7832	51
H14E	3107	-952	8310	51

H14F	2778	-1161	7572	51
H16'	1632	4	6256	40
H17'	998	-1408	5647	37
H18D	1410	-2965	5269	54
H18E	2114	-3394	5810	54
H18F	2203	-2887	5211	54

Table 23. Torsion angles [°] for $[Fe^{II}(TMC\text{-}Im)]^{2+}$.

C10-N1-C1-C2	175.6(4)	C16-N5-C15-N6	-0.7(4)
C11-N1-C1-C2	-67.0(5)	Fe1-N5-C15-N6	176.1(2)
Fe1-N1-C1-C2	57.9(5)	C16-N5-C15-C13	-178.8(4)
N1-C1-C2-C3	-72.0(5)	Fe1-N5-C15-C13	-2.0(5)
C12-N2-C3-C2	69.2(4)	C17-N6-C15-N5	0.6(4)
C4-N2-C3-C2	-172.2(3)	C18-N6-C15-N5	-177.9(4)
Fe1-N2-C3-C2	-55.9(4)	C17-N6-C15-C13	178.6(4)
C1-C2-C3-N2	69.3(5)	C18-N6-C15-C13	0.1(6)
C12-N2-C4-C5	-76.5(4)	N3-C13-C15-N5	-16.5(5)
C3-N2-C4-C5	164.6(3)	N3-C13-C15-N6	165.7(3)
Fe1-N2-C4-C5	41.1(3)	C15-N5-C16-C17	0.6(4)
C13-N3-C5-C4	156.7(3)	Fe1-N5-C16-C17	-175.0(3)
C6-N3-C5-C4	-81.7(4)	N5-C16-C17-N6	-0.2(5)
Fe1-N3-C5-C4	40.8(3)	C15-N6-C17-C16	-0.2(4)
N2-C4-C5-N3	-59.9(4)	C18-N6-C17-C16	178.3(4)
C13-N3-C6-C7	-76.1(4)	O3-S1-C19-F3	65.2(3)
C5-N3-C6-C7	163.3(4)	O1-S1-C19-F3	-54.4(3)
Fe1-N3-C6-C7	49.7(4)	O2-S1-C19-F3	-174.2(3)
N3-C6-C7-C8	-64.4(5)	O3-S1-C19-F2	-175.2(3)
C14-N4-C8-C7	61.4(5)	O1-S1-C19-F2	65.2(3)
C9-N4-C8-C7	-179.5(4)	O2-S1-C19-F2	-54.6(3)
Fe1-N4-C8-C7	-62.4(5)	O3-S1-C19-F1	-55.8(3)
C6-C7-C8-N4	72.5(6)	O1-S1-C19-F1	-175.4(3)
C8-N4-C9-C10	161.9(4)	O2-S1-C19-F1	64.8(3)
C14-N4-C9-C10	-78.4(5)	O6-S2-C20-F4	-57.9(3)
Fe1-N4-C9-C10	39.6(4)	O5-S2-C20-F4	-177.2(3)
C1-N1-C10-C9	-79.5(5)	O4-S2-C20-F4	62.7(3)
C11-N1-C10-C9	161.3(4)	O6-S2-C20-F5	-179.1(3)
Fe1-N1-C10-C9	42.4(5)	O5-S2-C20-F5	61.6(3)
N4-C9-C10-N1	-57.2(5)	O4-S2-C20-F5	-58.5(3)
C5-N3-C13-C15	-85.0(4)	O6-S2-C20-F6	61.0(3)
C6-N3-C13-C15	153.4(3)	O5-S2-C20-F6	-58.3(3)
Fe1-N3-C13-C15	24.7(4)	O4-S2-C20-F6	-178.4(3)

C11'-N1'-C1'-C2'	-159.3(4)	Fe1'-N5'-C15'-N6'	177.9(2)
C10'-N1'-C1'-C2'	80.9(4)	C16'-N5'-C15'-C13'	-179.4(4)
Fe1'-N1'-C1'-C2'	-38.4(4)	Fe1'-N5'-C15'-C13'	-1.3(5)
C12'-N2'-C2'-C1'	75.5(4)	C17'-N6'-C15'-N5'	0.4(4)
C3'-N2'-C2'-C1'	-165.4(4)	C18'-N6'-C15'-N5'	177.8(3)
Fe1'-N2'-C2'-C1'	-42.3(4)	C17'-N6'-C15'-C13'	179.5(4)
N1'-C1'-C2'-N2'	57.1(5)	C18'-N6'-C15'-C13'	-3.0(6)
C12'-N2'-C3'-C4'	-65.1(5)	N3'-C13'-C15'-N5'	20.4(5)
C2'-N2'-C3'-C4'	176.5(4)	N3'-C13'-C15'-N6'	-158.6(3)
Fe1'-N2'-C3'-C4'	59.4(4)	C15'-N5'-C16'-C17'	0.0(4)
N2'-C3'-C4'-C5'	-71.6(5)	Fe1'-N5'-C16'-C17'	-177.4(3)
C13'-N3'-C5'-C4'	73.6(4)	N5'-C16'-C17'-N6'	0.2(5)
C6'-N3'-C5'-C4'	-168.0(3)	C15'-N6'-C17'-C16'	-0.3(4)
Fe1'-N3'-C5'-C4'	-53.7(4)	C18'-N6'-C17'-C16'	-177.8(4)
C3'-C4'-C5'-N3'	67.0(5)	O2'-S1'-C19'-F2'	60.0(3)
C13'-N3'-C6'-C7'	-155.6(3)	O1'-S1'-C19'-F2'	-179.9(3)
C5'-N3'-C6'-C7'	84.3(4)	O3'-S1'-C19'-F2'	-60.2(3)
Fe1'-N3'-C6'-C7'	-40.3(3)	O2'-S1'-C19'-F1'	-59.9(3)
C14'-N4'-C7'-C6'	73.4(4)	O1'-S1'-C19'-F1'	60.2(3)
C8'-N4'-C7'-C6'	-168.0(3)	O3'-S1'-C19'-F1'	179.9(3)
Fe1'-N4'-C7'-C6'	-44.2(3)	O2'-S1'-C19'-F3'	-179.2(3)
N3'-C6'-C7'-N4'	60.9(4)	O1'-S1'-C19'-F3'	-59.1(3)
C7'-N4'-C8'-C9'	170.0(3)	O3'-S1'-C19'-F3'	60.6(3)
C14'-N4'-C8'-C9'	-71.3(4)	O4'-S2'-C20'-F5'	175.8(3)
Fe1'-N4'-C8'-C9'	52.9(4)	O6'-S2'-C20'-F5'	-63.7(3)
N4'-C8'-C9'-C10'	-69.7(4)	O5'-S2'-C20'-F5'	55.8(3)
C11'-N1'-C10'-C9'	69.8(4)	O4'-S2'-C20'-F4'	55.6(3)
C1'-N1'-C10'-C9'	-171.6(3)	O6'-S2'-C20'-F4'	176.1(3)
Fe1'-N1'-C10'-C9'	-58.2(4)	O5'-S2'-C20'-F4'	-64.4(3)
C8'-C9'-C10'-N1'	73.9(5)	O4'-S2'-C20'-F6'	-63.6(3)
C5'-N3'-C13'-C15'	-158.9(3)	O6'-S2'-C20'-F6'	56.8(3)
C6'-N3'-C13'-C15'	83.4(3)	O5'-S2'-C20'-F6'	176.4(3)
Fe1'-N3'-C13'-C15'	-27.1(4)		
C16'-N5'-C15'-N6'	-0.3(4)		

Fe(II)(TMC)(Cl)

Data collection

A crystal (approximate dimensions 0.200 x 0.100 x 0.100 mm) was placed onto the tip of a 0.5 mm MiTeGen loop and mounted on a Bruker Photon-III CPAD diffractometer for a data collection at 125(2) K.[161] A preliminary set of cell constants was calculated from reflections harvested from two sets of 12 frames. These initial sets of frames were oriented such that orthogonal wedges of reciprocal space were surveyed. This produced initial orientation matrices determined from 132 reflections. The data collection was carried out using MoKα radiation (graphite monochromator) with a frame time of 10 seconds and a detector distance of 7.0 cm. A randomly oriented region of reciprocal space was surveyed to the extent of one sphere and to a resolution of 0.71 Å. Four major sections of frames were collected with 0.30º steps in ω or ϕ. The intensity data were corrected for absorption and decay.[161] Final cell constants were calculated from the xyz centroids of 9993 strong reflections from the actual data collection after integration.[161] Please refer to

Table 24 for additional crystal and refinement information.

Structure solution and refinement

The structure was solved using SHELXT 2014/5 (Sheldrick, 2014)[162] and refined using SHELXL-2018/1 (Sheldrick, 2018).[163] The space group $P2_1/c$ was determined based on systematic absences and intensity statistics A direct-methods solution was calculated which provided most non-hydrogen atoms from the E-map. Full-matrix least squares / difference Fourier cycles were performed which located the remaining non-hydrogen atoms. All non-hydrogen atoms were refined with anisotropic displacement parameters. All hydrogen atoms were placed in ideal positions and refined as riding atoms with relative isotropic displacement parameters. The final full matrix least squares refinement converged to $R1 = 0.0412$ and $wR2 = 0.0924$ (F^2, all data).

Table 24. Crystal data and structure refinement for $[Fe^{II}(TMC)(Cl)]^{+}$.

Identification code	CCDC 1984620	
Empirical formula	$C_{16}\ H_{35}\ C_{l3}\ Fe_{1.50}\ N_5$	
Formula weight	487.61	
Temperature	125(2) K	
Wavelength	0.71073 Å	
Crystal system	Monoclinic	
Space group	$P2_1/c$	
Unit cell dimensions	a = 17.2341(9) Å	α = 90°
	b = 9.2309(5) Å	β = 92.598(2)°
	c = 28.7341(18) Å	γ = 90°
Volume	4566.5(4) $Å^3$	
Z	8	
Density (calculated)	1.419 Mg/m^3	
Absorption coefficient	1.327 mm^{-1}	
F(000)	2048	
Crystal color, morphology	pink, block	
Crystal size	0.200 x 0.100 x 0.100 mm^3	
Theta range for data collection	2.318 to 30.542°	
Index ranges	$-24 \le h \le 24$, $-13 \le k \le 13$, $-41 \le l \le 41$	
Reflections collected	106540	
Independent reflections	13922 [R(int) = 0.0981]	
Observed reflections	10186	
Completeness to theta = 25.242°	99.8%	
Absorption correction	Semi-empirical from equivalents	
Refinement method	Full-matrix least-squares on F^2	
Data / restraints / parameters	13922 / 0 / 470	
Goodness-of-fit on F^2	1.024	
Final R indices [I>2sigma(I)]	$R1$ = 0.0412, $wR2$ = 0.0795	
R indices (all data)	$R1$ = 0.0667, $wR2$ = 0.0924	
Extinction coefficient	n/a	
Largest diff. peak and hole	1.300 and -0.588 $e.Å^{-3}$	

Table 25. Atomic coordinates (x 10^4) and equivalent isotropic displacement parameters ($Å^2$x 10^3) for $[Fe^{II}(TMC)(Cl)]^+$. U_{eq} is defined as one third of the trace of the orthogonalized U_{ij} tensor.

	x	y	z	U_{eq}
Fe1	-352(1)	4071(1)	3891(1)	16(1)
Fe1'	6103(1)	2336(1)	6210(1)	16(1)
Fe2	2614(1)	4995(1)	1999(1)	18(1)
Cl1	418(1)	5686(1)	4298(1)	29(1)
Cl1'	5664(1)	1234(1)	5536(1)	27(1)
Cl2	2911(1)	3014(1)	2464(1)	34(1)
Cl3	2335(1)	4280(1)	1232(1)	23(1)
Cl4	1567(1)	6115(1)	2334(1)	31(1)
Cl5	3585(1)	6740(1)	1979(1)	25(1)
N1	-676(1)	5506(2)	3282(1)	21(1)
N1'	6064(1)	4710(2)	6216(1)	23(1)
N2	-1561(1)	3953(2)	4075(1)	19(1)
N2'	5019(1)	2249(2)	6608(1)	24(1)
N3	-254(1)	2163(2)	4376(1)	22(1)
N3'	6489(1)	733(2)	6728(1)	23(1)
N4	381(1)	2999(2)	3385(1)	17(1)
N4'	7348(1)	2791(2)	6037(1)	21(1)
N5	3696(1)	5844(3)	5355(1)	38(1)
N6	2375(1)	1918(3)	4507(1)	38(1)
C1	148(1)	3641(2)	2922(1)	22(1)
C1'	5731(2)	5441(3)	6622(1)	32(1)
C2	-34(1)	5233(2)	2965(1)	24(1)
C2'	4931(2)	4935(3)	6748(1)	32(1)
C3	-1433(1)	5142(3)	3036(1)	25(1)
C3'	4917(2)	3428(3)	6952(1)	29(1)
C4	-2130(1)	5189(3)	3342(1)	26(1)
C4'	5086(2)	827(3)	6853(1)	33(1)
C5	-2167(1)	3948(3)	3685(1)	24(1)
C5'	5878(2)	616(3)	7076(1)	30(1)
C6	-1671(1)	2592(2)	4342(1)	24(1)

C6'	7238(2)	999(3)	6997(1)	26(1)
C7	-961(1)	2248(3)	4652(1)	26(1)
C7'	7927(1)	1263(3)	6703(1)	28(1)
C8	-238(1)	746(3)	4131(1)	26(1)
C8'	7919(1)	2695(3)	6445(1)	26(1)
C9	420(1)	583(2)	3804(1)	23(1)
C9'	7326(1)	4312(2)	5866(1)	25(1)
C10	310(1)	1395(2)	3347(1)	21(1)
C10'	6875(1)	5252(3)	6177(1)	26(1)
C11	-666(2)	7076(3)	3394(1)	31(1)
C11'	5606(2)	5098(3)	5786(1)	31(1)
C12	-1685(1)	5214(3)	4384(1)	27(1)
C12'	4299(1)	2175(3)	6303(1)	34(1)
C13	430(2)	2267(3)	4709(1)	30(1)
C13'	6544(2)	-663(2)	6474(1)	29(1)
C14	1209(1)	3364(3)	3493(1)	24(1)
C14'	7630(2)	1880(3)	5655(1)	28(1)
C15	2827(2)	1975(3)	4805(1)	28(1)
C16	3418(2)	2057(3)	5182(1)	37(1)
C17	3833(1)	6949(3)	5514(1)	28(1)
C18	3995(2)	8353(3)	5728(1)	38(1)

Table 26. Bond lengths [Å] and angles [°] for $[Fe^{II}(TMC)(Cl)]^{+}$.

Fe(1)-N(2)	2.1765(19)	N(4)-C(10)	1.490(3)
Fe(1)-N(4)	2.2039(18)	N(4)-C(1)	1.493(3)
Fe(1)-N(1)	2.2465(18)	N(4')-C(14')	1.483(3)
Fe(1)-N(3)	2.2473(19)	N(4')-C(9')	1.488(3)
Fe(1)-Cl(1)	2.2835(6)	N(4')-C(8')	1.497(3)
Fe(1')-N(3')	2.1802(18)	N(5)-C(17)	1.138(3)
Fe(1')-N(1')	2.1930(19)	N(6)-C(15)	1.133(3)
Fe(1')-N(2')	2.234(2)	C(1)-C(2)	1.509(3)
Fe(1')-N(4')	2.265(2)	C(1)-H(1A)	0.9900
Fe(1')-Cl(1')	2.2860(6)	C(1)-H(1AB)	0.9900
Fe(2)-Cl(2)	2.3069(6)	C(1')-C(2')	1.515(4)
Fe(2)-Cl(5)	2.3249(6)	C(1')-H(1'A)	0.9900
Fe(2)-Cl(4)	2.3262(7)	C(1')-H(1'B)	0.9900
Fe(2)-Cl(3)	2.3320(6)	C(2)-H(2A)	0.9900
N(1)-C(11)	1.484(3)	C(2)-H(2AB)	0.9900
N(1)-C(2)	1.486(3)	C(2')-C(3')	1.510(4)
N(1)-C(3)	1.493(3)	C(2')-H(2'A)	0.9900
N(1')-C(11')	1.478(3)	C(2')-H(2'B)	0.9900
N(1')-C(1')	1.487(3)	C(3)-C(4)	1.522(3)
N(1')-C(10')	1.494(3)	C(3)-H(3A)	0.9900
N(2)-C(12)	1.484(3)	C(3)-H(3AB)	0.9900
N(2)-C(6)	1.489(3)	C(3')-H(3'A)	0.9900
N(2)-C(5)	1.496(3)	C(3')-H(3'B)	0.9900
N(2')-C(3')	1.487(3)	C(4)-C(5)	1.514(3)
N(2')-C(12')	1.488(3)	C(4)-H(4A)	0.9900
N(2')-C(4')	1.492(3)	C(4)-H(4AB)	0.9900
N(3)-C(7)	1.483(3)	C(4')-C(5')	1.495(4)
N(3)-C(13)	1.487(3)	C(4')-H(4'A)	0.9900
N(3)-C(8)	1.487(3)	C(4')-H(4'B)	0.9900
N(3')-C(13')	1.486(3)	C(5)-H(5A)	0.9900
N(3')-C(5')	1.489(3)	C(5)-H(5AB)	0.9900
N(3')-C(6')	1.496(3)	C(5')-H(5'A)	0.9900
N(4)-C(14)	1.485(3)	C(5')-H(5'B)	0.9900

C(6)-C(7)	1.514(3)	C(12')-H(12E)	0.9800
C(6)-H(6A)	0.9900	C(12')-H(12F)	0.9800
C(6)-H(6AB)	0.9900	C(13)-H(13A)	0.9800
C(6')-C(7')	1.508(4)	C(13)-H(13B)	0.9800
C(6')-H(6'A)	0.9900	C(13)-H(13C)	0.9800
C(6')-H(6'B)	0.9900	C(13')-H(13D)	0.9800
C(7)-H(7A)	0.9900	C(13')-H(13E)	0.9800
C(7)-H(7AB)	0.9900	C(13')-H(13F)	0.9800
C(7')-C(8')	1.516(3)	C(14)-H(14A)	0.9800
C(7')-H(7'A)	0.9900	C(14)-H(14B)	0.9800
C(7')-H(7'B)	0.9900	C(14)-H(14C)	0.9800
C(8)-C(9)	1.512(3)	C(14')-H(14D)	0.9800
C(8)-H(8A)	0.9900	C(14')-H(14E)	0.9800
C(8)-H(8AB)	0.9900	C(14')-H(14F)	0.9800
C(8')-H(8'A)	0.9900	C(15)-C(16)	1.456(3)
C(8')-H(8'B)	0.9900	C(16)-H(16A)	0.9800
C(9)-C(10)	1.515(3)	C(16)-H(16B)	0.9800
C(9)-H(9A)	0.9900	C(16)-H(16C)	0.9800
C(9)-H(9AB)	0.9900	C(17)-C(18)	1.455(4)
C(9')-C(10')	1.489(3)	C(18)-H(18A)	0.9800
C(9')-H(9'A)	0.9900	C(18)-H(18B)	0.9800
C(9')-H(9'B)	0.9900	C(18)-H(18C)	0.9800
C(10)-H(10A)	0.9900		
C(10)-H(10B)	0.9900	N(2)-Fe(1)-N(4)	136.21(7)
C(10')-H(10C)	0.9900	N(2)-Fe(1)-N(1)	90.68(7)
C(10')-H(10D)	0.9900	N(4)-Fe(1)-N(1)	83.10(7)
C(11)-H(11A)	0.9800	N(2)-Fe(1)-N(3)	81.70(7)
C(11)-H(11B)	0.9800	N(4)-Fe(1)-N(3)	91.65(7)
C(11)-H(11C)	0.9800	N(1)-Fe(1)-N(3)	162.70(7)
C(11')-H(11D)	0.9800	N(2)-Fe(1)-Cl(1)	116.69(5)
C(11')-H(11E)	0.9800	N(4)-Fe(1)-Cl(1)	107.11(5)
C(11')-H(11F)	0.9800	N(1)-Fe(1)-Cl(1)	97.62(5)
C(12)-H(12A)	0.9800	N(3)-Fe(1)-Cl(1)	99.68(5)
C(12)-H(12B)	0.9800	N(3')-Fe(1')-N(1')	132.98(7)
C(12)-H(12C)	0.9800	N(3')-Fe(1')-N(2')	82.13(7)
C(12')-H(12D)	0.9800	N(1')-Fe(1')-N(2')	90.31(8)

N(3')-Fe(1')-N(4')	90.70(7)	C(4')-N(2')-Fe(1')	103.01(15)
N(1')-Fe(1')-N(4')	81.14(7)	C(7)-N(3)-C(13)	107.43(18)
N(2')-Fe(1')-N(4')	160.26(7)	C(7)-N(3)-C(8)	109.46(18)
N(3')-Fe(1')-Cl(1')	110.82(5)	C(13)-N(3)-C(8)	109.25(19)
N(1')-Fe(1')-Cl(1')	116.20(5)	C(7)-N(3)-Fe(1)	104.46(14)
N(2')-Fe(1')-Cl(1')	99.54(5)	C(13)-N(3)-Fe(1)	112.52(15)
N(4')-Fe(1')-Cl(1')	100.20(5)	C(8)-N(3)-Fe(1)	113.43(13)
Cl(2)-Fe(2)-Cl(5)	114.99(3)	C(13')-N(3')-C(5')	109.29(19)
Cl(2)-Fe(2)-Cl(4)	105.61(3)	C(13')-N(3')-C(6')	108.89(19)
Cl(5)-Fe(2)-Cl(4)	105.99(2)	C(5')-N(3')-C(6')	106.44(18)
Cl(2)-Fe(2)-Cl(3)	110.69(2)	C(13')-N(3')-Fe(1')	106.12(13)
Cl(5)-Fe(2)-Cl(3)	106.91(2)	C(5')-N(3')-Fe(1')	107.75(14)
Cl(4)-Fe(2)-Cl(3)	112.69(2)	C(6')-N(3')-Fe(1')	118.15(14)
C(11)-N(1)-C(2)	107.31(18)	C(14)-N(4)-C(10)	108.45(17)
C(11)-N(1)-C(3)	108.87(18)	C(14)-N(4)-C(1)	108.24(17)
C(2)-N(1)-C(3)	109.36(18)	C(10)-N(4)-C(1)	108.21(16)
C(11)-N(1)-Fe(1)	113.98(14)	C(14)-N(4)-Fe(1)	109.53(13)
C(2)-N(1)-Fe(1)	102.25(13)	C(10)-N(4)-Fe(1)	116.48(14)
C(3)-N(1)-Fe(1)	114.60(14)	C(1)-N(4)-Fe(1)	105.65(13)
C(11')-N(1')-C(1')	109.6(2)	C(14')-N(4')-C(9')	107.16(18)
C(11')-N(1')-C(10')	108.82(19)	C(14')-N(4')-C(8')	108.69(19)
C(1')-N(1')-C(10')	107.56(18)	C(9')-N(4')-C(8')	108.68(17)
C(11')-N(1')-Fe(1')	104.59(14)	C(14')-N(4')-Fe(1')	113.71(14)
C(1')-N(1')-Fe(1')	118.21(15)	C(9')-N(4')-Fe(1')	103.73(13)
C(10')-N(1')-Fe(1')	107.75(14)	C(8')-N(4')-Fe(1')	114.44(14)
C(12)-N(2)-C(6)	109.15(18)	N(4)-C(1)-C(2)	111.33(17)
C(12)-N(2)-C(5)	109.61(18)	N(4)-C(1)-H(1A)	109.4
C(6)-N(2)-C(5)	106.45(17)	C(2)-C(1)-H(1A)	109.4
C(12)-N(2)-Fe(1)	105.68(13)	N(4)-C(1)-H(1AB)	109.4
C(6)-N(2)-Fe(1)	108.25(14)	C(2)-C(1)-H(1AB)	109.4
C(5)-N(2)-Fe(1)	117.52(14)	H(1A)-C(1)-H(1AB)	108.0
C(3')-N(2')-C(12')	107.71(19)	N(1')-C(1')-C(2')	115.8(2)
C(3')-N(2')-C(4')	109.75(19)	N(1')-C(1')-H(1'A)	108.3
C(12')-N(2')-C(4')	106.41(19)	C(2')-C(1')-H(1'A)	108.3
C(3')-N(2')-Fe(1')	116.15(14)	N(1')-C(1')-H(1'B)	108.3
C(12')-N(2')-Fe(1')	113.29(15)	C(2')-C(1')-H(1'B)	108.3

H(1'A)-C(1')-H(1'B)	107.4	H(4'A)-C(4')-H(4'B)	108.0
N(1)-C(2)-C(1)	112.18(19)	N(2)-C(5)-C(4)	115.84(18)
N(1)-C(2)-H(2A)	109.2	N(2)-C(5)-H(5A)	108.3
C(1)-C(2)-H(2A)	109.2	C(4)-C(5)-H(5A)	108.3
N(1)-C(2)-H(2AB)	109.2	N(2)-C(5)-H(5AB)	108.3
C(1)-C(2)-H(2AB)	109.2	C(4)-C(5)-H(5AB)	108.3
H(2A)-C(2)-H(2AB)	107.9	H(5A)-C(5)-H(5AB)	107.4
C(3')-C(2')-C(1')	114.1(2)	N(3')-C(5')-C(4')	111.2(2)
C(3')-C(2')-H(2'A)	108.7	N(3')-C(5')-H(5'A)	109.4
C(1')-C(2')-H(2'A)	108.7	C(4')-C(5')-H(5'A)	109.4
C(3')-C(2')-H(2'B)	108.7	N(3')-C(5')-H(5'B)	109.4
C(1')-C(2')-H(2'B)	108.7	C(4')-C(5')-H(5'B)	109.4
H(2'A)-C(2')-H(2'B)	107.6	H(5'A)-C(5')-H(5'B)	108.0
N(1)-C(3)-C(4)	114.63(19)	N(2)-C(6)-C(7)	111.20(19)
N(1)-C(3)-H(3A)	108.6	N(2)-C(6)-H(6A)	109.4
C(4)-C(3)-H(3A)	108.6	C(7)-C(6)-H(6A)	109.4
N(1)-C(3)-H(3AB)	108.6	N(2)-C(6)-H(6AB)	109.4
C(4)-C(3)-H(3AB)	108.6	C(7)-C(6)-H(6AB)	109.4
H(3A)-C(3)-H(3AB)	107.6	H(6A)-C(6)-H(6AB)	108.0
N(2')-C(3')-C(2')	114.3(2)	N(3')-C(6')-C(7')	114.82(18)
N(2')-C(3')-H(3'A)	108.7	N(3')-C(6')-H(6'A)	108.6
C(2')-C(3')-H(3'A)	108.7	C(7')-C(6')-H(6'A)	108.6
N(2')-C(3')-H(3'B)	108.7	N(3')-C(6')-H(6'B)	108.6
C(2')-C(3')-H(3'B)	108.7	C(7')-C(6')-H(6'B)	108.6
H(3'A)-C(3')-H(3'B)	107.6	H(6'A)-C(6')-H(6'B)	107.5
C(5)-C(4)-C(3)	114.4(2)	N(3)-C(7)-C(6)	111.09(18)
C(5)-C(4)-H(4A)	108.7	N(3)-C(7)-H(7A)	109.4
C(3)-C(4)-H(4A)	108.7	C(6)-C(7)-H(7A)	109.4
C(5)-C(4)-H(4AB)	108.7	N(3)-C(7)-H(7AB)	109.4
C(3)-C(4)-H(4AB)	108.7	C(6)-C(7)-H(7AB)	109.4
H(4A)-C(4)-H(4AB)	107.6	H(7A)-C(7)-H(7AB)	108.0
N(2')-C(4')-C(5')	111.5(2)	C(6')-C(7')-C(8')	115.2(2)
N(2')-C(4')-H(4'A)	109.3	C(6')-C(7')-H(7'A)	108.5
C(5')-C(4')-H(4'A)	109.3	C(8')-C(7')-H(7'A)	108.5
N(2')-C(4')-H(4'B)	109.3	C(6')-C(7')-H(7'B)	108.5
C(5')-C(4')-H(4'B)	109.3	C(8')-C(7')-H(7'B)	108.5

H(7'A)-C(7')-H(7'B)	107.5	H(10C)-C(10')-H(10D)	108.0
N(3)-C(8)-C(9)	114.43(19)	N(1)-C(11)-H(11A)	109.5
N(3)-C(8)-H(8A)	108.7	N(1)-C(11)-H(11B)	109.5
C(9)-C(8)-H(8A)	108.7	H(11A)-C(11)-H(11B)	109.5
N(3)-C(8)-H(8AB)	108.7	N(1)-C(11)-H(11C)	109.5
C(9)-C(8)-H(8AB)	108.7	H(11A)-C(11)-H(11C)	109.5
H(8A)-C(8)-H(8AB)	107.6	H(11B)-C(11)-H(11C)	109.5
N(4')-C(8')-C(7')	115.21(19)	N(1')-C(11')-H(11D)	109.5
N(4')-C(8')-H(8'A)	108.5	N(1')-C(11')-H(11E)	109.5
C(7')-C(8')-H(8'A)	108.5	H(11D)-C(11')-H(11E)	109.5
N(4')-C(8')-H(8'B)	108.5	N(1')-C(11')-H(11F)	109.5
C(7')-C(8')-H(8'B)	108.5	H(11D)-C(11')-H(11F)	109.5
H(8'A)-C(8')-H(8'B)	107.5	H(11E)-C(11')-H(11F)	109.5
C(8)-C(9)-C(10)	114.91(19)	N(2)-C(12)-H(12A)	109.5
C(8)-C(9)-H(9A)	108.5	N(2)-C(12)-H(12B)	109.5
C(10)-C(9)-H(9A)	108.5	H(12A)-C(12)-H(12B)	109.5
C(8)-C(9)-H(9AB)	108.5	N(2)-C(12)-H(12C)	109.5
C(10)-C(9)-H(9AB)	108.5	H(12A)-C(12)-H(12C)	109.5
H(9A)-C(9)-H(9AB)	107.5	H(12B)-C(12)-H(12C)	109.5
N(4')-C(9')-C(10')	111.00(19)	N(2')-C(12')-H(12D)	109.5
N(4')-C(9')-H(9'A)	109.4	N(2')-C(12')-H(12E)	109.5
C(10')-C(9')-H(9'A)	109.4	H(12D)-C(12')-H(12E)	109.5
N(4')-C(9')-H(9'B)	109.4	N(2')-C(12')-H(12F)	109.5
C(10')-C(9')-H(9'B)	109.4	H(12D)-C(12')-H(12F)	109.5
H(9'A)-C(9')-H(9'B)	108.0	H(12E)-C(12')-H(12F)	109.5
N(4)-C(10)-C(9)	114.99(17)	N(3)-C(13)-H(13A)	109.5
N(4)-C(10)-H(10A)	108.5	N(3)-C(13)-H(13B)	109.5
C(9)-C(10)-H(10A)	108.5	H(13A)-C(13)-H(13B)	109.5
N(4)-C(10)-H(10B)	108.5	N(3)-C(13)-H(13C)	109.5
C(9)-C(10)-H(10B)	108.5	H(13A)-C(13)-H(13C)	109.5
H(10A)-C(10)-H(10B)	107.5	H(13B)-C(13)-H(13C)	109.5
C(9')-C(10')-N(1')	111.48(19)	N(3')-C(13')-H(13D)	109.5
C(9')-C(10')-H(10C)	109.3	N(3')-C(13')-H(13E)	109.5
N(1')-C(10')-H(10C)	109.3	H(13D)-C(13')-H(13E)	109.5
C(9')-C(10')-H(10D)	109.3	N(3')-C(13')-H(13F)	109.5
N(1')-C(10')-H(10D)	109.3	H(13D)-C(13')-H(13F)	109.5

H(13E)-C(13')-H(13F)	109.5	C(15)-C(16)-H(16A)	109.5
N(4)-C(14)-H(14A)	109.5	C(15)-C(16)-H(16B)	109.5
N(4)-C(14)-H(14B)	109.5	H(16A)-C(16)-H(16B)	109.5
H(14A)-C(14)-H(14B)	109.5	C(15)-C(16)-H(16C)	109.5
N(4)-C(14)-H(14C)	109.5	H(16A)-C(16)-H(16C)	109.5
H(14A)-C(14)-H(14C)	109.5	H(16B)-C(16)-H(16C)	109.5
H(14B)-C(14)-H(14C)	109.5	N(5)-C(17)-C(18)	178.5(3)
N(4')-C(14')-H(14D)	109.5	C(17)-C(18)-H(18A)	109.5
N(4')-C(14')-H(14E)	109.5	C(17)-C(18)-H(18B)	109.5
H(14D)-C(14')-H(14E)	109.5	H(18A)-C(18)-H(18B)	109.5
N(4')-C(14')-H(14F)	109.5	C(17)-C(18)-H(18C)	109.5
H(14D)-C(14')-H(14F)	109.5	H(18A)-C(18)-H(18C)	109.5
H(14E)-C(14')-H(14F)	109.5	H(18B)-C(18)-H(18C)	109.5
N(6)-C(15)-C(16)	179.0(3)		

Table 27. Anisotropic displacement parameters ($Å^2 x\ 10^3$) for $[Fe^{II}(TMC)(Cl)]^+$. The anisotropic displacement factor exponent takes the form: $-2p^2[\ h^2\ a^{*2}U_{11} + ...\ + 2\ h\ k\ a^*\ b^*\ U_{12}\ ]$

	U_{11}	U_{22}	U_{33}	U_{23}	U_{13}	U_{12}
Fe1	16(1)	19(1)	14(1)	-3(1)	2(1)	-4(1)
Fe1'	18(1)	16(1)	14(1)	-1(1)	2(1)	-3(1)
Fe2	19(1)	18(1)	18(1)	1(1)	1(1)	1(1)
Cl1	26(1)	35(1)	26(1)	-12(1)	4(1)	-13(1)
Cl1'	30(1)	33(1)	18(1)	-6(1)	0(1)	-7(1)
Cl2	45(1)	27(1)	30(1)	9(1)	-4(1)	4(1)
Cl3	26(1)	24(1)	20(1)	1(1)	-2(1)	-1(1)
Cl4	22(1)	33(1)	37(1)	1(1)	9(1)	5(1)
Cl5	22(1)	25(1)	28(1)	-3(1)	1(1)	-4(1)
N1	22(1)	21(1)	21(1)	2(1)	5(1)	0(1)
N1'	25(1)	21(1)	24(1)	-1(1)	4(1)	-3(1)
N2	19(1)	23(1)	17(1)	-2(1)	2(1)	-4(1)
N2'	20(1)	30(1)	23(1)	-2(1)	5(1)	-5(1)
N3	21(1)	29(1)	17(1)	2(1)	3(1)	-3(1)
N3'	28(1)	21(1)	18(1)	4(1)	6(1)	-1(1)
N4	18(1)	19(1)	15(1)	0(1)	2(1)	-1(1)
N4'	21(1)	22(1)	21(1)	3(1)	0(1)	-3(1)
N5	37(1)	37(1)	40(1)	-5(1)	6(1)	-6(1)
N6	36(1)	44(1)	33(1)	-1(1)	0(1)	3(1)
C1	25(1)	28(1)	12(1)	-1(1)	3(1)	2(1)
C1'	35(1)	23(1)	38(1)	-8(1)	9(1)	-2(1)
C2	26(1)	27(1)	19(1)	6(1)	4(1)	-1(1)
C2'	27(1)	35(1)	34(1)	-12(1)	7(1)	3(1)
C3	25(1)	28(1)	22(1)	2(1)	0(1)	4(1)
C3'	23(1)	41(2)	24(1)	-7(1)	4(1)	-3(1)
C4	21(1)	30(1)	26(1)	1(1)	-2(1)	3(1)
C4'	33(1)	35(1)	31(1)	2(1)	10(1)	-14(1)
C5	18(1)	29(1)	23(1)	-2(1)	0(1)	-3(1)
C5'	36(1)	30(1)	24(1)	5(1)	8(1)	-7(1)
C6	23(1)	25(1)	24(1)	2(1)	6(1)	-5(1)

C6'	36(1)	25(1)	16(1)	1(1)	-2(1)	4(1)
C7	24(1)	35(1)	21(1)	5(1)	8(1)	-2(1)
C7'	26(1)	30(1)	27(1)	3(1)	-4(1)	3(1)
C8	26(1)	22(1)	29(1)	5(1)	3(1)	-2(1)
C8'	21(1)	30(1)	28(1)	3(1)	-3(1)	-3(1)
C9	25(1)	20(1)	25(1)	1(1)	0(1)	1(1)
C9'	23(1)	25(1)	28(1)	7(1)	2(1)	-6(1)
C10	23(1)	21(1)	20(1)	-4(1)	0(1)	0(1)
C10'	29(1)	22(1)	29(1)	1(1)	3(1)	-7(1)
C11	39(2)	19(1)	35(1)	2(1)	10(1)	-1(1)
C11'	33(1)	31(1)	31(1)	4(1)	4(1)	5(1)
C12	23(1)	33(1)	26(1)	-9(1)	6(1)	-4(1)
C12'	19(1)	48(2)	36(1)	-10(1)	3(1)	-8(1)
C13	27(1)	42(2)	20(1)	4(1)	-2(1)	-1(1)
C13'	42(2)	20(1)	25(1)	2(1)	1(1)	-3(1)
C14	20(1)	28(1)	25(1)	0(1)	3(1)	-4(1)
C14'	27(1)	34(1)	24(1)	0(1)	7(1)	-2(1)
C15	32(1)	26(1)	26(1)	3(1)	6(1)	2(1)
C16	38(2)	38(2)	32(1)	2(1)	-7(1)	-1(1)
C17	24(1)	34(1)	26(1)	3(1)	4(1)	-1(1)
C18	46(2)	31(1)	36(1)	-5(1)	7(1)	-5(1)

Table 28. Hydrogen coordinates (x 10^4) and isotropic displacement parameters (Å^2 x 10^3) for $[Fe^{II}(TMC)(Cl)]^+$.

	x	y	z	U(eq)
H1A	-315	3127	2790	26
H1AB	574	3511	2707	26
H1'A	5706	6494	6558	38
H1'B	6092	5299	6896	38
H2A	438	5752	3084	29
H2AB	-179	5626	2652	29
H2'A	4723	5622	6976	38
H2'B	4582	4961	6465	38
H3A	-1395	4159	2902	30
H3AB	-1524	5829	2775	30
H3'A	5335	3351	7199	35
H3'B	4416	3284	7101	35
H4A	-2118	6112	3518	31
H4AB	-2610	5183	3140	31
H4'A	4974	35	6627	39
H4'B	4695	779	7095	39
H5A	-2685	3960	3821	28
H5AB	-2124	3028	3511	28
H5'A	5972	1356	7321	36
H5'B	5909	-350	7225	36
H6A	-1774	1781	4123	29
H6AB	-2128	2697	4537	29
H6'A	7351	151	7200	31
H6'B	7172	1849	7202	31
H7A	-890	3008	4893	32
H7AB	-1038	1312	4811	32
H7'A	7954	469	6473	34
H7'B	8405	1216	6907	34
H8A	-736	616	3951	31

H8AB	-196	-36	4366	31
H8'A	7804	3476	6667	31
H8'B	8446	2875	6333	31
H9A	486	-459	3735	28
H9AB	905	925	3965	28
H9'A	7086	4339	5547	30
H9'B	7863	4688	5854	30
H10A	699	1040	3131	26
H10B	-211	1160	3208	26
H10C	6860	6252	6052	32
H10D	7137	5280	6490	32
H11A	-739	7638	3106	47
H11B	-166	7330	3549	47
H11C	-1087	7296	3601	47
H11D	5565	6155	5762	47
H11E	5085	4679	5797	47
H11F	5864	4719	5515	47
H12A	-2216	5193	4491	41
H12B	-1604	6112	4211	41
H12C	-1315	5169	4653	41
H12D	3850	2033	6495	51
H12E	4336	1363	6085	51
H12F	4236	3081	6127	51
H13A	443	1421	4915	45
H13B	390	3151	4896	45
H13C	906	2299	4536	45
H13D	6712	-1427	6692	44
H13E	6922	-570	6231	44
H13F	6034	-912	6330	44
H14A	1369	2978	3800	36
H14B	1273	4419	3493	36
H14C	1531	2937	3256	36
H14D	8142	2221	5569	42
H14E	7265	1946	5384	42
H14F	7668	870	5759	42
H16A	3203	1698	5470	55

H16B	3583	3066	5226	55
H16C	3866	1463	5105	55
H18A	4431	8811	5576	56
H18B	4130	8222	6060	56
H18C	3534	8971	5691	56

Table 29. Torsion angles [°] for $[Fe^{II}(TMC)(Cl)]^{+}$.

C14-N4-C1-C2	-80.2(2)	C13'-N3'-C6'-C7'	66.7(2)
C10-N4-C1-C2	162.49(19)	C5'-N3'-C6'-C7'	-175.6(2)
Fe1-N4-C1-C2	37.1(2)	Fe1'-N3'-C6'-C7'	-54.4(2)
C11'-N1'-C1'-C2'	67.2(3)	C13-N3-C7-C6	163.3(2)
C10'-N1'-C1'-C2'	-174.6(2)	C8-N3-C7-C6	-78.2(2)
Fe1'-N1'-C1'-C2'	-52.5(3)	Fe1-N3-C7-C6	43.6(2)
C11-N1-C2-C1	165.45(19)	N2-C6-C7-N3	-55.9(3)
C3-N1-C2-C1	-76.6(2)	N3'-C6'-C7'-C8'	70.2(3)
Fe1-N1-C2-C1	45.24(19)	C7-N3-C8-C9	174.82(18)
N4-C1-C2-N1	-59.5(2)	C13-N3-C8-C9	-67.8(2)
N1'-C1'-C2'-C3'	70.3(3)	Fe1-N3-C8-C9	58.6(2)
C11-N1-C3-C4	-70.5(2)	C14'-N4'-C8'-C7'	-72.1(3)
C2-N1-C3-C4	172.50(19)	C9'-N4'-C8'-C7'	171.6(2)
Fe1-N1-C3-C4	58.4(2)	Fe1'-N4'-C8'-C7'	56.2(2)
C12'-N2'-C3'-C2'	-70.9(3)	C6'-C7'-C8'-N4'	-72.9(3)
C4'-N2'-C3'-C2'	173.6(2)	N3-C8-C9-C10	-75.8(2)
Fe1'-N2'-C3'-C2'	57.4(2)	C14'-N4'-C9'-C10'	166.16(19)
C1'-C2'-C3'-N2'	-73.4(3)	C8'-N4'-C9'-C10'	-76.6(2)
N1-C3-C4-C5	-72.6(3)	Fe1'-N4'-C9'-C10'	45.6(2)
C3'-N2'-C4'-C5'	-78.1(3)	C14-N4-C10-C9	70.8(2)
C12'-N2'-C4'-C5'	165.6(2)	C1-N4-C10-C9	-172.05(19)
Fe1'-N2'-C4'-C5'	46.2(2)	Fe1-N4-C10-C9	-53.3(2)
C12-N2-C5-C4	66.4(3)	C8-C9-C10-N4	71.6(3)
C6-N2-C5-C4	-175.7(2)	N4'-C9'-C10'-N1'	-57.9(2)
Fe1-N2-C5-C4	-54.2(2)	C11'-N1'-C10'-C9'	-76.7(2)
C3-C4-C5-N2	69.3(3)	C1'-N1'-C10'-C9'	164.62(19)
C13'-N3'-C5'-C4'	-80.9(2)	Fe1'-N1'-C10'-C9'	36.2(2)
C6'-N3'-C5'-C4'	161.7(2)		
Fe1'-N3'-C5'-C4'	34.0(2)		
N2'-C4'-C5'-N3'	-57.0(3)		
C12-N2-C6-C7	-78.8(2)		
C5-N2-C6-C7	162.93(19)		
Fe1-N2-C6-C7	35.7(2)		

Appendix

Experimental Section

General considerations. All chemicals and solvents were of commercially available quality and used without further purification unless otherwise specified. All moisture and oxygen sensitive compounds were prepared using standard Schlenk-line techniques, and a nitrogen-filled glove box was used for any subsequent manipulation and storage of these compounds. $Fe^{II}(OTf)_2 \bullet 2CH_3CN$ was prepared according to the published procedure.[164] UV-vis absorption spectra were recorded on a HP8453A diode array spectrometer equipped with a cryostat from Unisoku Scientific Instruments (Osaka, Japan).

Raman Spectroscopy. Raman spectra were obtained at room temperature, 243 K, or 77 K with excitation at 407 nm (30 mW at source, Cobolt Lasers), 457 nm (50 mW at source, Cobolt Lasers), or 561 nm (100 mW at source, Cobolt Lasers) through the sample in a flat bottom NMR tube using a 90° backscattering arrangement (parallel to the slit direction) or through the sample in a NMR or EPR tube using a 135° backscattering arrangement. The collimated Raman scattering was collected using two Plano convex lenses (f = 5 cm and 10 cm, placed at an appropriate distance) through appropriate long pass edge filters (Semrock) into an Acton AM-506M3 monochromator equipped with a Princeton Instruments ACTON PyLON LN/CCD-1340x400 detector. The detector was cooled to - 120 °C prior to the experiments. Spectral calibration was performed using the Raman spectrum of acetonitrile/toluene 50:50 (v:v).[165] Each spectrum was accumulated, typically resulting in a total acquisition time of 1-10 min per spectrum.

X-ray Absorption Spectroscopy Iron K-edge X-ray absorption spectra were collected on SSRL beamline 9−3 using a 100- element solid-state Ge detector(Canberra) with a SPEAR storage ring current of~500 mA at a power of 3.0 GeV. The incoming X-rays were unfocused using a Si(220)

doublecrystal monochromator, which was detuned to 70% of the maximal flux to attenuate harmonic X-rays. Six scans of the fluorescence excitation spectra for the sample were collected from 6882 to 8000 eV at a temperature (10 K) that was controlled by an Oxford Instruments CF1208 continuous-flow liquid helium cryostat. An iron foil was placed in the beam pathway prior to the ionization chamber (I_o) and scanned concomitantly for energy calibration, with the first inflection point of the edge assigned to 7112.0 eV. A 3 or 6 μm Mn filter may have been used to increase the signal-to-noise ratio, and a Soller slit was used to increase the signal-to-noise ratio of the spectra. Photoreduction was monitored by scanning the same spot on the sample twice and comparing the first-derivative peaks associated with the edge energy during collection, but none was observed in the present study. The detector channels from the scans were examined, calibrated, averaged, and processed for EXAFS analysis using EXAFSPAK to extract χ(k).[166] Theoretical phase and amplitude parameters for a given absorber−scatterer pair were calculated using FEFF 8.40 and were utilized by the "opt" program of the EXAFSPAK package during curve fitting. In all analyses, the coordination number of a given shell was a fixed parameter and was varied iteratively in integer steps, while bond lengths (R) and mean-square deviation (σ^2) were allowed to float freely. The amplitude reduction factor S_0 was fixed at 0.9, while the edge-shift parameter E_0 was allowed to float as a single value for all shells. Thus, in any given fit, the number of floating parameters was typically equal to (2×number of shells) + 1. The k range of the data is specified for each sample, but typically 2 – 14 or 2 – 15 $Å^{-1}$. Pre-edge analysis was performed on data normalized in the "process" program of the EXAFSPAK package, and pre-edge features were fit between 7108 and 7118 eV using the Fityk program with pseudo-Voigt functions composed of 50:50 Gaussian/Lorentzian functions.[167]

Bibliography

1. Wong, S. D.; Srnec, M.; Matthews, M. L.; Liu, L. V.; Kwak, Y.; Park, K.; Bell, C. B., 3rd; Alp, E. E.; Zhao, J.; Yoda, Y.; Kitao, S.; Seto, M.; Krebs, C.; Bollinger, J. M., Jr.; Solomon, E. I., Elucidation of the Fe(IV)=O intermediate in the catalytic cycle of the halogenase SyrB2. *Nature* **2013,** *499* (7458), 320-323.
2. Klinker, E. J.; Kaizer, J.; Brennessel, W. W.; Woodrum, N. L.; Cramer, C. J.; Que, L., Jr., Structures of nonheme oxoiron(IV) complexes from X-ray crystallography, NMR spectroscopy, and DFT calculations. *Angew. Chem. Int. Ed.* **2005,** *44* (24), 3690-3694.
3. Rasheed, W.; Draksharapu, A.; Banerjee, S.; Young, V. G., Jr.; Fan, R.; Guo, Y.; Ozerov, M.; Nehrkorn, J.; Krzystek, J.; Telser, J.; Que, L., Jr., Crystallographic Evidence for a Sterically Induced Ferryl Tilt in a Non-Heme Oxoiron(IV) Complex that Makes it a Better Oxidant. *Angew. Chem. Int. Ed.* **2018,** *57* (30), 9387-9391.
4. Sheng, Y.; Abelson, C. S.; Prakash, J.; Draksharapu, A.; Young Jr, V. G.; Que Jr, L., Unmasking Steps in Intramolecular Aromatic Hydroxylation by a Synthetic Nonheme Oxoiron (IV) Complex. *Angew. Chem. Int. Ed.* **2021,** *60* (38), 20991-20998.
5. Mukherjee, G.; Alili, A.; Barman, P.; Kumar, D.; Sastri, C. V.; de Visser, S. P., Interplay Between Steric and Electronic Effects: A Joint Spectroscopy and Computational Study of Nonheme Iron(IV)-Oxo Complexes. *Chem. Eur. J.* **2019,** *25* (19), 5086-5098.
6. Huang, X.; Groves, J. T., Oxygen Activation and Radical Transformations in Heme Proteins and Metalloporphyrins. *Chem. Rev.* **2018,** *118* (5), 2491-2553.
7. Jia, Z. J.; Gao, S.; Arnold, F. H., Enzymatic Primary Amination of Benzylic and Allylic C(sp3)−H Bonds. *J. Am. Chem. Soc.* **2020,** *142* (23), 10279-10283.
8. Goldberg, N. W.; Knight, A. M.; Zhang, R. K.; Arnold, F. H., Nitrene Transfer Catalyzed by a Non-Heme Iron Enzyme and Enhanced by Non-Native Small-Molecule Ligands. *J. Am. Chem. Soc.* **2019,** *141* (50), 19585-19588.
9. Abelson, C. S.; Aboelenen, A. M.; Rasheed, W.; Que, L., Jr., 8.17 - Synthetic Nonheme High-Valent Iron-Oxo Complexes Structures and Oxidative Function. In *Comprehensive Coordination Chemistry III*, Constable, E. C.; Parkin, G.; Que Jr, L., Eds. Elsevier: Oxford, 2021; pp 412-454.
10. Koehntop, K. D.; Emerson, J. P.; Que, L., Jr., The 2-His-1-carboxylate Facial Triad: A Versatile Platform for Dioxygen Activation by Mononuclear Nonheme Iron(II) Enzymes. *J. Biol. Inorg. Chem.* **2005,** *10* (2), 87-93.
11. Krebs, C.; Fujimori, D. G.; Walsh, C. T.; Bollinger, J. M., Jr., Non-Heme Fe(IV)–Oxo Intermediates. *Acc. Chem. Res.* **2007,** *40* (7), 484-492.
12. Que, L., Jr., The road to non-heme oxoferryls and beyond. *Acc. Chem. Res.* **2007,** *40* (7), 493-500.
13. Solomon, E. I.; Goudarzi, S.; Sutherlin, K. D., O2 Activation by Non-Heme Iron Enzymes. *Biochemistry* **2016,** *55* (46), 6363-6374.
14. Srnec, M.; Wong, S. D.; Matthews, M. L.; Krebs, C.; Bollinger, J. M., Jr.; Solomon, E. I., Electronic Structure of the Ferryl Intermediate in the α-Ketoglutarate Dependent Non-Heme Iron Halogenase SyrB2: Contributions to H Atom Abstraction Reactivity. *J. Am. Chem. Soc.* **2016,** *138*, 5110-5122.
15. Bollinger, J. M., Jr.; Price, J. C.; Hoffart, L. M.; Barr, E. W.; Krebs, C., Mechanism of Taurine: α-Ketoglutarate Dioxygenase (TauD) from *Escherichia coli*. *Eur. J. Inorg. Chem.* **2005**, 4245-4254.

16. Riggs-Gelasco, P. J.; Price, J. C.; Guyer, R. B.; Brehm, J. H.; Barr, E. W.; Bollinger, J. M., Jr.; Krebs, C., EXAFS Spectroscopic Evidence for an Fe=O Unit in the Fe(IV) Intermediate Observed during Oxygen Activation by Taurine:alpha-Ketoglutarate Dioxygenase. *J. Am. Chem. Soc.* **2004,** *126* (26), 8108-8109.
17. Price, J. C.; Barr, E. W.; Tirupati, B.; Bollinger, J. M., Jr.; Krebs, C., The First Direct Characterization of a High-Valent Iron Intermediate in the Reaction of an α-Ketoglutarate-Dependent Dioxygenase: A High-Spin Fe(IV) Complex in Taurine/α-Ketoglutarate Dioxygenase (TauD) from Escherichia coli. *Biochemistry* **2003,** *42* (24), 7497-7508.
18. Krebs, C.; Price, J. C.; Baldwin, J.; Saleh, L.; Green, M. T.; Bollinger, J. M., Jr., Rapid Freeze-Quench ^{57}Fe Mössbauer Spectroscopy: Monitoring Changes of an Iron-Containing Active Site during a Biochemical Reaction. *Inorg. Chem.* **2005,** *44* (4), 742-757.
19. Matthews, M. L.; Krest, C. M.; Barr, E. W.; Vaillancourt, F. H.; Walsh, C. T.; Green, M. T.; Krebs, C.; Bollinger, J. M., Jr., Substrate-Triggered Formation and Remarkable Stability of the C−H Bond-Cleaving Chloroferryl Intermediate in the Aliphatic Halogenase, SyrB2. *Biochemistry* **2009,** *48* (20), 4331-4343.
20. Proshlyakov, D. A.; Henshaw, T. F.; Monterosso, G. R.; Ryle, M. J.; Hausinger, R. P., Direct Detection of Oxygen Intermediates in the Non-Heme Fe Enzyme Taurine/α-Ketoglutarate Dioxygenase. *J. Am. Chem. Soc.* **2004,** *126*, 1022-1023.
21. Banerjee, R.; Jones, J. C.; Lipscomb, J. D., Soluble Methane Monooxygenase. *Annu. Rev. Biochem.* **2019,** *88* (1), 409−431.
22. Cutsail III, G.; Banerjee, R.; Zhou, A.; Que, L., Jr.; Lipscomb, J. D.; DeBeer, S., High-Resolution EXAFS Provides Evidence for a Longer Fe•••Fe Distance in the Q Intermediate of Methane Monooxygenase. *J. Am. Chem. Soc.* **2018,** *140*, 16807-16820.
23. Shu, L.; Nesheim, J. C.; Kauffmann, K.; Münck, E.; Lipscomb, J. D.; Que, L., Jr., An $Fe_2^{IV}O_2$ Diamond Core Structure for the Key Intermediate Q of Methane Monooxygenase. *Science* **1997,** *275* (5299), 515-518.
24. Lee, S.-K.; Fox, B. G.; Froland, W. A.; Lipscomb, J. D.; Münck, E., A Transient Intermediate of the Methane Monooxygenase Catalytic Cycle Containing an $Fe^{IV}Fe^{IV}$ Cluster. *J. Am. Chem. Soc.* **1993,** *115*, 6450-6451.
25. Jasniewski, A. J.; Que, L., Jr., Dioxygen Activation by Nonheme Diiron Enzymes: Diverse Dioxygen Adducts, High-Valent Intermediates, and Related Model Complexes. *Chem. Rev.* **2018,** *118* (5), 2554–2592.
26. Castillo, R. G.; Banerjee, R.; Allpress, C. J.; Rohde, G. T.; Bill, E.; Que, L., Jr.; Lipscomb, J. D.; DeBeer, S., High-Energy-Resolution Fluorescence-Detected X-ray Absorption of the Q Intermediate of Soluble Methane Monooxygenase. *J. Am. Chem. Soc.* **2017,** *139* (49), 18024-18033.
27. Banerjee, R.; Proshlyakov, Y.; Lipscomb, J. D.; Proshlyakov, D. A., Structure of the key species in the enzymatic oxidation of methane to methanol. *Nature* **2015,** *518* (7539), 431-434.
28. Nesheim, J. C.; Lipscomb, J. D., Large Kinetic Isotope Effects in Methane Oxidation Catalyzed by Methane Monooxygenase: Evidence for C-H Bond Cleavage in a Reaction Cycle Intermediate. *Biochemistry* **1996,** *35*, 10240-10247.
29. Jacobs, A. B.; Banerjee, R.; Deweese, D. E.; Braun, A.; Babicz, J. T., Jr.; Gee, L. B.; Sutherlin, K. D.; Böttger, L. H.; Yoda, Y.; Saito, M.; Kitao, S.; Kobayashi, Y.; Seto, M.; Tamasaku, K.; Lipscomb, J. D.; Park, K.; Solomon, E. I., Nuclear Resonance Vibrational Spectroscopic Definition of the $Fe(IV)_2$ Intermediate Q in Methane Monooxygenase and Its Reactivity. *J. Am. Chem. Soc.* **2021,** *143* (39), 16007-16029.
30. Banerjee, S.; Draksharapu, A.; Crossland, P. M.; Fan, R.; Guo, Y.; Swart, M.; Que, L., Jr., Sc^{3+}-promoted O–O bond cleavage of a (μ-1,2-peroxo)diiron(III) species formed from an iron(II)

precursor and O_2 to generate a complex with an $Fe^{IV}2(\mu\text{-}O)_2$ core. *J. Am. Chem. Soc.* **2020,** *142* (9), 4285-4297.
31. Pestovsky, O.; Stoian, S.; Bominaar, E. L.; Shan, X.; Münck, E.; Que, L., Jr.; Bakac, A., Aqueous Fe^{IV}=O: spectroscopic identification and oxo-group exchange. *Angew. Chem. Int. Ed.* **2005,** *44* (42), 6871-6874.
32. Hoffart, L. M.; Barr, E. W.; Guyer, R. B.; Bollinger, J. M., Jr.; Krebs, C., Direct spectroscopic detection of a C-H-cleaving high-spin Fe(IV) complex in a prolyl-4-hydroxylase. *Proc. Natl. Acad. Sci. U.S.A.* **2006,** *103* (40), 14738-14743.
33. Panay, A. J.; Lee, M.; Krebs, C.; Bollinger, J. M.; Fitzpatrick, P. F., Evidence for a high-spin Fe(IV) species in the catalytic cycle of a bacterial phenylalanine hydroxylase. *Biochemistry* **2011,** *50* (11), 1928-1933.
34. Eser, B. E.; Barr, E. W.; Frantom, P. A.; Saleh, L.; Bollinger, J. M.; Krebs, C.; Fitzpatrick, P. F., Direct Spectroscopic Evidence for a High-Spin Fe(IV) Intermediate in Tyrosine Hydroxylase. *J. Am. Chem. Soc.* **2007,** *129* (37), 11334-11335.
35. England, J.; Martinho, M.; Farquhar, E. R.; Frisch, J. R.; Bominaar, E. L.; Münck, E.; Que, L., Jr., A synthetic high-spin oxoiron(IV) complex: generation, spectroscopic characterization, and reactivity. *Angew. Chem. Int. Ed.* **2009,** *48* (20), 3622-3626.
36. England, J.; Guo, Y.; Farquhar, E. R.; Young, V. G., Jr.; Münck, E.; Que, L., Jr., The crystal structure of a high-spin oxoiron(IV) complex and characterization of its self-decay pathway. *J. Am. Chem. Soc.* **2010,** *132* (25), 8635-8644.
37. Lacy, D. C.; Gupta, R.; Stone, K. L.; Greaves, J.; Ziller, J. W.; Hendrich, M. P.; Borovik, A. S., Formation, structure, and EPR detection of a high spin Fe(IV)-oxo species derived from either an Fe(III)-oxo or Fe(III)-OH complex. *J. Am. Chem. Soc.* **2010,** *132* (35), 12188-12190.
38. Mitchell, A. J.; Dunham, N. P.; Martinie, R. J.; Bergman, J. A.; Pollock, C. J.; Hu, K.; Allen, B. D.; Chang, W. C.; Silakov, A.; Bollinger, J. M., Jr.; Krebs, C.; Boal, A. K., Visualizing the Reaction Cycle in an Iron(II)- and 2-(Oxo)-glutarate-Dependent Hydroxylase. *J. Am. Chem. Soc.* **2017,** *139* (39), 13830-13836.
39. Biswas, A. N.; Puri, M.; Meier, K. K.; Oloo, W. N.; Rohde, G. T.; Bominaar, E. L.; Münck, E.; Que, L., Jr., Modeling TauD-**J**: A High-Spin Nonheme Oxoiron(IV) Complex with High Reactivity toward C–H Bonds. *J. Am. Chem. Soc.* **2015,** *137* (7), 2428-2431.
40. Puri, M.; Biswas, A. N.; Fan, R.; Guo, Y.; Que, L., Jr., Modeling Non-Heme Iron Halogenases: High-Spin Oxoiron(IV)−Halide Complexes That Halogenate C−H Bonds. *J. Am. Chem. Soc.* **2016,** *138*, 2484-2487.
41. Rohde, J. U.; Torelli, S.; Shan, X.; Lim, M. H.; Klinker, E. J.; Kaizer, J.; Chen, K.; Nam, W.; Que, L., Jr., Structural insights into nonheme alkylperoxoiron(III) and oxoiron(IV) intermediates by X-ray absorption spectroscopy. *J. Am. Chem. Soc.* **2004,** *126* (51), 16750-16761.
42. Sinnecker, S.; Svensen, N.; Barr, E. W.; Ye, S.; Bollinger, J. M., Jr.; Neese, F.; Krebs, C., Spectroscopic and Computational Evaluation of the Structure of the High-Spin Fe(IV)-Oxo Intermediates in Taurine: α-Ketoglutarate Dioxygenase from Escherichia coli and Its His99Ala Ligand Variant. *J. Am. Chem. Soc.* **2007,** *129* (19), 6168-6179.
43. Galonić, D. P.; Barr, E. W.; Walsh, C. T.; Bollinger, J. M., Jr.; Krebs, C., Two interconverting Fe(IV) intermediates in aliphatic chlorination by the halogenase CytC3. *Nature Chem. Biol.* **2007,** *3* (2), 113-116.
44. Galonić Fujimori, D.; Barr, E. W.; Matthews, M. L.; Koch, G. M.; Yonce, J. R.; Walsh, C. T.; Bollinger, J. M., Jr.; Krebs, C.; Riggs-Gelasco, P. J., Spectroscopic Evidence for a High-Spin Br-Fe(IV)-Oxo Intermediate in the α-Ketoglutarate-Dependent Halogenase CytC3 from Streptomyces. *J. Am. Chem. Soc.* **2007,** *129* (44), 13408-13409.

45. Bigi, J. P.; Harman, W. H.; Lassalle-Kaiser, B.; Robles, D. M.; Stich, T. A.; Yano, J.; Britt, R. D.; Chang, C. J., A high-spin iron(IV)-oxo complex supported by a trigonal nonheme pyrrolide platform. *J. Am. Chem. Soc.* **2012,** *134* (3), 1536-1542.
46. England, J.; Guo, Y.; Van Heuvelen, K. M.; Cranswick, M. A.; Rohde, G. T.; Bominaar, E. L.; Münck, E.; Que, L., Jr., A more reactive trigonal-bipyramidal high-spin oxoiron(IV) complex with a cis-labile site. *J. Am. Chem. Soc.* **2011,** *133* (31), 11880-11883.
47. Kass, D.; Corona, T.; Warm, K.; Braun-Cula, B.; Kuhlmann, U.; Bill, E.; Mebs, S.; Swart, M.; Dau, H.; Haumann, M.; Hildebrandt, P.; Ray, K., Stoichiometric Formation of an Oxoiron(IV) Complex by a Soluble Methane Monooxygenase Type Activation of O_2 at an Iron(II)-Cyclam Center. *J. Am. Chem. Soc.* **2020,** *142* (13), 5924-5928.
48. Rohde, J. U.; In, J. H.; Lim, M. H.; Brennessel, W. W.; Bukowski, M. R.; Stubna, A.; Münck, E.; Nam, W.; Que, L., Jr., Crystallographic and spectroscopic characterization of a nonheme Fe(IV)-O complex. *Science* **2003,** *299* (5609), 1037-1039.
49. Schaub, S.; Miska, A.; Becker, J.; Zahn, S.; Mollenhauer, D.; Sakshath, S.; Schunemann, V.; Schindler, S., Synthesis of an Iron(IV) Aqua-Oxido Complex Using Ozone as an Oxidant. *Angew. Chem. Int. Ed.* **2018,** *57* (19), 5355-5358.
50. Thibon, A.; England, J.; Martinho, M.; Young, V. G., Jr.; Frisch, J. R.; Guillot, R.; Girerd, J. J.; Münck, E.; Que, L., Jr.; Banse, F., Proton- and reductant-assisted dioxygen activation by a nonheme iron(II) complex to form an oxoiron(IV) intermediate. *Angew. Chem. Int. Ed.* **2008,** *47* (37), 7064-7067.
51. England, J.; Bigelow, J. O.; Van Heuvelen, K. M.; Farquhar, E. R.; Martinho, M.; Meier, K. K.; Frisch, J. R.; Münck, E.; Que, L., Jr., An Ultra-Stable Oxoiron(IV) Complex and Its Blue Conjugate Base. *Chem. Sci.* **2014,** *5* (3), 1204-1215.
52. Meyer, S.; Klawitter, I.; Demeshko, S.; Bill, E.; Meyer, F., A tetracarbene-oxoiron(IV) complex. *Angew. Chem. Int. Ed.* **2013,** *52* (3), 901-905.
53. Kaizer, J.; Klinker, E. J.; Oh, N. Y.; Rohde, J.-U.; Song, W. J.; Stubna, A.; Kim, J.; Münck, E.; Nam, W.; Que, L., Jr., Nonheme $Fe^{IV}O$ Complexes That Can Oxidize the C-H Bonds of Cyclohexane at Room Temperature. *J. Am. Chem. Soc.* **2004,** *126* (2), 472-473.
54. Sahu, S.; Zhang, B.; Pollock, C. J.; Durr, M.; Davies, C. G.; Confer, A. M.; Ivanovic-Burmazovic, I.; Siegler, M. A.; Jameson, G. N.; Krebs, C.; Goldberg, D. P., Aromatic C-F Hydroxylation by Nonheme Iron(IV)-Oxo Complexes: Structural, Spectroscopic, and Mechanistic Investigations. *J. Am. Chem. Soc.* **2016,** *138* (39), 12791-12802.
55. Prakash, J.; Rohde, G. T.; Meier, K. K.; Münck, E.; Que, L., Jr., Upside Down! Crystallographic and Spectroscopic Characterization of an $[Fe^{IV}(O_{syn})(TMC)]^{2+}$ Complex. *Inorg. Chem.* **2015,** *54* (23), 11055-11057.
56. Rasheed, W.; Fan, R.; Abelson, C. S.; Peterson, P. O.; Ching, W. M.; Guo, Y.; Que, L., Jr., Structural implications of the paramagnetically shifted NMR signals from pyridine H atoms on synthetic nonheme Fe(IV)=O complexes. *J. Biol. Inorg. Chem.* **2019,** *24* (4), 533-545.
57. Bukowski, M. R.; Koehntop, K. D.; Stubna, A.; Bominaar, E. L.; Halfen, J. A.; Münck, E.; Nam, W.; Que, L., Jr., A thiolate-ligated nonheme oxoiron(IV) complex relevant to cytochrome P450. *Science* **2005,** *310* (5750), 1000-1002.
58. Roach, P. L.; Clifton, I. J.; Fülöp, V.; Harlos, K.; Barton, G. J.; Hajdu, J.; Andersson, I.; Schofield, C. J.; Baldwin, J. E., Crystal Structure of Isopenicillin *N* Synthase is the First From a New Structural Family of Enzymes. *Nature* **1995,** *375*, 700-704.
59. Denisov, I. G.; Makris, T. M.; Sligar, S. G.; Schlichting, I., Structure and chemistry of cytochrome P450. *Chem. Rev.* **2005,** *105* (6), 2253-2277.
60. Grapperhaus, C. A.; Mienert, B.; Bill, E.; Weyhermuller, T.; Wieghardt, K., Mononuclear (nitrido)iron(V) and (oxo)iron(IV) complexes via photolysis of [(cyclam-acetato)$Fe^{III}(N_3)$]+ and

ozonolysis of [(cyclam-acetato)$Fe^{III}(O_3SCF_3)$]+ in water/acetone mixtures. *Inorg. Chem.* **2000,** *39* (23), 5306-5317.
61. Chanda, A.; Shan, X.; Chakrabarti, M.; Ellis, W. C.; Popescu, D. L.; Tiago de Oliveira, F.; Wang, D.; Que, L., Jr.; Collins, T. J.; Münck, E.; Bominaar, E. L., (TAML)Fe^{IV}=O complex in aqueous solution: synthesis and spectroscopic and computational characterization. *Inorg. Chem.* **2008,** *47* (9), 3669-3678.
62. Kim, J.; Dong, Y.; Larka, E.; Que, L., Jr., Electrospray Inonization Mass Spectral Characterization of Transient Iron Species of Bioinorganic Relevance. *Inorg. Chem.* **1996,** *35*, 2369-2372.
63. Kim, C.; Chen, K.; Kim, J.; Que, L., Jr., Stereospecific Alkane Hydroxylation with H_2O_2 Catalyzed by an Iron(II)-Tris(2-pyridylmethyl)amine Complex. *J. Am. Chem. Soc.* **1997,** *119*, 5964-5965.
64. Ho, R. Y. N.; Roelfes, G.; Feringa, B. L.; Que, L., Jr., Raman Evidence for a Weakened O-O Bond in Mononuclear Low-Spin Iron(III)-Hydroperoxides. *J. Am. Chem. Soc.* **1999,** *121*, 264-265.
65. Tiago de Oliveira, F.; Chanda, A.; Banerjee, D.; Shan, X.; Mondal, S.; Que, L., Jr.; Bominaar, E. L.; Münck, E.; Collins, T. J., Chemical and Spectroscopic Evidence for an Fe^{V}-Oxo Complex. *Science* **2007,** *315* (5813), 835-838.
66. Prat, I.; Mathieson, J. S.; Güell, M.; Ribas, X.; Luis, J. M.; Cronin, L.; Costas, M., Observation of Fe(V)=O using Variable Temperature Mass Spectrometry and its Enzyme-like C-H and C=C Oxidation Reactions. *Nature Chem.* **2011,** *3*, 788-793.
67. Xu, S.; Veach, J. J.; Oloo, W. N.; Peters, K. C.; Wang, J.; Perry, R. H.; Que, L., Jr., Detection of a Transient Fe^{V}(O)(OH) Species Involved in Olefin Oxidation by a Bio-Inspired Non-Haem Iron Catalyst. *Chem. Commun.* **2018,** *54* (63), 8701-8704.
68. Borrell, M.; Andris, E.; Navrátil, R.; Roithová, J.; Costas, M., Characterized *cis*-Fe^{V}(O)(OH) intermediate mimics enzymatic oxidations in the gas phase. *Nat. Commun.* **2019,** *10*, 901.
69. Hitomi, Y.; Arakawa, K.; Funabiki, T.; Kodera, M., An Iron(III)–Monoamidate Complex Catalyst for Selective Hydroxylation of Alkane CH Bonds with Hydrogen Peroxide. *Angew. Chem. Int. Ed.* **2012,** *51*, 3448-3452.
70. Ghosh, M.; Singh, K. K.; Panda, C.; Weitz, A.; Hendrich, M. P.; Collins, T. J.; Dhar, B. B.; Gupta, S. S., Formation of a Room Temperature Stable Fe^{V}(O) Complex: Reactivity Toward Unactivated C−H Bonds. *J. Am. Chem. Soc.* **2014,** *136*, 9524-9527.
71. Xue, S.-S.; Li, X.-X.; Lee, Y.-M.; Seo, M. S.; Kim, Y.; Yanagisawa, S.; Kubo, M.; Jeon, Y.-K.; Kim, W.-S.; Sarangi, R.; Kim, S. H.; Fukuzumi, S.; Nam, W., Enhanced Redox Reactivity of a Nonheme Iron(V)–Oxo Complex Binding Proton. *J. Am. Chem. Soc.* **2020,** *142* (36), 15305-15319.
72. Van Heuvelen, K. M.; Fiedler, A. T.; Shan, X.; De Hont, R. H.; Meier, K. K.; Bominaar, E. L.; Münck, E.; Que, L., Jr., One-electron oxidation of an oxoiron(IV) complex to form an [O═Fe^{V}═NR] center. *Proc. Natl. Acad. Sci. U.S.A.* **2012,** *109* (30), 11933-11938.
73. Zima, A. M.; Lyakin, O. Y.; Bushmin, D. S.; Soshnikov, I. E.; Bryliakov, K. P.; Talsi, E. P., Non-heme perferryl intermediates: Effect of spin state on the epoxidation enantioselectivity. *Mol. Catal.* **2021,** *502*, 111403.
74. Zima, A. M.; Lyakin, O. Y.; Bryliakov, K. P.; Talsi, E. P., High-Spin and Low-Spin Perferryl Intermediates in Fe(PDP)-Catalyzed Epoxidations. *ChemCatChem* **2019,** *11* (21), 5345-5352.
75. Xu, S.; Draksharapu, A.; Rasheed, W.; Que, L., Jr., Acid pK_a Dependence in O–O Bond Heterolysis of a Nonheme Fe^{III}–OOH Intermediate to Form a Potent Fe^{V}=O Oxidant with Heme Compound I-Like Reactivity. *J. Am. Chem. Soc.* **2019,** *141* (40), 16093-16107.
76. Bollinger, J. M., Jr.; Edmondson, D. E.; Huynh, B. H.; Filley, J.; Norton, J.; Stubbe, J., Mechanism of assembly of the tyrosyl radical-dinuclear iron cluster cofactor of ribonucleotide reductase. *Science* **1991,** *253* (5017), 292-298.

77. Liu, K. E.; Valentine, A. M.; Wang, D.; Huynh, B. H.; Edmondson, D. E.; Salifoglou, A.; Lippard, S. J., Kinetic and Spectroscopic Characterization of Intermediates and Component Interactions in Reactions of Methane Monooxygenase from *Methylococcus capsulatus* (Bath). *J. Am. Chem. Soc.* **1995,** *117*, 10174-10185.
78. Ghosh, A.; Tiago de Oliveira, F.; Yano, T.; Nishioka, T.; Beach, E. S.; Kinoshita, I.; Münck, E.; Ryabov, A. D.; Horwitz, C. P.; Collins, T. J., Catalytically Active μ-Oxodiiron(IV) Oxidants from Iron(III) and Dioxygen. *J. Am. Chem. Soc.* **2005,** *127*, 2505-2513.
79. Dong, Y.; Fujii, H.; Hendrich, M. P.; Leising, R. A.; Pan, G.; Randall, C. R.; Wilkinson, E. C.; Zang, Y.; Que, L., Jr.; Fox, B. G.; Kauffmann, K.; Münck, E., A High-Valent Nonheme Iron Intermediate. Structure and Properties of $[Fe_2(\mu\text{-}O)_2(5\text{-}Me\text{-}TPA)_2](ClO_4)_3$. *J. Am. Chem. Soc.* **1995,** *117*, 2778-2792.
80. Wilkinson, E. C.; Dong, Y.; Zang, Y.; Fujii, H.; Fraczkiewicz, R.; Fraczkiewicz, G.; Czernuszewicz, R. S.; Que, L., Jr., Raman Signature of the Fe_2O_2 'Diamond' Core. *J. Am. Chem. Soc.* **1998,** *120*, 955-962.
81. Hsu, H.-F.; Dong, Y.; Shu, L.; Young, V. G., Jr.; Que, L., Jr., Crystal Structure of a Synthetic High-Valent Complex with an $Fe_2(\mu\text{-}O)_2$ Diamond Core. Implications for the Core Structures of Methane Monooxygenase Intermediate **Q** and Ribonucleotide Reductase Intermediate **X**. *J. Am. Chem. Soc.* **1999,** *121*, 5230-5237.
82. Kryatov, S. V.; Taktak, S.; Korendovych, I. V.; Rybak-Akimova, E. V.; Kaizer, J.; Torelli, S.; Shan, X.; Mandal, S.; MacMurdo, V. L.; Mairata i Payeras, A.; Que, L., Jr., Dioxygen Binding to Complexes with $Fe^{II}2(\mu\text{-}OH)_2$ Cores: Steric Control of Activation Barriers and O_2-Adduct Formation. *Inorg. Chem.* **2005,** *44* (1), 85-99.
83. Cranswick, M. A.; Meier, K. K.; Shan, X.; Stubna, A.; Kaizer, J.; Mehn, M. P.; Münck, E.; Que, L., Jr., Protonation of a Peroxodiiron(III) Complex and Conversion to a Diiron(III/IV) Intermediate: Implications for Proton-Assisted O−O Bond Cleavage in Nonheme Diiron Enzymes. *Inorg. Chem.* **2012,** *51* (19), 10417-10426.
84. MacMurdo, V. L.; Zheng, H.; Que, L., Jr., Model for the Cofactor Formation Reaction of E. Coli Ribonucleotide Reductase. From a Diiron(II) Precursor to an $Fe^{III}Fe^{IV}$ Species via a Peroxo Intermediate. *Inorg. Chem.* **2000,** *39*, 2254-2255.
85. Kodera, M.; Kawahara, Y.; Hitomi, Y.; Nomura, T.; Ogura, T.; Kobayashi, Y., Reversible O−O Bond Scission of Peroxodiiron(III) to High-Spin Oxodiiron(IV) in Dioxygen Activation of a Diiron Center with a Bistpa Dinucleating Ligand as a Soluble Methane Monooxygenase Model. *J. Am. Chem. Soc.* **2012,** *134* (32), 13236-13239.
86. Xue, G.; Fiedler, A. T.; Martinho, M.; Münck, E.; Que, L., Jr., Insights into the P-to-Q Conversion in the Catalytic Cycle of Methane Monooxygenase from a Synthetic Model System. *Proc. Natl. Acad. Sci. U.S.A.* **2008,** *105* (52), 20615-20620.
87. Stoian, S. A.; Xue, G.; Bominaar, E. L.; Que, L., Jr.; Münck, E., Spectroscopic and Theoretical Investigation of a Complex with a $[O{=}Fe^{IV}{-}O{-}Fe^{IV}{=}O]$ Core Related to Methane Monooxygenase Intermediate Q. *J. Am. Chem. Soc.* **2014,** *136* (4), 1545-1558.
88. Xue, G.; De Hont, R.; Münck, E.; Que, L., Jr., Million-fold activation of the $[Fe_2(\mu\text{-}O)_2]$ diamond core for C–H bond cleavage. *Nature Chem.* **2010,** *2* (5), 400-405.
89. Xue, G.; Pokutsa, A.; Que, L., Jr., Substrate-Triggered Activation of a Synthetic $[Fe_2(\mu\text{-}O)_2]$ Diamond Core for C–H Bond Cleavage. *J. Am. Chem. Soc.* **2011,** *133* (41), 16657–16667.
90. Xue, G.; Geng, C.; Ye, S.; Fiedler, A. T.; Neese, F.; Que, L., Jr., Hydrogen-Bonding Effects on the Reactivity of $[X{-}Fe^{III}{-}O{-}Fe^{IV}{=}O]$ (X = OH, F) Complexes toward C−H Bond Cleavage. *Inorg. Chem.* **2013,** *52* (7), 3976-3984.

91. Draksharapu, A.; Xu, S.; Que, L., Jr., Ce(IV)- and $HClO_4$-Promoted Assembly of an $Fe_2(IV)(\mu\text{-}O)_2$ Diamond Core from its Monomeric Fe(IV)=O Precursor at Room Temperature. *Angew. Chem. Int. Ed.* **2020,** *59* (50), 22484-22488.
92. Xue, G.; Wang, D.; De Hont, R.; Fiedler, A. T.; Shan, X.; Münck, E.; Que, L., Jr., A Synthetic Precedent for the $[Fe^{IV}2(\mu\text{-}O)_2]$ Diamond Core Proposed for Methane Monooxygenase Intermediate Q. *Proc. Natl. Acad. Sci. U.S.A.* **2007,** *104* (52), 20713-20718.
93. Rohde, G. T.; Xue, G.; Que, L., Jr., Explorations of the nonheme high-valent iron-oxo landscape: crystal structure of a synthetic complex with an $[Fe^{IV}2(\mu\text{-}O)_2]$ diamond core relevant to the chemistry of sMMOH. *Faraday Discuss.* **2022,** *234* (0), 109-128.
94. Huang, X.; Groves, J. T., Beyond ferryl-mediated hydroxylation: 40 years of the rebound mechanism and C–H activation. *J. Biol. Inorg. Chem.* **2017,** *22*, 185-207.
95. Brausam, A.; Eigler, S.; Jux, N.; van Eldik, R., Mechanistic Investigations of the Reaction of an Iron(III) Octa-Anionic Porphyrin Complex with Hydrogen Peroxide and the Catalyzed Oxidation of Diammonium-2,2'-azinobis(3-ethylbenzothiazoline-6-sulfonate). *Inorg. Chem.* **2009,** *48* (16), 7667-7678.
96. Hölzl, S. M.; Altmann, P. J.; Kück, J. W.; Kühn, F. E., Speciation in iron epoxidation catalysis: A perspective on the discovery and role of non-heme iron(III)-hydroperoxo species in iron-catalyzed oxidation reactions. *Coord. Chem. Rev.* **2017,** *352*, 517-536.
97. Martinho, M.; Dorlet, P.; Rivière, E.; Thibon, A.; Ribal, C.; Banse, F.; Girerd, J.-J., Preparation and Characterization of a Microcrystalline Non-Heme Fe^{III}(OOH) Complex Powder: EPR Reinvestigation of Fe^{III}(OOH) Complexes — Improvement of the Perturbation Equations for the g Tensor of Low-Spin Fe^{III}. *Chem. Eur. J.* **2008,** *14* (10), 3182-3188.
98. Simaan, A. J.; Döpner, S.; Banse, F.; Bourcier, S.; Bouchoux, G.; Boussac, A.; Hildebrandt, P.; Girerd, J.-J., Fe^{III}-Hydroperoxo and Peroxo Complexes with Aminopyridyl Ligands and the Resonance Raman Spectroscopic Identification of the Fe-O and O-O Stretching Modes. *Eur. J. Inorg. Chem.* **2000,** *2000* (7), 1627-1633.
99. Kal, S.; Draksharapu, A.; Que, L., Jr., Sc^{3+} (or $HClO_4$) activation of a nonheme Fe^{III}–OOH intermediate for the rapid hydroxylation of cyclohexane and benzene. *J. Am. Chem. Soc.* **2018,** *140* (17), 5798-5804.
100. Costas, M.; Mehn, M. P.; Jensen, M. P.; Que, L., Jr., Oxygen Activation at Mononuclear Nonheme Iron: Enzymes, Intermediates, and Models. *Chem. Rev.* **2004,** *104* (2), 939-986.
101. Eckert, F.; Leito, I.; Kaljurand, I.; Kütt, A.; Klamt, A.; Diedenhofen, M., Prediction of acidity in acetonitrile solution with COSMO-RS. *J. Comput. Chem.* **2009,** *30* (5), 799-810.
102. Kütt, A.; Tshepelevitsh, S.; Saame, J.; Lõkov, M.; Kaljurand, I.; Selberg, S.; Leito, I., Strengths of Acids in Acetonitrile. *Eur. J. Org. Chem.* **2021,** *2021* (9), 1407-1419.
103. Que, L., Jr., Metalloproteins with phenolate coordination. *Coord. Chem. Rev.* **1983,** *50* (1), 73-108.
104. Thibon, A.; Jollet, V.; Ribal, C.; Sénéchal-David, K.; Billon, L.; Sorokin, A. B.; Banse, F., Hydroxylation of Aromatics with the Help of a Non-Haem FeOOH: A Mechanistic Study under Single-Turnover and Catalytic Conditions. *Chem. Eur. J.* **2012,** *18* (9), 2715–2724.
105. Liu, L. V.; Hong, S.; Cho, J.; Nam, W.; Solomon, E. I., Comparison of High-Spin and Low-Spin Nonheme Fe^{III}–OOH Complexes in O−O Bond Homolysis and H-Atom Abstraction Reactivities. *J. Am. Chem. Soc.* **2013,** *135* (8), 3286-3299.
106. Zhang, Q.; Goldsmith, C. R., Kinetic Analysis of the Formation and Decay of a Non-Heme Ferric Hydroperoxide Species Susceptible to O–O Bond Homolysis. *Inorg. Chem.* **2014,** *53* (10), 5206-5211.

107. Kaizer, J.; Costas, M.; Que, L., Jr., A Dramatic Push Effect on the Homolysis of Fe^{III}(OOR) Intermediates To Form Nonheme Fe^{IV}=O Complexes. *Angew. Chem. Int. Ed.* **2003,** *42* (31), 3671-3673.
108. Mairata i Payeras, A.; Ho, R. Y. N.; Fujita, M.; Que, L., Jr., The Reaction of [Fe^{II}(tpa)] with H_2O_2 in Acetonitrile and Acetone—Distinct Intermediates and Yet Similar Catalysis. *Chem. Eur. J.* **2004,** *10* (20), 4944-4953.
109. Oloo, W. N.; Fielding, A. J.; Que, L., Jr., Rate Determining Water-Assisted O–O Bond Cleavage of a Fe^{III}–OOH Intermediate in a Bio-inspired Nonheme Iron-Catalyzed Oxidation. *J. Am. Chem. Soc.* **2013,** *135* (17), 6438-6441.
110. Serrano-Plana, J.; Acuña-Parés, F.; Dantignana, V.; Oloo, W. N.; Castillo, E.; Draksharapu, A.; Whiteoak, C. J.; Martin-Diaconsescu, V.; Basallote, M. G.; Luis, J. M.; Que, L., Jr.; Costas, M.; Company, A., Acid-triggered O–O bond heterolysis of a nonheme Fe^{III}(OOH) species for the stereospecific hydroxylation of strong C–H bonds. *Chem. Eur. J.* **2018,** *24* (20), 5331-5340.
111. Li, F.; Meier, K. K.; Cranswick, M. A.; Chakrabarti, M.; Van Heuvelen, K. M.; Münck, E.; Que, L., Jr., Characterization of a High-Spin Nonheme Fe^{III}–OOH Intermediate and Its Quantitative Conversion to an Fe^{IV}=O Complex. *J. Am. Chem. Soc.* **2011,** *133* (19), 7256–7259.
112. Olah, G. A., Aromatic substitution. XXVIII. Mechanism of electrophilic aromatic substitutions. *Acc. Chem. Res.* **1971,** *4* (7), 240-248.
113. Kal, S.; Xu, S.; Que, L., Jr., Bio-inspired Nonheme Iron Oxidation Catalysis: Involvement of Oxoiron(V) Oxidants in Cleaving Strong C-H Bonds. *Angew. Chem. Int. Ed.* **2020,** *59* (19), 7332-7349.
114. Lie, T. J.; Pitta, T.; Leadbetter, E. R.; Godchaux III, W.; Leadbetter, J. R., Sulfonates: novel electron acceptors in anaerobic respiration. *Arch. Microbiol.* **1996,** *166* (3), 204-210.
115. Laue, H.; Denger, K.; Cook, A. M., Taurine reduction in anaerobic respiration of Bilophila wadsworthia RZATAU. *Appl. Environ. Microbiol.* **1997,** *63* (5), 2016-2021.
116. Sahu, S.; Quesne, M. G.; Davies, C. G.; Durr, M.; Ivanovic-Burmazovic, I.; Siegler, M. A.; Jameson, G. N.; de Visser, S. P.; Goldberg, D. P., Direct observation of a nonheme iron(IV)-oxo complex that mediates aromatic C-F hydroxylation. *J. Am. Chem. Soc.* **2014,** *136* (39), 13542-13545.
117. Dogutan, D. K.; McGuire, R., Jr.; Nocera, D. G., Electocatalytic Water Oxidation by Cobalt(III) Hangman β-Octafluoro Corroles. *J. Am. Chem. Soc.* **2011,** *133* (24), 9178-9180.
118. Dunford, H. B.; Hewson, W. D.; Steiner, H., Horseradish peroxidase. XXIX. Reactions in water and deuterium oxide: cyanide binding, compound I formation, and reactions of compounds I and II with ferrocyanide. *Can. J. Chem.* **1978,** *56* (22), 2844–2852.
119. Lee, S.-K.; Lipscomb, J. D., Oxygen Activation Catalyzed by Methane Monooxygenase Hydroxylase Component: Proton Delivery during the O-O Bond Cleavage Steps. *Biochemistry* **1999,** *38* (14), 4423-4432.
120. Tinberg, C. E.; Lippard, S. J., Revisiting the Mechanism of Dioxygen Activation in Soluble Methane Monooxygenase from M. capsulatus (Bath): Evidence for a Multi-Step, Proton-Dependent Reaction Pathway. *Biochemistry* **2009,** *48* (51), 12145–12158.
121. Grave, K.; Torren-Edo, J.; Muller, A.; Greko, C.; Moulin, G.; Mackay, D.; Group, E., Variations in the sales and sales patterns of veterinary antimicrobial agents in 25 European countries. *J. Antimicrob. Chemother.* **2014,** *69* (8), 2284-2291.
122. Daughton, C. G.; Ruhoy, I. S., Environmental footprint of pharmaceuticals: the significance of factors beyond direct excretion to sewers. *Environ. Toxicol. Chem.* **2009,** *28* (12), 2495-2521.
123. Deng, Y.; Li, B.; Zhang, T., Bacteria that make a meal of sulfonamide antibiotics: blind spots and emerging opportunities. *Environ. Sci. Technol.* **2018,** *52* (7), 3854-3868.

124. Bengtsson-Palme, J.; Larsson, D. J., Concentrations of antibiotics predicted to select for resistant bacteria: proposed limits for environmental regulation. *Environ. Int.* **2016,** *86*, 140-149.
125. Andersson, D. I.; Hughes, D., Antibiotic resistance and its cost: is it possible to reverse resistance? *Nat. Rev. Microbiol.* **2010,** *8* (4), 260-271.
126. Ricken, B.; Kolvenbach, B. A.; Bergesch, C.; Benndorf, D.; Kroll, K.; Strnad, H.; Vlček, Č.; Adaixo, R.; Hammes, F.; Shahgaldian, P., FMNH2-dependent monooxygenases initiate catabolism of sulfonamides in Microbacterium sp. strain BR1 subsisting on sulfonamide antibiotics. *Sci. Rep.* **2017,** *7* (1), 1-11.
127. Oberoi, A. S.; Jia, Y.; Zhang, H.; Khanal, S. K.; Lu, H., Insights into the fate and removal of antibiotics in engineered biological treatment systems: a critical review. *Environ. Sci. Technol.* **2019,** *53* (13), 7234-7264.
128. Nunes, O. C.; Manaia, C. M.; Kolvenbach, B. A.; Corvini, P. F.-X., Living with sulfonamides: a diverse range of mechanisms observed in bacteria. *Appl. Microbiol. Biotechnol.* **2020,** *104* (24), 10389-10408.
129. Cook, A. M.; Laue, H.; Junker, F., Microbial desulfonation. *FEMS Microbiol. Rev.* **1998,** *22* (5), 399-419.
130. Kelly, D. P.; Baker, S. C.; Trickett, J.; Davey, M.; Murrell, J. C., Methanesulphonate utilization by a novel methylotrophic bacterium involves an unusual monooxygenase. *Microbiology* **1994,** *140* (6), 1419-1426.
131. Higgins, T. P.; Davey, M.; Trickett, J.; Kelly, D. P.; Murrell, J. C., Metabolism of methanesulfonic acid involves a multicomponent monooxygenase enzyme. *Microbiology* **1996,** *142* (2), 251-260.
132. Wang, S.; Wang, J., Biodegradation and metabolic pathway of sulfamethoxazole by a novel strain Acinetobacter sp. *Appl. Microbiol. Biotechnol.* **2018,** *102* (1), 425-432.
133. Mulla, S. I.; Hu, A.; Sun, Q.; Li, J.; Suanon, F.; Ashfaq, M.; Yu, C.-P., Biodegradation of sulfamethoxazole in bacteria from three different origins. *J. Environ. Manage.* **2018,** *206*, 93-102.
134. Moonen, M. J.; Synowsky, S. A.; van den Berg, W. A.; Westphal, A. H.; Heck, A. J.; van den Heuvel, R. H.; Fraaije, M. W.; van Berkel, W. J., Hydroquinone dioxygenase from Pseudomonas fluorescens ACB: a novel member of the family of nonheme-iron (II)-dependent dioxygenases. *J. Bacteriol.* **2008,** *190* (15), 5199-5209.
135. Trehoux, A.; Mahy, J.-P.; Avenier, F., A growing family of O_2 activating dinuclear iron enzymes with key catalytic diiron(III)-peroxo intermediates: Biological systems and chemical models. *Coord. Chem. Rev.* **2016,** *322*, 142-158.
136. Cotruvo, J. A.; Stubbe, J., Class I Ribonucleotide Reductases: Metallocofactor Assembly and Repair In Vitro and In Vivo. *Annu. Rev. Biochem.* **2011,** *80*, 733-767.
137. Price, J. C.; Barr, E. W.; Glass, T. E.; Krebs, C.; Bollinger, J. M., Jr., Evidence for Hydrogen Abstraction from C_1 of Taurine by the High-Spin Fe(IV) Intermediate Detected during Oxygen Activation by Taurine:α-Ketoglutarate Dioxygenase (TauD). *J. Am. Chem. Soc.* **2003,** *125* (43), 13008-13009.
138. Zang, Y.; Dong, Y.; Que, L., Jr.; Kauffmann, K.; Münck, E., The First Bis(μ-oxo)diiron(III) Complex. Structure and Magnetic Properties of $[Fe_2(\mu\text{-}O)_2(6TLA)_2](ClO_4)_2$. *J. Am. Chem. Soc.* **1995,** *117* (3), 1169-1170.
139. Banerjee, S. Structure and Reactivity of Mono- and Diiron Synthetic Models of Nonheme Iron-containing Enzymes. Ph.D. Thesis, University of Minnesota, Minneapolis, MN, 2020.
140. Zang, Y.; Kim, J.; Dong, Y.; Wilkinson, E. C.; Appelman, E. H.; Que, L., Jr., Models for Nonheme Iron Intermediates: Structural Basis for Tuning the Spin States of Fe(TPA) Complexes. *J. Am. Chem. Soc.* **1997,** *119*, 4197-4205.

141. Kitajima, N.; Tamura, N.; Tanaka, M.; Moro-oka, Y., Synthesis and Molecular Structure of Diferrous Complexes Containing a Bis(hydroxo) or a Hydroxo Carboxylato Bridge. *Inorg. Chem.* **1992,** *31*, 3342-3343.
142. Stubna, A.; Jo, D.-H.; Costas, M.; Brenessel, W. W.; Andres, H.; Bominaar, E. L.; Münck, E.; Que, L., Jr., A Structural and Mössbauer Study of Complexes with $Fe_2(\mu\text{-}O(H))_2$ Cores: Stepwise Oxidation from $Fe^{II}(\mu\text{-}OH)_2Fe^{II}$ through $Fe^{II}(\mu\text{-}OH)_2Fe^{III}$ to $Fe^{III}(\mu\text{-}O)(\mu\text{-}OH)Fe^{III}$. *Inorg. Chem.* **2004,** *43* (10), 3067-3079.
143. Dong, Y.; Zang, Y.; Shu, L.; Wilkinson, E. C.; Que, L., Jr. ; Kauffmann, K.; Münck, E., Models for Nonheme Diiron Enzymes. Assembly of a High-Valent Fe_2O_2 Diamond Core from Its Peroxo Precursor. *J. Am. Chem. Soc.* **1997,** *119*, 12683-12684.
144. Zheng, H.; Zang, Y.; Dong, Y.; Young, V. G., Jr.; Que, L., Jr., Complexes with $Fe^{III}2(\mu\text{-}O)(\mu\text{-}OH)$, $Fe^{III}2(\mu\text{-}O)_2$, and $Fe^{III}3(\mu\text{-}O)_3$ Cores: Structures, Spectroscopy, and Core Interconversions. *J. Am. Chem. Soc.* **1999,** *121*, 2226-2235.
145. Zang, Y.; Pan, G.; Que, L., Jr.; Fox, B. G.; Münck, E., First Diferric Complex with an $Fe_2(\mu\text{-}O)(\mu\text{-}OH)$ Core. Structure and Reactivity of $[Fe_2(\mu\text{-}O)(\mu\text{-}OH)(6TLA)_2](ClO_4)_3$. *J. Am. Chem. Soc.* **1994,** *116*, 3653-3654.
146. Do, L. H.; Xue, G.; Que, L., Jr.; Lippard, S. J., Evaluating the Identity and Diiron Core Transformations of a (μ-Oxo)diiron(III) Complex Supported by Electron-Rich Tris(pyridyl-2-methyl)amine Ligands. *Inorg. Chem.* **2012,** *51* (4), 2393-2402.
147. Fiedler, A. T.; Shan, X.; Mehn, M. P.; Kaizer, J.; Torelli, S.; Frisch, J. R.; Kodera, M.; Que, L., Jr., Spectroscopic and Computational Studies of (μ-Oxo)(μ-1,2-Peroxo)diiron(III) Complexes of Relevance to Nonheme Diiron Oxygenase Intermediates. *J. Phys. Chem. A* **2008,** *112* (50), 13037-13044.
148. Zhang, X.; Furutachi, H.; Fujinami, S.; Nagatomo, S.; Maeda, Y.; Watanabe, Y.; Kitagawa, T.; Suzuki, M., Structural and Spectroscopic Characterization of (μ-Hydroxo or μ-Oxo)(μ-peroxo)diiron(III) Complexes: Models for Peroxo Intermediates of Non-Heme Diiron Proteins. *J. Am. Chem. Soc.* **2005,** *127*, 826-827.
149. Hegg, E. L.; Que, L., Jr., The 2-His-1-Carboxylate Facial Triad: An Emerging Structural Motif in Mononuclear Non-Heme Iron(II) Enzymes. *Eur. J. Biochem.* **1997,** *250*, 625-629.
150. Marsh, R. E.; Schomaker, V.; Herbstein, F. H., Arrays with local centers of symmetry in space groups Pca21 and Pna21. *Acta Cryst.* **1998,** *54* (6), 921-924.
151. Jackson, T. A.; Rohde, J. U.; Seo, M. S.; Sastri, C. V.; DeHont, R.; Stubna, A.; Ohta, T.; Kitagawa, T.; Münck, E.; Nam, W.; Que, L., Jr., Axial ligand effects on the geometric and electronic structures of nonheme oxoiron(IV) complexes. *J. Am. Chem. Soc.* **2008,** *130* (37), 12394-12407.
152. Bigelow, J. O.; England, J.; Klein, J. E.; Farquhar, E. R.; Frisch, J. R.; Martinho, M.; Mandal, D.; Munck, E.; Shaik, S.; Que, L., Jr., Oxoiron(IV) Tetramethylcyclam Complexes with Axial Carboxylate Ligands: Effect of Tethering the Carboxylate on Reactivity. *Inorg. Chem.* **2017,** *56* (6), 3287-3301.
153. Klein, J. E. M. N.; Draksharapu, A.; Shokri, A.; Cramer, C. J.; Que, L., Jr., On the Lewis Acidity of the Oxoiron(IV) Unit in a Tetramethylcyclam Complex. *Chem. Eur. J.* **2018,** *24* (20), 5373-5378.
154. Bell, C. B., 3rd; Wong, S. D.; Xiao, Y.; Klinker, E. J.; Tenderholt, A. L.; Smith, M. C.; Rohde, J. U.; Que, L., Jr.; Cramer, S. P.; Solomon, E. I., A combined NRVS and DFT study of Fe(IV)=O model complexes: a diagnostic method for the elucidation of non-heme iron enzyme intermediates. *Angew. Chem. Int. Ed.* **2008,** *47* (47), 9071-9074.
155. Wang, D.; Ray, K.; Collins, M. J.; Farquhar, E. R.; Frisch, J. R.; Gómez, L.; Jackson, T. A.; Kerscher, M.; Waleska, A.; Comba, P.; Costas, M.; Que, L., Nonheme oxoiron(IV) complexes of

pentadentate N5 ligands: spectroscopy, electrochemistry, and oxidative reactivity. *Chem. Sci.* **2013,** *4* (1), 282-291.
156. Mitra, M.; Nimir, H.; Demeshko, S.; Bhat, S. S.; Malinkin, S. O.; Haukka, M.; Lloret-Fillol, J.; Lisensky, G. C.; Meyer, F.; Shteinman, A. A.; Browne, W. R.; Hrovat, D. A.; Richmond, M. G.; Costas, M.; Nordlander, E., Nonheme Fe(IV) Oxo Complexes of Two New Pentadentate Ligands and Their Hydrogen-Atom and Oxygen-Atom Transfer Reactions. *Inorg. Chem.* **2015,** *54* (15), 7152-7164.
157. Rana, S.; Biswas, J. P.; Sen, A.; Clemancey, M.; Blondin, G.; Latour, J. M.; Rajaraman, G.; Maiti, D., Selective C-H halogenation over hydroxylation by non-heme iron(iv)-oxo. *Chem. Sci.* **2018,** *9* (40), 7843-7858.
158. Chantarojsiri, T.; Sun, Y.; Long, J. R.; Chang, C. J., Water-Soluble Iron(IV)-Oxo Complexes Supported by Pentapyridine Ligands: Axial Ligand Effects on Hydrogen Atom and Oxygen Atom Transfer Reactivity. *Inorg. Chem.* **2015,** *54* (12), 5879-5887.
159. Rohde, J. U.; Que, L., Jr., Axial coordination of carboxylate activates the non-heme FeIV=O unit. *Angew. Chem. Int. Ed.* **2005,** *44* (15), 2255-2258.
160. Singh, R.; Ganguly, G.; Malinkin, S. O.; Demeshko, S.; Meyer, F.; Nordlander, E.; Paine, T. K., A Mononuclear Nonheme Iron(IV)-Oxo Complex of a Substituted N4Py Ligand: Effect of Ligand Field on Oxygen Atom Transfer and C-H Bond Cleavage Reactivity. *Inorg. Chem.* **2019,** *58* (3), 1862-1876.
161. *APEX3, SAINT, SHELXTL, and SADABS* Bruker Analytical X-ray Systems: Madison, WI, USA, 2015.
162. Sheldrick, G., SHELXT - Integrated space-group and crystal-structure determination. *Acta Crystallogr.* **2015,** *71* (1), 3-8.
163. Sheldrick, G., Crystal structure refinement with SHELXL. *Acta Crystallogr.* **2015,** *71* (1), 3-8.
164. Hagen, K. S., Iron(II) Triflate Salts as Convenient Substitutes for Perchlorate Salts: Crystal Structures of $[Fe(H_2O)_6](CF_3SO_3)_2$ and $Fe(MeCN)_4(CF_3SO_3)_2$. *Inorg. Chem.* **2000,** *39*, 5867-5869.
165. *ASTM E1840-96, Standard Guide for Raman Shift Standards for Spectrometer Calibration*. ASTM International: West Conshohocken, PA, 2007.
166. George, G. N.; Pickering, I. J. *EXAFSPAK*, Stanford Synchrotron Radiation Laboratory, Stanford Linear Accelerator Center: Stanford, California, 2000.
167. Wojdyr, M., Fityk: a general-purpose peak fitting program. *J. Appl. Cryst.* **2010,** *43* (5-1), 1126-1128.